

Electrical transport and microwave study of a correlated two-dimensional electron system

Von der Fakultät Mathematik und Physik
der Universität Stuttgart zur Erlangung der Würde eines
Doktors der Naturwissenschaften (Dr. rer. nat.)
genehmigte Abhandlung

vorgelegt von
Daniela Țabrea
geboren in Suceava, Rumänien

Hauptberichter: Dr. habil. Jurgen H. Smet
Mitberichter: Prof. Dr. Sebastian Loth
Tag der mündlichen Prüfung: 22.06.2022

Max-Planck-Institut für Festkörperforschung
Stuttgart, 2022

Introduction and outline

Correlations in electron systems have long been an intriguing subject in condensed matter physics. Perhaps one of the most pervasive questions at the beginning of the last century was not how correlations impact observations, but why in some cases they appear to play little role. After all, early theories such as the Drude and the Sommerfeld models, successfully described key properties of charge carriers in metals while ignoring Coulomb interactions. This was despite the fact that in some materials such as sodium the average Coulomb energy exceeded the Fermi energy of the electron system. Significant progress in addressing this question was made by L. D. Landau in the 1950's through his Fermi liquid theory. The formalism assumes that low-energy single-particle excitations of an interacting fermion system can be obtained from corresponding excitations in the non-interacting case. This premise greatly simplified the daunting task of solving a many-body problem by reducing the effect of interactions to a set of Landau parameters which describe the behaviour of so-called quasiparticles - elementary excitations of a Fermi liquid. Within this framework quasiparticles can be treated as independent, albeit described by renormalized parameters with respect to the non-interacting counterparts. An in-depth account of the Fermi liquid theory can be found in the textbook by Pines and Nozières [1].

Landau's phenomenological theory was successful in explaining why electrons can often be approximated as free particles. Moreover it predicted how interactions may modify quantities such as specific heat, spin susceptibility, electron effective mass and g -factor provided the host material has a nearly spherical Fermi surface. It turns out, however, that the Fermi liquid approximation works well only when interactions are relatively weak. Transition metal oxides, for instance, host a series of perplexing states, among which high-temperature superconductivity, metal-to-insulator transitions, spin density waves and strange-metal states [2]. These systems have been broadly coined as strongly-correlated materials and understanding the complexity of their phase diagram still requires enormous theoretical effort.

Another instance of the breakdown of the Fermi liquid theory is the formation of an electron solid. As predicted by Wigner in 1934 [3], if interactions are sufficiently strong, electrons arrange in a crystalline structure to minimize Coulomb repulsion. In contrast to the electron liquid in which single particle excitations at the Fermi surface aid conductivity, the Wigner crystal would slide as a whole in the presence of an electric field. If a small amount of disorder is present, the electron solid is pinned at impurity sites, leading to an insulator-like behaviour. The effect of disorder on the electron solid phase is an interesting issue in itself. It is believed that while a weak disorder potential leads to a glassy phase in which charge order occurs over

a finite correlation length, strong fluctuating potentials due to material disorder results in single-particle localization with no correlated charge order.

A convenient way to gauge the strength of interaction in a many-body system is through the Wigner-Seitz parameter, r_s . While it is usually defined as the radius of a sphere which encompasses on average one electron, it can also be expressed as the ratio between the average Coulomb energy and the average kinetic energy. Counter-intuitively, r_s decreases with electron density, meaning that charge carriers interact more strongly when they are further apart. This is partly why electrons in most metals behave almost like free particles. One way to engineer a strongly-correlated system is by limiting the dimensionality. While nowadays two- and one-dimensional systems can be routinely obtained in both research laboratories and commercial setups, this achievement is due to decades-long experimental effort. Nonetheless, the result is rewarding. Intriguing individualistic *and* collective effects span the field of low-dimensional physics. Perhaps two of the best examples are the integer and the fractional quantum Hall effects (IQHE and FQHE, respectively). While the former can be explained within a single-particle picture, the latter requires the addition of correlations. Not only does the FQHE not abide by the Fermi liquid model, but it also goes beyond the realm of standard quantum statistics. A detailed description of both quantum Hall effects can be found in Ref. [4].

While the effects of correlations on charge carriers in two dimensions have been investigated for decades, the realization of high-quality strongly-interacting systems has been limited, until recently, only to a few materials. As we have seen, high quality is a key aspect because disorder can hinder the observation of exotic states such as the Wigner crystal. The electrons in Si-based metal-oxide-semiconductor field-effect transistors (MOSFET) interact strongly, but surface roughness create potential fluctuations which limit particle mobility. Reduced dimensionality does not promptly ensure strong correlations. For example, the highly mobile 2DES in GaAs/AlGaAs quantum wells spans relatively small values of the interaction parameter due to the small effective mass of electrons in this material. The 2D hole system (2DHS) in GaAs and the 2D electron system (2DES) in AlAs are examples where both aforementioned conditions are met and have indeed proven to be excellent platforms for the study of correlation-induced effects. The recent physics observed in twisted-bilayer graphene opens up a whole new realm of possibilities on the topic. Ever new opportunities are expected from other 2D materials which await to be studied.

The scope of this thesis is to identify and study the effects of correlations in another high-quality system in which large values of the interaction parameter can be easily achieved, namely the 2DES hosted by MgZnO/ZnO heterostructures. The thesis is organized in four chapters. In the first chapter we introduce basic physical concepts relevant to the work. The second chapter concerns the 2DES in a regime where it can be approximated with a Fermi liquid. Here we present both transport and microwave techniques for studying its properties. In the third chapter we investigate the system in the ultra-low density regime where a breakdown of the Fermi liquid model is expected. We explore the possibility of Wigner crystallization and a transition to a spin-ordered state. Finally, the fourth chapter presents a summary of the main findings as well as a few future directions of research.

Contents

1	Fundamentals	7
1.1	Transport properties in two dimensions	7
1.1.1	Electronic transport in the absence of a magnetic field	7
1.1.2	Classical magnetotransport	9
1.1.3	Quantum magnetotransport	10
1.2	Electron-electron interactions	16
1.2.1	The Fermi liquid formalism	18
1.2.2	Wigner crystals	21
1.3	Realization of a 2DES	22
1.3.1	Properties of the ZnO-based 2DES	25
1.4	Cyclotron resonance (CR) and magnetoplasmons (MPs)	28
1.5	Microwave-induced resistance oscillations (MIRO)	30
1.6	Electron spin resonance (ESR)	32
2	The two-dimensional electron liquid	35
2.1	Methods	35
2.2	Transport characterization	37
2.2.1	Carrier mobility	37
2.2.2	Magnetotransport and electron liquid parameters	37
2.3	Cyclotron resonance and magnetoplasmons	39
2.3.1	Detection scheme	40
2.3.2	Frequency dependence	42
2.3.3	Density dependence	45
2.4	Microwave-induced resistance oscillations	46
2.4.1	Detection	46
2.4.2	Determination of MIRO effective mass	47
2.4.3	Competition with CR	48

2.4.4	Power dependence of the microwave response	51
2.4.5	Discussion: effective mass	51
2.5	Electron spin resonance	53
2.5.1	Detection	54
2.5.2	ESR spectrum	55
2.5.3	Filling factor dependence	56
2.5.4	Temperature dependence	61
3	The 2DES in the ultra-low density regime	65
3.1	Methods	65
3.2	Transport characterization	69
3.2.1	Temperature dependent study	69
3.2.2	Electron pinning in an electric field	76
3.2.3	Magnetoresistance in a perpendicular magnetic field	82
3.2.4	Magnetoresistance in a parallel magnetic field	83
3.2.5	Temperature analysis of the resistance in a parallel B -field	89
3.2.6	Transition to a spin-ordered state	91
3.3	ESR in the dilute regime	94
4	Summary and outlook	99
	Zusammenfassung und Ausblick	103
	Bibliography	110

Chapter 1

Fundamentals

The two-dimensional electron system (2DES) hosted by MgZnO/ZnO heterostructures lies at the heart of this work. The methods of study are magnetotransport and microwave response. We therefore dedicate the first part of this chapter to introducing the basic properties of a 2DES in the presence of electric and/or magnetic fields. Following is an overview of the main models for describing the inter-particle interactions as well as the role of disorder. Further on we learn how such a system can be realized in practice, with special attention on the host material investigated in this thesis. Finally, we discuss the possible responses of the 2DES to microwave irradiation in the presence of a magnetic field.

1.1 Transport properties in two dimensions

1.1.1 Electronic transport in the absence of a magnetic field

The effect of an in-plane electric field \mathbf{E} on a 2DES can be understood in a quasi-classical approach based on the Drude model. Here we present a modified framework in which the following assumptions are made:

- charge carriers move independently from each other;
- electrons' interaction with their environment is described by the scattering time τ which is the average time between collisions with defects, impurities and phonons;
- the scattering rate does not depend on the particle velocity \mathbf{v} ;
- charge carriers move in straight lines between collisions;

Additionally, we consider that negatively charged particles move inside a ionic background potential of which the sole effect is to change the electronic mass from the free space value m_0 to the band value m . With these assumptions at hand we can write the equation of motion:

$$m \frac{d\mathbf{v}}{dt} = -m \frac{\mathbf{v}}{\tau} - e\mathbf{E}, \quad (1.1)$$

where e is the elementary charge. In steady state the velocity becomes constant $\mathbf{v} = \mathbf{v}_D$ and the solution to Eq. 1.1 is given by:

$$\mathbf{v}_D = -\frac{e\tau}{m}\mathbf{E} = -\mu\mathbf{E}. \quad (1.2)$$

Here the mobility μ is defined as the ratio between the electron drift velocity and the applied electric field and it is a measure of the response of an electron to an external \mathbf{E} -field. By substituting the drift velocity into the defining expression of the current density we obtain:

$$\mathbf{j} = -en\mathbf{v}_D = \frac{ne^2\tau}{m}\mathbf{E} = \sigma_0\mathbf{E} = \frac{1}{\rho_0}\mathbf{E}, \quad (1.3)$$

where σ_0 and ρ_0 are the conductivity and the resistivity, respectively, of the system in the absence of a magnetic field, and n is the electron density. The above equation allows us to deduce the scattering time and the mobility simply by measuring either σ_0 or ρ_0 . Since the conductivity depends on the charge carrier density, it is generally more convenient to use the mobility as a measure of system quality.

The mobility of an electron system is limited by deviations from a perfect crystal. Phonon, impurities, interface roughness, alloy randomness, intrinsic defects increase the probability of collision and thus limit τ . According to Matthiesen's rule, if different scattering mechanisms are independent, the total relaxation rate $1/\tau$ can be written as a sum:

$$\frac{1}{\tau} = \frac{1}{\tau_{\text{phonons}}} + \frac{1}{\tau_{\text{impurities}}} + \frac{1}{\tau_{\text{defects}}} + \dots \quad (1.4)$$

Phonon scattering is almost completely eliminated by decreasing the system temperature. As we will see further on, the other scattering mechanisms can be reduced by improved growth technologies and/or doping schemes. In some cases electron-electron scattering becomes important and has to be accounted for.

Not all scattering events contribute equally to the transport relaxation rate. Collisions which result in a large angle change θ of the electron momentum vector have a greater weight than small angle events. This can be quantified by the relationship [5]:

$$\frac{1}{\tau} = \int_0^\pi d\theta S(\theta)(1 - \cos\theta), \quad (1.5)$$

where $S(\theta)$ describes the scattering potential and it is a measure of the probability to be scattered at an angle θ . In contrast to τ , the quantum relaxation time τ_q is affected by all scattering events, regardless of the momentum direction change:

$$\frac{1}{\tau_q} = \int_0^\pi d\theta S(\theta). \quad (1.6)$$

This quantity reflects the lifetime of an electron in a certain state. Due to the higher probability of such events, generally $\tau > \tau_q$.

1.1.2 Classical magnetotransport

In the presence of both an electric and a magnetic field, the equation of motion 1.1 can be modified to include the Lorentz force, yielding:

$$m \frac{d\mathbf{v}}{dt} = -m \frac{\mathbf{v}}{\tau} - e(\mathbf{E} + \mathbf{v} \times \mathbf{B}). \quad (1.7)$$

Without loss of generality we can assume that the magnetic field is applied perpendicular to the 2DES i.e. along the z -axis, as shown in Fig. 1.1. In steady state ($d\mathbf{v}/dt = 0$), the electric field as a function of current density $\mathbf{j} = -ne\mathbf{v}_D$ is:

$$\begin{pmatrix} E_x \\ E_y \end{pmatrix} = \begin{pmatrix} \frac{m}{ne^2\tau} & \frac{B}{ne} \\ -\frac{B}{ne} & \frac{m}{ne^2\tau} \end{pmatrix} \begin{pmatrix} j_x \\ j_y \end{pmatrix} = \begin{pmatrix} \rho_{xx} & \rho_{xy} \\ \rho_{yx} & \rho_{yy} \end{pmatrix} \begin{pmatrix} j_x \\ j_y \end{pmatrix}. \quad (1.8)$$

The above result shows that the longitudinal resistivity (the resistivity along the current flow direction) is equal to the zero-field resistivity $\rho_{xx} = \rho_{yy} = \rho_0 = m/ne^2\tau$. From Eq. 1.3 we see that in the absence of a magnetic field the resistivity can be expressed as a diagonal matrix. This is no longer the case when $B \neq 0$: the magnetic field generates a current transverse to the external electric field. If, for example, the electric field is applied in the x -direction, the magnetic field will deflect the current in the y -direction. Under the steady state condition $j_y = 0$, charges accumulated at the sample edge create an electric field E_y that counteracts the Lorentz force:

$$E_y = -\frac{B}{ne} j_x. \quad (1.9)$$

The appearance of an electric field transversal to the applied one in the presence of a magnetic field is called the Hall effect.

A common setup for measuring the Hall effect is illustrated in Fig. 1.1. The magnetic field points along the z -axis. In panel (a) the current is applied between contacts 1 and 4, while the longitudinal voltage drop between 2 and 3 is recorded. Panel (b) shows an alternative configuration which facilitates measurement of the Hall voltage. Following Eq. 1.8, the Hall resistivity is simply given by:

$$\rho_{xy} = \frac{V_{xy}}{I_x} = \frac{V_{24}}{I_{13}} = \frac{B}{ne}. \quad (1.10)$$

Thus by knowing B , the Hall effect can be used to determine the charge carrier species and concentration of a sample.

Often it is difficult to perfectly align the probes such that there is no mixing between the transversal and the longitudinal components of the resistivity. Moreover, when point contacts are used, the current does not flow homogeneously across the sample. In this case the van der Pauw method can be employed to obtain the longitudinal resistivity [6]:

$$\rho_{xx} = \frac{\pi(V_{23}/I_{14} + V_{43}/I_{12})f}{2 \ln 2}. \quad (1.11)$$

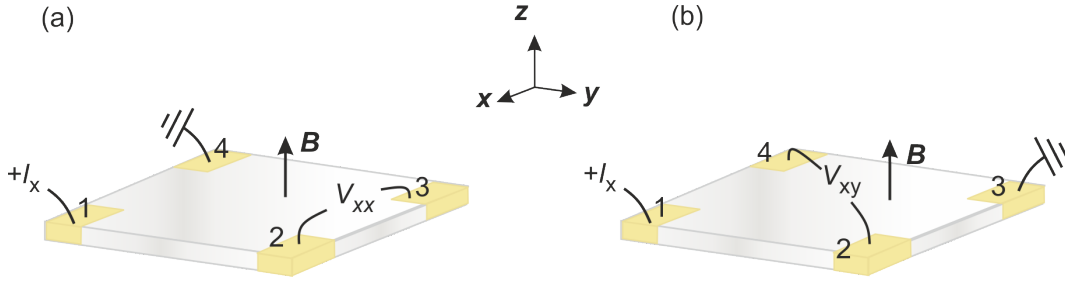


Figure 1.1: Schematic of a Hall measurement setup typical for transport experiments in this thesis. The magnetic field (black arrow) is pointing along z -axis. Measuring (a) V_{xx} and (b) V_{xy} allows the determination of longitudinal and transversal resistivity, respectively.

Here f is a factor which depends on the ratio between V_{23}/I_{14} and V_{43}/I_{12} and is equal to 1 for a square geometry. An accurate measurement of the transversal resistivity in the van der Pauw geometry can be obtained by measuring the Hall voltage both with and without magnetic field or for both B -field polarities:

$$\rho_{xy} = \frac{V_{13}(B) - V_{13}(0)}{I_{24}} = \frac{V_{13}(B) - V_{13}(-B)}{2 I_{24}}. \quad (1.12)$$

1.1.3 Quantum magnetotransport

Let us begin this section by posing the following question: what happens to the energy spectrum of an electron system if it is free to move in two dimensions but it is tightly confined in the third direction (e.g. along the z -axis)? To answer this, let us assume that the movement of the electrons of isotropic mass m and parabolic band structure is restricted in the z direction by infinite potential barriers separated by a distance L , i.e. $V(z) = \infty$ for $z < 0$ and $z > L_z$ but $V(z) = 0$ for $0 < z < L_z$. Because the particles are free to move in the xy -plane, the wave numbers k_x, k_y can take on any value and the corresponding kinetic energies are given by:

$$E_j = \frac{\hbar k_j^2}{2m}, \quad j = x, y. \quad (1.13)$$

The confinement along the z direction, however, leads to the quantization of k_z in integer units of π/L_z . Therefore the energy levels E_z are discrete and given by:

$$E_{zi} = \frac{\hbar^2 k_{zi}^2}{2m} = \frac{\hbar^2}{2m} \frac{i^2 \pi^2}{L_z^2}. \quad (1.14)$$

The ground state energy is no longer zero as in the unconfined case, but it is increased by the value:

$$\Delta E = \frac{\hbar^2}{2m} \frac{\pi^2}{L_z^2}. \quad (1.15)$$

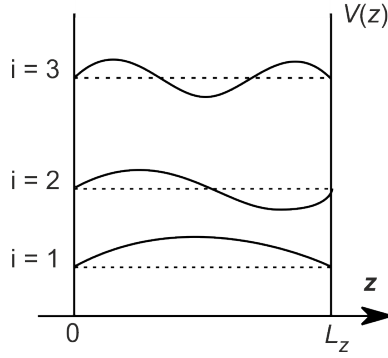


Figure 1.2: Schematic diagram of energy subbands (dashed lines) and wave function solutions (solid lines) in the z -direction for a 1D box with infinite barriers.

This energy offset is a consequence of the Heisenberg uncertainty principle: confinement within a distance L_z leads to an uncertainty of the order \hbar/L_z in k_z . The particle wavefunctions are described by standing waves, as illustrated in Fig. 1.2. One can see from Eq. 1.14 that the spacing between the energy bands increases as the confinement length decreases. If L_z is small enough, all electrons will occupy the lowest subband and their kinetic energy will depend only on the in-plane wavevectors k_x and k_y .

Real 2D electron systems have finite size with $L_x, L_y \gg L_z$, which leads to the allowed wavevectors $k_j = 2\pi l/L_j$, with $j = x, y$ and $l = 0, \pm 1, \pm 2, \dots$. Every state occupies an area in the (k_x, k_y) -space of $4\pi^2/(L_x L_y)$. Knowing that all the states of energy $E = \hbar^2 \vec{k}^2 / (2m)$ lie on a circle with radius k , one can write down the number of states of equal energy:

$$Z = \frac{\pi k^2}{4\pi^2/(L_x L_y)} g_s = \frac{L_x L_y}{4\pi} \frac{2mE}{\hbar^2} g_s n_v, \quad (1.16)$$

where $g_s = 2$ and n_v are the spin and valley degeneracies, respectively. The spin degeneracy is a consequence of the Pauli principle which allows two electrons of opposite spin $s = \pm 1/2$ to occupy the same state.

To obtain the density of states (DOS) per unit area around a certain energy, we divide the relation above to the total area $A = L_x L_y$ and take the derivative with respect to E :

$$D(E) = \frac{1}{A} \frac{dZ}{dE} = \frac{m n_v}{\pi \hbar^2}. \quad (1.17)$$

If the system only occupies the first subband, the DOS is constant for all energies for a material with parabolic dispersion. Therefore the electron density can be obtained by integrating the DOS over the occupied energy states:

$$n = \int_0^{E_F} D(E) dE = \frac{m n_v}{\pi \hbar^2} E_F. \quad (1.18)$$

Notice that we set the confinement energy ΔE to zero without the loss of generality.

In the presence of a magnetic field, the Hamiltonian of a spinless electron system

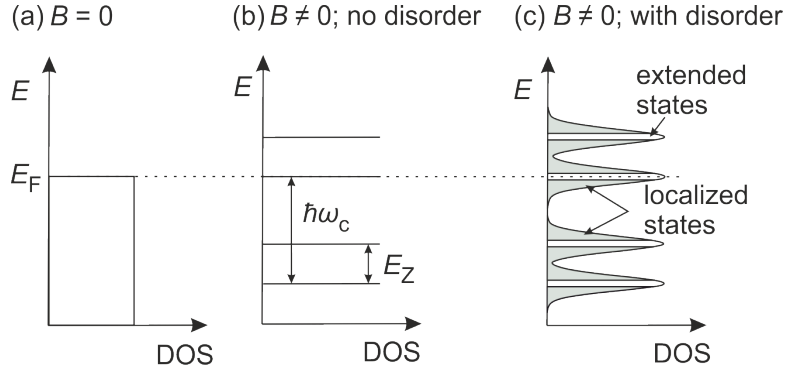


Figure 1.3: The energy spectrum of a 2DES: (a) at zero magnetic field; (b) in the absence of disorder at strong magnetic fields; (c) in a disordered sample at strong magnetic fields.

can be written as:

$$\mathbf{H} = \frac{1}{2m}(\mathbf{p} - e\mathbf{A})^2, \quad (1.19)$$

where \mathbf{p} is the electron momentum operator and \mathbf{A} is the vector potential associated with the magnetic field $\mathbf{B} = \nabla \times \mathbf{A}$. Here we take the magnetic field to be perpendicular to the 2DES plane $\mathbf{B} = B\mathbf{e}_z$ and we use the Landau gauge $\mathbf{A} = -B(y, 0, 0)$. Thus we can write the Schrödinger equation corresponding to the Hamiltonian \mathbf{H} :

$$\frac{1}{2m} \left(-i\hbar \frac{\partial}{\partial x} + eBy \right)^2 \psi - \frac{\hbar^2}{2m} \frac{\partial^2}{\partial y^2} \psi = E\psi. \quad (1.20)$$

Solving Eq. 1.20 one obtains the energy of the system:

$$E_N = \left(N + \frac{1}{2} \right) \hbar\omega_c, N = 0, 1, 2, \dots \quad (1.21)$$

where $\omega_c = eB/m$ is the cyclotron frequency and represents the rate at which the electrons perform cyclotron orbits. This result shows that charged particles occupy discrete energy levels indexed by $N = 0, 1, 2, \dots$ known as Landau levels (LL). The density of states is no longer a constant as found in Eq. 1.17, but a series of delta peaks as shown in Fig. 1.3(b). Due to their independence on momentum, Landau levels are highly degenerate, with the total number of states per level at a certain magnetic field given by:

$$\mathcal{N} = \frac{eBL_xL_y}{h} = \frac{A}{2\pi l_B^2}, \quad (1.22)$$

where $A = L_xL_y$ is the area of the sample and $l_B = \sqrt{\hbar/eB}$, a characteristic length scale in a magnetic field, is coined the magnetic length. The degeneracy can also be expressed in terms of the number of magnetic flux quanta $\Phi_0 = h/e$ that penetrate the sample: $\mathcal{N} = \Phi/\Phi_0$. If N_e is the total number of electrons in the system, we can define the filling factor as the number of occupied Landau levels:

$$\nu = \frac{N_e}{\mathcal{N}} = \frac{nh}{eB}. \quad (1.23)$$

The filling factor will be an integer number if the chemical potential lies at equal distance between two adjacent Landau levels. The inverse of the filling factor ν^{-1} represents the average number of flux quanta enclosed by each electron.

So far we have considered the electrons to be spinless. The interaction between spin-1/2 charge carriers and the applied magnetic field gives rise to an additional term in Eq. 1.21 associated with the Zeeman energy:

$$E_Z = g\mu_B B, \quad (1.24)$$

where g is the effective g -factor and $\mu_B = e\hbar/2m_0$ is the Bohr magneton. We have denoted the free electron mass as m_0 . A more detailed account of the Zeeman term is given in Section 1.6. The total energy can be written:

$$E_N = \left(N + \frac{1}{2}\right) \hbar\omega_c - sg\mu_B B, N = 0, 1, 2, \dots; s = \pm 1/2. \quad (1.25)$$

By convention we have chosen the spin up state ($s = 1/2$) to be lower in energy. Comparing the cyclotron energy $E_c = \hbar\omega_c$ with the Zeeman term $g\mu_B B$, one may find that they should be equal for an electron in vacuum. However, in real materials the effective electron mass and g -factor differ from the free electron values, such that frequently $\hbar\omega_c$ is larger than E_Z .

As seen in Fig. 1.3(b), in an ideal system a magnetic field splits the DOS in a sequence of infinitely narrow peaks. In a real 2DES disorder such as impurities, defects, interface roughness etc. are always present. This disorder potential leads to the broadening of the Landau levels. In the tails of the non-zero width peaks reside localized states. Electrons which occupy these states are trapped in either the hills or the valleys of the disorder potential. In contrast, electrons which occupy the states in the middle of a LL are delocalized (extended) and act as mobile carriers which can conduct current. The localized and extended states are shown schematically in Fig. 1.3(c).

The formation of a discrete energy levels in the presence of a magnetic field is at the basis of observing the integer quantum Hall effect (IQHE) in transport measurements. Typical IQHE traces for a GaAs-based two-dimensional system are shown in Fig. 1.4 [7]. A constant current is applied in the x -direction and the longitudinal R_{xx} and transversal R_{xy} resistance are measured against a varying magnetic field. At high fields ($B > 0.8$ T) wide plateaus start to appear in the Hall resistance, in contrast to the expected classical linear dependence. Moreover, the values at the plateaus are quantized as:

$$R_{xy} = \frac{h}{\nu e^2}, \nu = 1, 2, 3, \dots \quad (1.26)$$

Correspondingly the longitudinal resistance vanishes around integer values of the filling factor and exhibits high peaks otherwise. This behaviour can be intuitively understood by considering the DOS in Fig. 1.3(c). As explained above, if the chemical potential lies inside the mobility edge (where the extended states reside) electrons are free to move inside the sample, the longitudinal resistance is finite and the Hall resistance changes abruptly with B . Generally, the longitudinal resistance increases

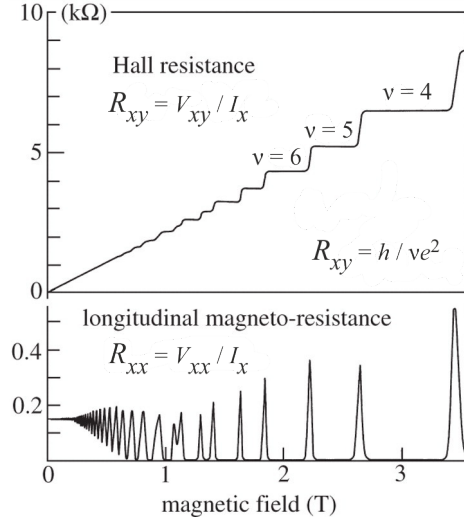


Figure 1.4: The integer quantum Hall effect in a GaAs-based 2DES. In a quantum Hall state, the transversal resistance takes on integer values of $h/(\nu e^2)$, while the longitudinal resistance vanishes. From Ref. [7].

with DOS, which explains the increasing peak amplitude observed in R_{xx} . If, however, the Fermi energy enters the region of localized states, electrons are trapped in the disorder potential, which leads to a vanishing longitudinal conductivity. If $\hat{\sigma}$ is the conductivity tensor, inverting it we obtain:

$$\hat{\rho} = \frac{1}{\sigma_{xx}^2 + \sigma_{xy}^2} \begin{pmatrix} \sigma_{xx} & -\sigma_{xy} \\ \sigma_{xy} & \sigma_{xx} \end{pmatrix}. \quad (1.27)$$

Thus if the conductivity is zero, the resistivity will be zero as well: $\rho_{xx} = \sigma_{xx}/(\sigma_{xx}^2 + \sigma_{xy}^2) = 0$.

To understand the quantization of the Hall resistance it is useful to include into the discussion the sample edges. In the absence of a magnetic field, the bulk value of the charge density n decreases smoothly to zero towards the edge of a 2DES. In this regime the DOS is constant. If a perpendicular field is applied, the DOS splits into discrete levels which bend stepwise upwards in the depletion zone. Stripes with varying and constant charge density form. The regions where the electron density varies are called compressible stripes. Here the Fermi level lies inside a Landau level and electrons can therefore screen electrostatic potential variations. In contrast, inside the regions with constant electron density the Fermi level lies between Landau levels which bend upwards. Due to the lack of free states at the chemical potential, electrons cannot rearrange to screen an electric field. These regions are called incompressible.

The bending of the Landau levels in the incompressible stripes means that there is an electric field E_y in the y -direction which translates into a drift current in the x -direction. All the Landau levels which in the bulk of the sample are occupied

contribute to the total current density in the x -direction which can be written:

$$j_x = \nu \frac{e^2}{h} E_y. \quad (1.28)$$

A diagram of the sample edge is shown in Fig. 1.5. The black arrows show the direction of dissipationless current flowing in the incompressible stripes (unshaded areas).

Note however that in the absence of a Hall voltage the current flowing on one side of the sample is cancelled by the current flowing on the opposite side, resulting in a zero net current. A Hall voltage V_{xy} increases the current on one edge with respect to the other, which leads to the net result over the whole width of the sample:

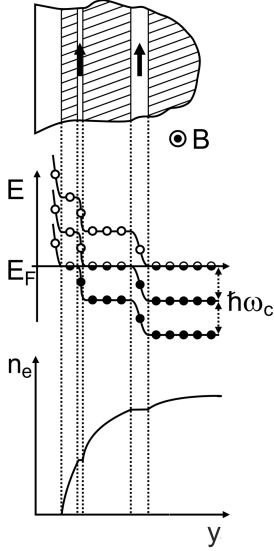
$$I_x = \nu \frac{e^2}{h} V_{xy}. \quad (1.29)$$

This current flows dissipationless in the incompressible stripes when the system is in a quantum Hall state and gives rise to a quantized Hall resistance:

$$R_{xy} = \frac{h}{\nu e^2}. \quad (1.30)$$

This simplified explanation of the IQHE only skims the surface of decades-long studies of this effect. A detailed description is beyond the scope of this thesis and we therefore direct the reader to a list of publications [4, 7, 8, 9, 10, 11, 12].

Figure 1.5: Compressible and incompressible stripes in the quantum Hall regime. See text for explanation. Modified from Ref. [8].



At moderate magnetic field, where the QHE is not fully developed ($B < 0.6$ T in Fig. 1.4) oscillations periodic in $1/B$ occur in the longitudinal resistivity due the oscillatory DOS. They are called Shubnikov-de Haas oscillations (SdHO) and can be described by the following relation:

$$\frac{\rho_{xx}(B) - \rho_0}{\rho_0} = 2 \cos \left[2\pi \left(\frac{E_F}{\hbar\omega_c} - \frac{1}{2} \right) \right] \cos \left(2\pi \frac{g\mu_B B}{2\hbar\omega_c} \right) \exp \left(-\frac{\pi m}{\tau_q e B} \right) \frac{X}{\sinh X}, \quad (1.31)$$

where

$$X = \frac{2\pi^2 k_B T}{\hbar\omega_c}. \quad (1.32)$$

The first cosine expresses the $1/B$ oscillatory behaviour, while the second cosine accounts for the spin degeneracy splitting. If the Zeeman energy is much lower than the cyclotron energy, this term can be dropped. The exponential term describes the envelope of the oscillations, the amplitude of which increases with field. It compares $\hbar\omega_c$ with the broadening of the Landau levels Γ . This term allows the extraction of the quantum scattering time by virtue of the relation $\Gamma = \hbar/(2\tau_q)$. The last term

takes into account the effect of finite temperature on the Fermi distribution. Since the dampening is described by the ratio between $k_B T$ and the cyclotron energy, the effective mass m can be estimated by temperature dependent measurements.

At low temperatures the Shubnikov-de Hass oscillations and the quantum Hall effect appear in all the samples studied in this thesis and are used to determine the electron density as well as to estimate the system quality. By assuming that the SdHO become apparent when the cyclotron energy is of the order of the LL width ($\Gamma \approx \hbar\omega_c$), one can use the corresponding value of the magnetic field to calculate the quantum lifetime:

$$\tau_q = \frac{1}{2\omega_c}. \quad (1.33)$$

1.2 Electron-electron interactions

So far we have neglected electron-electron interactions in our calculations of electron transport. However phenomena such as the fractional quantum Hall effect, electron crystallization and hydrodynamic effects could not be accounted for in a free-electron approach. In this section we will briefly introduce a formalism which sheds some light on the possible ground states of an interacting electron system. The corresponding Hamiltonian is given by:

$$\mathbf{H} = \sum_i \frac{\mathbf{p}_i^2}{2m} + \frac{1}{2} \sum_{i \neq j} \frac{e^2}{4\pi\epsilon |\mathbf{r}_i - \mathbf{r}_j|}, \quad (1.34)$$

where ϵ is the dielectric constant of the hosting material. The first term represents the kinetic energy, while the second is the Coulomb energy. If n is the electron density, then the average distance between two electrons can be expressed as:

$$\langle r \rangle = \frac{1}{\sqrt{\pi n}}. \quad (1.35)$$

The Coulomb term becomes:

$$E_C = \frac{e^2}{4\pi\epsilon \langle r \rangle} = \frac{e^2}{4\pi\epsilon} \sqrt{\pi n}. \quad (1.36)$$

If the temperature of the system is much lower than the Fermi energy, then the system is said to be degenerate and the average energy per particle can be approximated as:

$$E_F = \frac{\pi \hbar^2}{n_v m} n, \quad (1.37)$$

where n_v is the number of occupied valleys. A convenient way to estimate the strength of interaction is through the Wigner-Seitz (WS) radius r_s , which can be written as the ratio between the Coulomb and the kinetic terms:

$$r_s = \frac{E_C}{E_F} = \frac{n_v e^2 m}{4\pi\epsilon \hbar^2 \sqrt{\pi n}}. \quad (1.38)$$

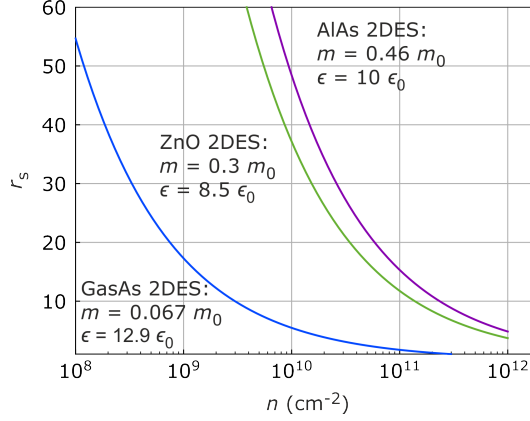


Figure 1.6: Density dependence of the interaction parameter for three different 2DESs, as indicated.

Assuming $n_v = 1$ and using the definition of the Bohr radius,

$$a_B = \frac{4\pi\epsilon\hbar^2}{e^2m_0}, \quad (1.39)$$

the interaction parameter can be expressed as the average inter-particle distance in units of the effective Bohr radius: $r_s = \langle r \rangle / (4\pi\epsilon\hbar^2/e^2m)$. As seen in Eq. 1.38, r_s is proportional to the effective mass m and inversely proportional to the dielectric constant ϵ . This leads to the interaction strength being host material dependent, as exemplified in Fig. 1.6.

Contrary to intuition, interactions are stronger when electrons are further apart from each other. In the limit of high charge carrier density where r_s is small, the correlations are weak and the system behaves like a non-interacting Fermi gas. The electron-electron interactions are gradually “switched on” as n decreases and the Coulomb energy becomes dominant, leading to the so-called Fermi liquid phase. In the very dilute regime, $r_s \geq 35$, it is predicted that the ground state of the system is a Wigner solid - an electron crystal formed due to strong Coulomb repulsion [3, 13].

A comprehensive diagram of the different phases of an interacting electron system is both a great challenge and an interesting problem in condensed matter physics. While the Fermi liquid is fairly well justified in practice [14, 15, 16, 17, 18], the observation of Wigner crystals has proven more challenging [19, 20, 21]. This is in part due to ubiquitous disorder in such systems which leads to electron localization before the solid phase sets in [22]. Theory suggests that there cannot be a direct first order transition between a Fermi liquid and a Wigner crystal, but rather a continuous transition through liquid crystalline phases [23]. It is also widely believed that the system may undergo other symmetry transformations at intermediate values of the interaction parameter, such as a transition to spin-ordered states [24, 25, 26].

In this thesis we employ transport and microwave resonance measurements to study the evolution of the ZnO-based 2DES through different phases as the charge carrier density is varied. The large electron band mass and relatively low dielectric constant of ZnO give access to the large r_s regime where the inter-particle interactions dominate over the kinetic energy.

1.2.1 The Fermi liquid formalism

Fermi liquid theory was developed by L. D. Landau (1954) to describe the behaviour of liquid ^3He at low temperatures. Later on his formalism was adapted for conduction electrons in metals. The theory relies on the observation that even in strongly interacting systems where $r_s \gg 1$ particles seem to behave independently. In this regime, a perturbative approach (where one considers the Coulomb energy a small perturbation) would clearly not work as the interaction term greatly exceeds the kinetic energy. Landau constructed his formalism around the assumption that the excited states close to the Fermi surface of the interacting system can be obtained from the excited states of the free system by slowly turning on the interactions. This adiabatic switching on ensures a one-to-one correspondence between the states of the Fermi gas and those of the Fermi liquid. The main success of this phenomenological theory is that it correctly identifies how various parameters are renormalized by interactions and how some of these observables are related to each other.

In this section we will briefly introduce key notions of the Fermi liquid theory by closely following calculations in chapter 8 of Ref. [27]. A more complete study can be found in Ref. [1]. Let us denote by $\{\mathcal{N}_{\vec{k}\sigma}\}$ the set of occupation numbers of non-interacting single-particle states. Thus a state of momentum \vec{k} and spin σ has the probability $\mathcal{N}_{\vec{k}\sigma}$ to be occupied and $1 - \mathcal{N}_{\vec{k}\sigma}$ to be empty. In the ground state at $T = 0$, $\mathcal{N}_{\vec{k}\sigma}^{(0)} = \Theta(k_F - k)$, where $\Theta(x)$ is the Heaviside step function. Landau's first assumption is that the same set of occupation numbers can be used to describe the Fermi liquid: an excited state with $k > k_F$ of the free system evolves into an excited state with equal momentum of the interacting system. This approximation holds for low-lying excitations due to the Pauli exclusion principle: an excited electron with $k = k_F + \delta k$ can only scatter into states lying in a narrow shell of width δk around the Fermi surface - all the other states allowed by momentum and energy conservation are already occupied; since the scattering time decreases with the number of available states, a change in the occupation numbers occurs very slowly. One should note however that $\{\mathcal{N}_{\vec{k}\sigma}\}$ are not the true occupation numbers of the Fermi liquid excited states, but can be regarded as such over time intervals shorter than the average scattering time. The states associated with these occupation numbers describe the spectrum of electrons dressed by interactions. They are coined quasi-particle states.

Restricting the discussion to low-lying excitations is reasonable in practice as well. Transport measurements at low temperatures rely on scattering of electrons into states close to the Fermi surface. Let us define the deviation in occupation from the ground state value as $\delta\mathcal{N}_{\vec{k}\sigma} = \mathcal{N}_{\vec{k}\sigma} - \mathcal{N}_{\vec{k}\sigma}^{(0)}$. For a free electron gas we can expand the energy to first order in $\delta\mathcal{N}_{\vec{k}\sigma}$:

$$E = E_0 + \sum_{\vec{k}\sigma} \frac{\hbar^2 k^2}{2m} \delta\mathcal{N}_{\vec{k}\sigma}, \quad (1.40)$$

where E_0 is the ground state energy. In the Fermi liquid case, since quasiparticles are allowed to interact with one another, an expansion to second order is necessary:

$$E[\{\mathcal{N}_{\vec{k}\sigma}\}] = E_0 + \sum_{\vec{k}\sigma} \varepsilon_{\vec{k}\sigma} \delta\mathcal{N}_{\vec{k}\sigma} + \frac{1}{2} \sum_{\vec{k}\sigma, \vec{k}'\sigma'} f_{\vec{k}\sigma, \vec{k}'\sigma'} \delta\mathcal{N}_{\vec{k}\sigma} \delta\mathcal{N}_{\vec{k}'\sigma'}. \quad (1.41)$$

Here $\varepsilon_{\vec{k}\sigma}$ denotes single quasiparticle energies and $f_{\vec{k}\sigma,\vec{k}'\sigma'}$ is the Landau interaction function. The Fermi velocity of the quasiparticles can be written as:

$$v_{\text{F}}^* = \frac{1}{\hbar} \left| \frac{\partial \varepsilon_{\vec{k}\sigma}}{\partial \vec{k}} \right|_{k=k_{\text{F}}}, \quad (1.42)$$

which in turn allows the definition of the quasiparticle effective mass:

$$m^* = \frac{\hbar k_{\text{F}}}{v_{\text{F}}^*}. \quad (1.43)$$

The band effective mass differs from the quasi-electron effective mass. The former is determined by the curvature of the conduction band bottom, while the latter depends on the interaction-induced renormalization of the Fermi velocity.

The Landau interaction function $f_{\vec{k}\sigma,\vec{k}'\sigma'}$ in Eq. 1.41 describes the scattering of two electrons with momenta \vec{k} and \vec{k}' and spins σ and σ' . Since our system is isotropic in momentum and we focus only on quasiparticles close to the Fermi surface, f depends only on the angle between \vec{k} and \vec{k}' . Thus we can write $f_{\vec{k}\sigma,\vec{k}'\sigma'} \approx f_{\sigma,\sigma'}(\hat{k} \cdot \hat{k}')$. In the absence of an external field, the system is invariant under time-reversal and reflection, implying that f depends only on the relative orientation of the spin which can be either $\uparrow\uparrow$ or $\downarrow\uparrow$. The interaction function can then be separated into spin symmetric and spin antisymmetric components:

$$f^{\text{s}}(\hat{k} \cdot \hat{k}') = \frac{1}{2} [f_{\uparrow\uparrow}(\hat{k} \cdot \hat{k}') + f_{\downarrow\downarrow}(\hat{k} \cdot \hat{k}')] \quad (1.44)$$

$$f^{\text{a}}(\hat{k} \cdot \hat{k}') = \frac{1}{2} [f_{\uparrow\downarrow}(\hat{k} \cdot \hat{k}') - f_{\downarrow\uparrow}(\hat{k} \cdot \hat{k}')]. \quad (1.45)$$

Writing down the corresponding Fourier expansion:

$$f^{\text{s,a}}(\hat{k} \cdot \hat{k}') = \sum_{l=0}^{\infty} f_l^{\text{s,a}} \cos(l\theta), \quad \text{where } \theta = \hat{k} \cdot \hat{k}', \quad (1.46)$$

we can define the dimensionless Landau parameters:

$$F_l^{\text{s,a}} = A D^*(E_{\text{F}}) f_l^{\text{s,a}}. \quad (1.47)$$

In the equation above A denotes the area of the system and the density of states at the Fermi level $D(E_{\text{F}})$ is given by Eq. 1.17. The mass entering $D^*(E_{\text{F}})$ is in this case the renormalized quasiparticle mass. It can be shown [27] that m^* and the interaction function f are connected through the Landau parameter F_1^{s} by:

$$\frac{m^*}{m} = 1 + \frac{1}{2} F_1^{\text{s}}, \quad (1.48)$$

where m is the electron mass of the non-interacting system. The simplicity of this equation reflects the power of Landau's theory. Despite complex many-body interactions, one of the key quantities describing the Fermi liquid system can be reduced to a single parameter equation. In practice, calculating the set $F_l^{\text{s,a}}$ typically

requires appropriate choice of trial functions and a reduced system size (a few tens of electrons).

In the presence of a magnetic field, the isolated quasiparticle energy becomes:

$$\varepsilon_{\vec{k}\sigma}(B) = \varepsilon_{\vec{k}\sigma} + \frac{1}{2}g\mu_B B\sigma. \quad (1.49)$$

As a result electrons with spin up will lower in energy by an amount $\delta\varepsilon_{\vec{k}\uparrow}$, while electrons of opposite spin will gain an equal amount in energy. Associated with this shift in energy is a change of $\delta k_{F\uparrow} = -\delta k_{F\downarrow}$ in the Fermi momentum. The net magnetization per unit area can therefore be written:

$$M = -\frac{1}{2}g\mu_B(\delta n_{\uparrow} - \delta n_{\downarrow}) = \frac{1}{2}g\mu_B D^*(E_F)\delta k_{F\downarrow}. \quad (1.50)$$

It can be shown that at equilibrium the change in momentum expressed in terms of the Fermi parameters is given by:

$$\delta k_{F\downarrow} = \frac{g\mu_B B}{2\hbar v_F^*} \frac{1}{1 + F_0^a}. \quad (1.51)$$

Substituting this into Eq. 1.50 and using the definition of susceptibility $M = \chi B$, we find:

$$\chi^* = \left(\frac{g\mu_B}{2}\right)^2 \frac{D^*(E_F)}{1 + F_0^a}. \quad (1.52)$$

We identify $\chi = (g\mu_B)^2 D(E_F)/4$ as the Pauli (non-interacting gas) susceptibility. Thus Eq. 1.52 becomes:

$$\frac{\chi^*}{\chi} = \frac{m^*}{m} \frac{1}{1 + F_0^a}. \quad (1.53)$$

In a similar vein, one can find the expression for the renormalized g -factor:

$$\frac{g^*}{g} = \frac{1}{1 + F_0^a}. \quad (1.54)$$

Combining Eqs.1.53 and 1.54 we have:

$$\frac{\chi^*}{\chi} = \frac{m^* g^*}{m g}. \quad (1.55)$$

These results highlight the effect of interactions on measurable quantities. A Fermi liquid retains the general behaviour of free particles: it has a well-defined Fermi surface and the transport properties found in the previous section still hold. Parameters describing the quasiparticle system are, however, renormalized by interactions. There are numerous studies dedicated to calculating the many-body effective mass, g -factor and spin susceptibility of 2DESs and to corroborating these results with experimental findings. Most transport measurements agree on the enhancement and apparent divergence of spin susceptibility in the limit of large r_s . A diverging χ as the carrier density is reduced may indicate that the system approaches a phase transition. A Stoner instability leading to a fully spin polarized state is supported both by theory and experiment [24, 26]. Another possible candidate is the Wigner

crystal, which will be discussed in the following subsection.

1.2.2 Wigner crystals

At sufficiently low carrier densities, the Coulomb energy is much larger than the kinetic energy of the system. Wigner [3] was the first to suggest that in this limit the kinetic energy can be neglected and electrons arrange in a crystalline lattice due to the Coulomb repulsion.

The static ground state energy of the two-dimensional Wigner crystal was calculated by Bonsall and Maradudin [28] by considering a system with constant electron density embedded in a uniform positive charge background. The total energy is then obtained by adding up the electrostatic interaction energy between a given electron with all the other electrons in the crystal and with the neutralizing positive background of density ρ_+ :

$$E_1 = E_1^{(e)} + E_1^{(b)} = \frac{e^2}{4\pi\epsilon} \lim_{\vec{x} \rightarrow 0} \left(\sum_l \frac{1}{|\vec{x} - \vec{x}(l_1, l_2)|} - \frac{1}{|\vec{x}|} \right) - \frac{e\rho_+}{4\pi\epsilon} \int_A \int_A \frac{d^2x}{|\vec{x}|}. \quad (1.56)$$

In the equation above the integral is carried out over the area of the crystal. The position of the lattice points in real space is expressed with the help of the primitive lattice vectors \vec{a}_1 and \vec{a}_2 :

$$\vec{x} = l_1 \vec{a}_1 + l_2 \vec{a}_2, \quad (1.57)$$

where l_1 and l_2 are integer numbers. The energy per particle can be written in terms of the Misra functions $\phi_n(z)$ (see tabulated values in Ref. [29]):

$$E_1 = -\frac{2e^2\sqrt{n}}{4\pi\epsilon} \left[2 - \sum_{l_1, l_2 \neq 0} \phi_{-1/2} \left(\frac{\pi}{a_c} x^2(l_1, l_2) \right) \right], \quad (1.58)$$

with a_c the area of the unit cell. Bonsall and Maradudin have evaluated this expression for five different Bravais Wigner lattices, out of which the hexagonal lattice yielded the lowest ground state energy:

$$E_1^{\text{hex}} = -\frac{3.921034}{2} \frac{e^2\sqrt{n}}{4\pi\epsilon} \text{ (J)} = -\frac{2.2122}{r_s} \text{ (Ry)}, \quad (1.59)$$

where the Rydberg unit Ry is defined as:

$$\text{Ry} = \frac{m^* e^4}{2\hbar^2 (4\pi\epsilon)^2}. \quad (1.60)$$

This result takes into account only the classical static energy of the Wigner crystal. The leading quantum mechanical corrections are due to the zero point motion of the electrons localized at the lattice points. Tannatar and Cheperley [13] have performed Quantum Monto Carlo calculations to estimate the total Wigner crystal energy:

$$E_{\text{WC}} = -\frac{2.2122}{r_s} + \frac{1.628}{r_s^{3/2}} + \frac{0.0508}{r_s^2} \text{ (Ry)}, \quad (1.61)$$

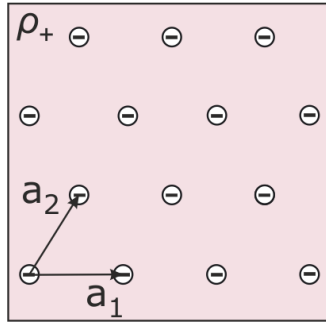


Figure 1.7: Schematic of a two-dimensional Wigner crystal embedded in a positive background of homogeneous density ρ_+ .

where the second and the third terms are due the zero-point energy and anharmonic contributions, respectively.

With the ground state energy of the unpolarized Wigner crystal at hand one might pose the following question: what is the value of r_s at which a Fermi liquid crystallizes? To determine the phase diagram of a strongly-interacting system the energy of the Wigner crystal should be compared with the energy of other possible states, which includes paramagnetic Fermi liquid, partially- and fully-polarized Fermi liquid, antiferromagnetic Wigner crystal. The symmetry of these phases has to be assumed a priori, which means that the true ground state might have been completely disregarded. Despite decades of efforts in Quantum Monte Carlo calculations [13, 24, 25, 30] as well as electrical [19, 20, 26, 31, 32, 33] and optical measurements [21, 34, 35, 36, 37], there is no consensus on a complete phase diagram. However both theoretical and experimental studies point to a Wigner crystallization when $r_s \approx 30 - 40$.

So far observations of Wigner crystals primarily relied on temperature dependent conductivity measurements of high-mobility systems [19, 20, 26]. These studies often include sub-linear $I - V$ curves, which have been attributed to the interaction-mediated pinning of the charge carriers. Recently strong experimental evidence has also been reported in transition-metal dichalcogenide (TMD) structures [21, 36]. Here modifications in the exciton band structure pinpoint a transition to a charge ordered state. Perhaps the most convincing evidence for this fragile state is the real-space imaging of the electronic lattice reported in WSe_2/WS_2 heterostructures [38]. These advances have reignited interest in the topic and encourage further investigations on the ground state of the interacting 2D many-body system.

1.3 Realization of a 2DES

Improvements in the semiconductor technology has paved the way towards routinely manufacturing high-quality heterostructures. The invention and development of ultra-high vacuum molecular-beam epitaxy in the 1960s and 1970s is perhaps one of the most important steps in the fabrication of state-of-the-art devices. In combination with improved lithographic and etching methods, these devices can be scaled down to the nanoscale.

Among the applications of semiconductor structures growth is the confinement

of charge carriers in two dimensions. In Fig. 1.8(a-c) three representative examples are shown. The first panel illustrates a schematic of a silicon metal-oxide-semiconductor field-effect transistor (Si MOSFET) and the corresponding energy band diagram. To achieve potential equilibrium, electron transfer from the metallic gate to the p -doped Si occurs. Due to the formation of an electric field across the junction, the energy bands bend such that close to the oxide-semiconductor interface the conduction band in Si is lowered. By adjusting the gate voltage, the electron concentration in the accumulation layer (also commonly known as an inversion layer) can be tuned [39]. The device can be modified to host a two-dimensional hole system by using an n -type Si transistor body instead.

The Si MOSFET has a special place in the semiconductor device evolution not only because of its high-performance and large-scale integration capability, but also because it was the first device that allowed the observation of new physical phenomena. Among them one can name the Integer Quantum Hall effect (IQHE) [9] and the metal-insulator transition (MIT) [40]. It is also argued that strong evidence for a Wigner crystal formation was first reported in a Si MOSFET [41]. The observation of the latter two is facilitated by inter-particle correlations, owing to the relatively large effective mass $m = 0.19m_0$ [42], a dielectric constant of $\epsilon = 7.8\epsilon_0$ and the existence of two almost degenerate valleys ($n_v = 2$). Using Eq. 1.38, these parameters lead to typical interaction parameter values of $r_s \sim 10 - 40$.

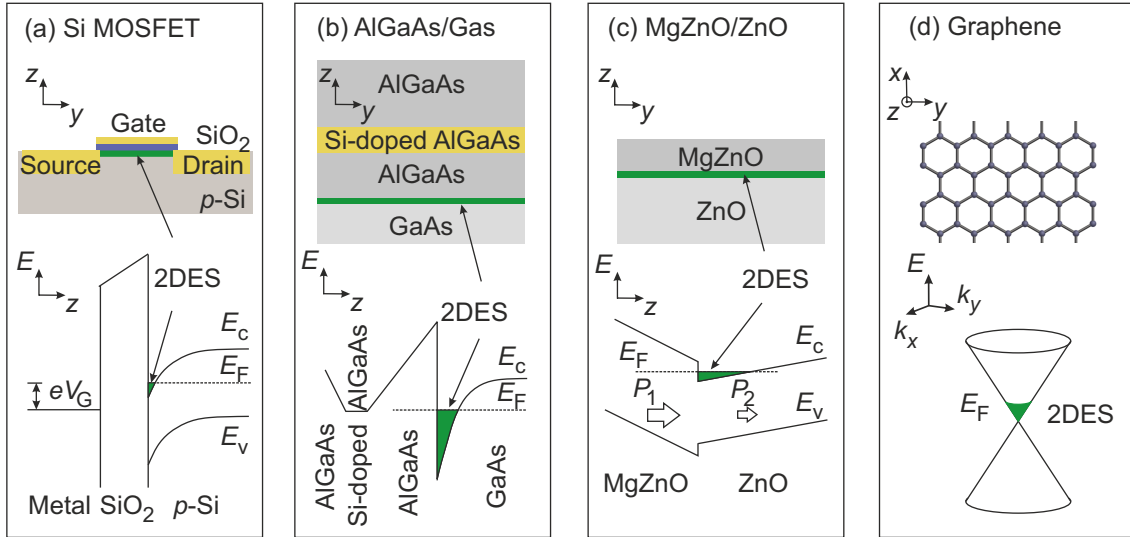


Figure 1.8: Schematic diagrams of four representative 2D systems and their corresponding energy band structure. (a) Si MOSFET; (b) Modulation-doped AlGaAs/GaAs heterostructure; (c) MgZnO/ZnO heterostructure (d) Monolayer graphene.

Since the invention of the transistor there has been a big incentive for the production of high-mobility devices due to potential end-use technologies. This is in part due to the close relation between mobility and transistor switching frequency. In Si MOSFETs mobility is limited by charged states in the oxide layer as well as roughness at the SiO₂/Si interface. To this day the highest value reported is $\mu = 3 \times 10^4 \text{ cm}^2 \text{ V}^{-1} \text{ s}^{-1}$ [22]. A big leap forward was made when the doping layer was separated from the heterojunction where the 2DES is formed. Such an

example is shown for an AlGaAs/GaAs heterostructure in Fig. 1.8(b). In this case, the mismatch between the band gap of AlGaAs and GaAs ensures the creation of a quantum well. At low temperature, the bulk of the sample becomes insulating and charge is transferred from the doping layer to the quantum well until equilibrium is reached. Further improvement was achieved by designing a short period superlattice of doped GaAs layers separated by AlAs layers by means of which the effect of charged donors is reduced. State-of-the-art GaAs-based 2DESs present mobilities of $44 \times 10^6 \text{ cm}^2 \text{ V}^{-1} \text{ s}^{-1}$.

The high-quality of GaAs-samples made possible the discovery of fragile fractional quantum Hall states [43, 44, 45]. In comparison to the 2DES in Si MOSFETs, electron-electron interactions in a AlGaAs/GaAs heterostructure are almost an order of magnitude weaker for the same charge carrier density. In other words, values of n two orders of magnitude lower have to be used to achieve the same r_s range as in Si. Larger interaction parameters are achieved in p -GaAs quantum wells due to the larger effective mass of holes.

A whole class of materials have been used to create heterostructures with various properties, as listed in Table 1.1. Special attention has been given to AlAs and SiGe/Si/SiGe QWs due to their valley degree of freedom and anisotropic mass as well as the large spin-orbit coupling (SOC) in AlAs which add further twists in interaction-mediated effects [26, 46, 47, 48].

Table 1.1: Comparison between parameters determining the cyclotron, Coulomb and Zeeman energy scales for various 2D system.

Material	Charge species	Peak mobility ($\text{cm}^2 \text{ V}^{-1} \text{ s}^{-1}$)	Effective mass (m_0)	Dielectric cst. (ϵ_0)	g -factor	Valleys
Si MOSFET	e	3×10^4 [22]	0.19 [42]	7.8	2 [49]	2
SiGe/Si	e	2.4×10^6 [50]	\sim	\sim	\sim	\sim
AlGaAs/GaAs	e	44×10^6 [51]	0.067 [52]	12.9	-0.44 [53]	1
	h	2×10^6 [54]	$m_l = 0.38$ $m_h = 0.6$ [55]	\sim	1	\sim
AlAs	e	2.4×10^6 [56]	$m_l = 1.1$ $m_t = 0.2$ [57]	10	2 [57]	2
AlGaN/GaN	e	6×10^4 [58]	0.22 [59]	8.9	1.95 [60]	1
MgZnO/ZnO	e	1.3×10^6 [61]	0.3 [62]	8.3	1.95 [63]	1

¹The g -factor in GaAs-based 2DHS is highly anisotropic and depends strongly on QW width.

In Fig. 1.8(c) we present a third design hosting a ZnO-based 2DES. One may immediately notice the simplicity of the heterostructure which requires the epitaxial growth of only two layers, namely pure ZnO and Mg-alloyed ZnO. A finite spontaneous polarisation is present in both layers. Due to a difference in the polarisation magnitudes charge carriers from ionized impurities in the substrate will accumulate at the interface. Since a higher concentration of Mg in the cap layer leads to a larger polarization mismatch, the electron density can be controlled by adjusting the alloy content. A more detailed description is given in the following subsection. Another example of polarisation-induced 2DES is the AlGa_N/Ga_N heterostructure [68].

Last but not least, Fig. 1.8(d) illustrates the lattice structure and the band structure of graphene - a single layer of carbon atoms arranged in a hexagonal pattern. We direct the reader towards review papers for more details on graphene's electronic properties, current challenges and possible applications [69, 70]. Since the first exfoliated graphene sample was reported [71] the interest in atomically-thin systems has boomed. Making use of the weak inter-layer van der Waals bond, a few dozens of 2D materials have been successfully isolated to this day. However, hundreds of new compounds await to be studied [72]. Due to their reduced size, relatively high mobility at room temperature as well as low cost of production, 2D materials have potential applications in electronics.

1.3.1 Properties of the ZnO-based 2DES

The material hosting the 2DES studied in this thesis is ZnO and its alloy, Mg_xZn_{1-x}O. Crystallized in hexagonal wurtzite, the lattice constants are $a = 3.25 \text{ \AA}$ and $c = 5.2 \text{ \AA}$. In this structure each Zn atom is surrounded by four oxygen atoms positioned at the corners of a tetrahedron (see Fig. 1.9). The Zn s electrons hybridise with the O p electrons to form sp^3 covalent bonds. Due to the strong electronegativity of the oxygen, the bond has substantial ionic character which leads to a certain degree of polarity in the [0001] crystal direction. This explains why the c/a ratio of 1.6 in ZnO deviates from the ideal wurtzite structure where $c/a = 1.633$. At room temperature, ZnO has a wide direct band gap of $E_g = 3.37 \text{ eV}$ and an exciton binding energy of $E_x = 60 \text{ mV}$. By using Mg as an alloy, E_g can be increased up to 3.99 eV for $x = 0.35$, which renders ZnO attractive for optoelectronic devices [74, 75]. A further increase in alloy content leads to dramatic structural changes, as MgO preferably crystallizes in a rock-salt structure. Undoped crystals have a finite residual electron concentration due to the predominance of Zn interstitials and O vacancies as intrinsic defects. While this favours the formation of the 2DES, it represents a challenge to attaining p -type crystals and therefore no ZnO-based two-dimensional hole systems (2DHS) have been reported. Various growth methods and p -doping elements (such as N, P, As, and Sb) were used in an effort to obtain high-quality ZnO crystals, however the results seem to lack reproducibility [76].

The heterostructures studied in this thesis were obtained using a molecular beam epitaxy apparatus dedicated for ZnO. Details on the growth procedure as well as in-depth characterization of the samples can be found in Refs. [61, 77]. A 250

For heavy holes, in the out-of-plane direction $g_{\perp} \sim 0.01 - 0.04$, however some reports suggest it is vanishingly small [64, 65, 66]. The in-plane component was found in the range $g_{\parallel} \sim 2 - 2.5$ [64, 67]. Further complexity is added by mixing of heavy and light holes.

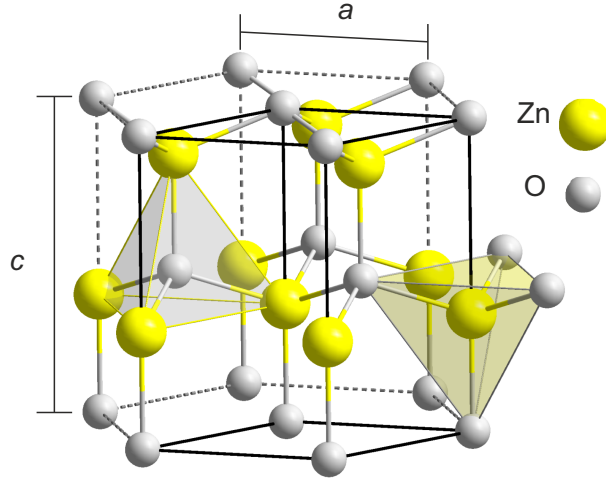


Figure 1.9: Crystal structure of wurtzite ZnO with the lattice constants a and c indicated [73].

nm layer of ZnO followed by 250 nm of $\text{Mg}_x\text{Zn}_{1-x}\text{O}$ were epitaxially deposited on single-crystal ZnO substrates. As explained above, the ionic character of the Zn-O bond leads to a finite spontaneous polarization which is larger in the cap layer than in the buffer layer. In addition, strain induces piezoelectric polarization in MgZnO . The total polarization of the system can be written:

$$\Delta P_{\text{tot}}(x) = P_{\text{spon}}(\text{Mg}_x\text{Zn}_{1-x}\text{O}) - P_{\text{spon}}(\text{ZnO}) - P_{\text{piezo}}(\text{Mg}_x\text{Zn}_{1-x}\text{O}). \quad (1.62)$$

The polarization discontinuity at the interface facilitates the accumulation of electrons in the quantum well formed due to band offset. The source of electrons is still under debate, but they likely originate from the residual bulk charge which is naturally n -type or from donors at the surface [78].

Figure 1.10 shows the Mg content x dependence of electron density and mobility for samples similar to the ones presented in this study [79]. With increasing alloying, the charge concentration increases sub-linearly. This is expected as the polarization divergence at the interface will increase with higher x . The mobility shows a peak at approximately $n = 1.4 \times 10^{11} \text{ cm}^{-2}$ and decreases abruptly at lower densities. This is likely due to reduced screening of the charged impurities in the vicinity of the 2DES. At higher electron densities, the mobility is suppressed due to the enhanced interface roughness and alloy scattering.

Photoluminescence and reflectance measurements show [80] that in the charge carrier density range presented in Fig. 1.10 electrons occupy a single subband. The energy spacing between the first two subbands as a function of electron density is plotted in Fig. 1.11(a). Self-consistent calculations suggest that the 2DES wavefunction resides mostly on the ZnO side and has a maximum width of 10 nm, as presented in Fig. 1.11(b). Recently the occupation of two subbands for $x = 0.25$ and a total density of $n = 4 \times 10^{12} \text{ cm}^{-2}$ has been observed in magnetotransport and magneto-optical measurements.

The quality of MgZnO/ZnO heterostructures has improved significantly over

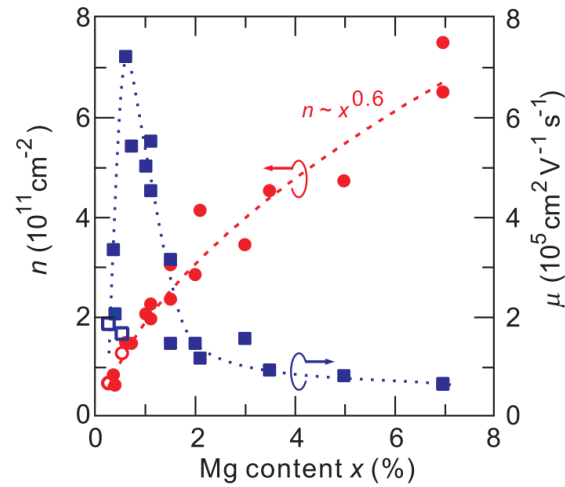


Figure 1.10: Magnesium content dependence of electron density (circles) and mobility (squares). Interface roughness and alloy scattering limit the mobility at high n , while at low n charge impurity scattering dominates. From Ref. [79]

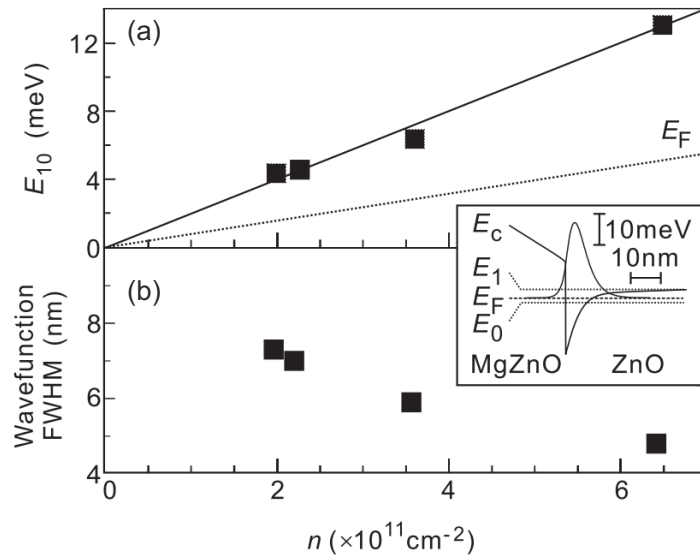


Figure 1.11: (a) Energy splitting between the lowest and the first excited subbands estimated from photoluminescence measurements as a function of electron density. (b) 2DES wavefunction full width at half maximum (FWHM) for various values of n obtained from solving the Schrödinger-Poisson equation self-consistently. Inset: schematic of the 2DES wavefunction at the MgZnO/ZnO interface. From Ref. [80]

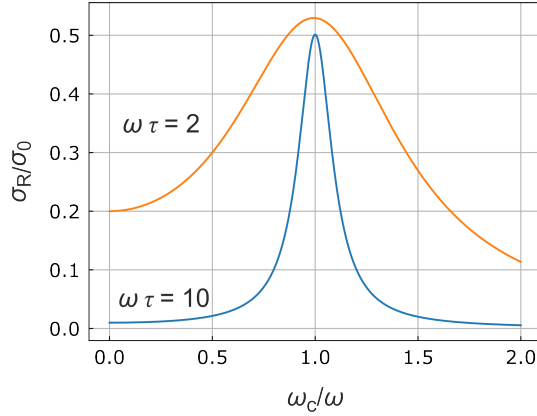


Figure 1.12: Drude model of cyclotron resonance. Power absorption reaches a maximum for $\omega_c = \omega$. The width of the lineshape is determined by $\omega\tau$.

the years and it has reached its peak mobility of just over $10^6 \text{ cm}^2 \text{ V}^{-1} \text{ s}^{-1}$ for an electron density of $n = 8.3 \times 10^{10} \text{ cm}^{-2}$ [61]. This improvement has allowed the observation of fragile even-denominator fractional quantum Hall states [81], exotic, charge-density-like physics [82], as well as a possible Wigner crystal ground state in dilute samples [83]. In this thesis we will explore magnetotransport and microwave-induced phenomena in MgZnO/ZnO heterostructures similar to the ones studied in these reports.

1.4 Cyclotron resonance (CR) and magnetoplasmons (MPs)

In the presence of a perpendicular magnetic field electrons perform cyclotron orbits with the rate $T_c = 2\pi/\omega_c = 2\pi m/eB$. If electromagnetic radiation of frequency $\omega = \omega_c$ is applied, the system absorbs energy from the oscillating electric field resonantly. Classically the equation of motion reads:

$$m \left(\frac{d\mathbf{v}}{dt} + \frac{\mathbf{v}}{\tau} \right) = e (\mathbf{E} + \mathbf{v} \times \mathbf{B}). \quad (1.63)$$

Assuming that \mathbf{B} points in the z -direction and that the radiation is linearly polarized $\mathbf{E} = E_x \exp(i\omega t)$, we can solve for v_x to obtain the dynamic conductivity:

$$\sigma_{xx} = \sigma_0 \left[\frac{1 + i\omega\tau}{1 + (\omega_c^2 - \omega^2)\tau^2 + 2i\omega\tau} \right]. \quad (1.64)$$

The static conductivity σ_0 is given by Eq. 1.3. The real component σ_R of σ_{xx} , which represents the losses due to absorption, is given by:

$$\frac{\sigma_R}{\sigma_0} = \frac{1 + (\omega_c\tau)^2 + (\omega\tau)^2}{[1 + (\omega_c\tau)^2 - (\omega\tau)^2]^2 + 4(\omega\tau)^2}. \quad (1.65)$$

From Eq. 1.65 we can infer the following:

1. In order to observe the resonance, the condition $\omega_c\tau > 1$ should be met; this is equivalent to the requirement that electrons perform at least one cyclotron orbit between two scattering events.
2. Maximum absorption occurs at $\omega = \omega_c$; for linearly polarized light and $\omega\tau \gg 1$, the real part of the dynamic conductivity is half of the static conductivity: $\sigma_R/\sigma_0 = 1/2$.
3. The lineshape of the resonance is a Lorentzian with a half-width determined by $\Delta\omega = 1/\tau$.

Figure 1.65 illustrates the real component of the conductivity as a function of the cyclotron frequency in units of ω . Two different values of $\omega\tau$ are used for comparison. In typical cyclotron resonance (CR) experiments, the radiation frequency is fixed, while the transmission through the sample is measured as a function of the applied magnetic field. The transmission signal $T(B)$ displays a minimum at resonance, as $\sigma_R/\sigma_0 \propto 1 - T(B)/T(0)$ [84]. Another convenient way to detect CR is by measuring the conductivity change of the system as the electron temperature increases due to resonant energy absorption. The photoconductivity signal can be expressed as $(\partial\sigma/\partial T)\Delta T$ and thus depends strongly on the sensitivity of σ on temperature.

At high magnetic fields the classical description of the cyclotron resonance from Eq. 1.65 is no longer valid. This is due to the fact that in the Drude model the B -dependence of the density of states is not taken into account. The problem of the CR line shape is discussed by Ando in Ref. [85]. The results depend on the nature of the scatterers [86]. In the case of short-range disorder, the width of the resonance line varies with the Landau level width. Thus it directly reflects the quantum lifetime τ_q . For long-range scatterers, the line shape depends on the difference between the width of adjacent LLs.

The quantum mechanical approach to the cyclotron resonance is centred around single-particle excitations from a filled LL to a neighbouring LL with empty states. The transition occurs when an electron absorbs a photon of energy E_c , where $E_c = \hbar\omega_c$ is the LL spacing. Since a photon carries an angular momentum of $m_J = 1$, the transition is allowed only when the initial and the final states are in adjacent LLs and if the spin of the electron is conserved. Spin-flip excitations within the same LL have energies equal to the Zeeman splitting and will be discussed later in this chapter.

In the absence of an external magnetic field, the radiation induces oscillations of the 2DES system as a whole [87]. The dispersion relation of the so-called plasmon resonance is given by [88]:

$$\omega_p^2 = \frac{ne^2}{2\epsilon m}q, \quad (1.66)$$

where q is the plasmon wave vector and ϵ is the dielectric constant. In a finite-size sample plasmons do not freely propagate, but are confined by the boundaries of the system. The smallest q -vector corresponding to a sample of length L is $q = \pi/L$. At finite magnetic field the cyclotron resonance can hybridize with the plasma oscillations to form magnetoplasmons (MPs). The dispersion relation becomes:

$$\omega^2 = \omega_p^2 + \omega_c^2. \quad (1.67)$$

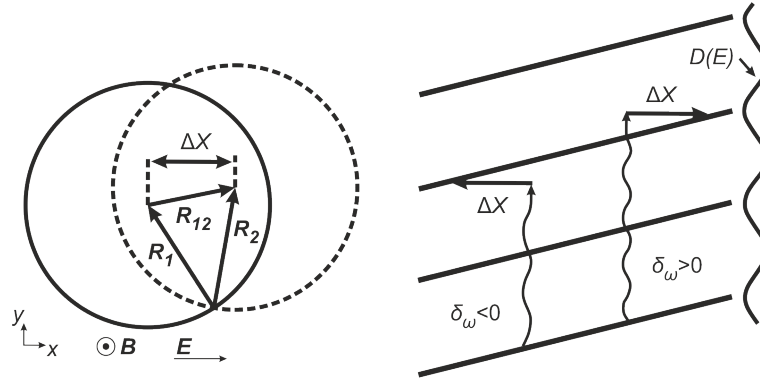


Figure 1.13: Schematic of the displacement mechanism. Left panel: the shift of the cyclotron guiding centre due to scattering. Right panel: absorption of a photon of frequency $\omega = \omega_c(\delta_\omega - 2)$ assisted by the scattering event. A positive (negative) detuning δ_ω leads to an increase (decrease) in the longitudinal resistance. Modified from Ref. [90]

According to the above equation, in a system of finite size the MP spectrum is gapped: a minimum energy of ω_p is required to excite plasmons. In the limit $L \rightarrow \infty$, this energy tends to zero. At high magnetic field, the MP dispersion line approaches the cyclotron frequency.

CR is a convenient tool to determine the effective mass of charge carriers by virtue of the resonance condition. According to Kohn's theorem [89], in an isotropic system with parabolic energy dispersion, excitations under uniform radiation are not modified by inter-particle interactions. Therefore the effective mass obtained in CR experiments corresponds to the band mass of the system. Since the carrier mass of most heterostructures under study have $m > 0.06$ (see Table 1.1), the cyclotron frequency falls in the microwave and infrared range for magnetic field strengths routinely achieved in experimental setups ($B \approx 0 - 10$ T).

1.5 Microwave-induced resistance oscillations (MIRO)

In the previous section we have seen that CR is the typical response of a 2DES subject to a magnetic field and radiation of frequency $\omega = \omega_c$. However an additional phenomenon was found in high-mobility samples, namely the appearance of resistance oscillations upon illumination. As in the case of CR, the relevant energy scale is $\hbar\omega_c$, which leads to the name microwave/THz-induced resistance oscillations (MIRO or TIRO, depending on the frequency range used). Its observation has triggered intense theoretical efforts to explain the driving mechanisms. A comprehensive review in a unified theoretical framework can be found in Ref. [90]. Here we restrict the discussion to a qualitative description of the effect.

Unlike in the case of cyclotron resonance where a single absorption peak is expected at $\omega = \omega_c$, MIRO displays oscillations in the longitudinal resistance with a period given by the ratio $\epsilon = \omega/\omega_c$. Generally the oscillations extrema are symmetrically shifted from the CR harmonics. The maxima (minima) are offset to higher

(lower) B -fields with respect to integer ϵ by a quarter of a cycle [91]. The amplitude is exponentially damped at low magnetic field. As a function of magnetic field, the change in the longitudinal resistance δR_{xx} follows the equation:

$$\delta R_{xx} \propto -A_\omega \sin(2\pi\epsilon) \exp(-2\pi/\omega_c \tau_q^{\text{MIRO}}), \quad (1.68)$$

where τ_q^{MIRO} denotes a quantum scattering time characteristic to MIRO and is of the order of the quantum lifetime. The amplitude A_ω is a function of microwave power and, depending on the dominant scattering mechanism, can vary with temperature.

Most characteristics of MIRO can be explained through a combination of two mechanisms: the displacement mechanism and the inelastic mechanism. The former, which relies on radiation-assisted scattering off disorder [92, 93], is depicted in Fig. 1.13. The sketch on the left represents the shift of the cyclotron orbit guiding centre ΔR_{12} following an elastic scattering event. The external electric and magnetic field are pointing in the x - and z -direction, respectively. The net effect of the E -field is to tilt the energy spectrum, as shown in the right panel of Fig. 1.13. If the electron scatters and concomitantly absorbs a photon of energy $\hbar\omega$, it can be promoted to a higher Landau level. Since this is a non-resonant process, the change in the Landau level index ΔN can be higher than one. If the detuning between the cyclotron energy and the photon energy $\delta_\omega = \omega/\omega_c - \Delta N$ is positive, scattering events which correspond to a displacement ΔX in the same direction as the electric field dominate. This leads to a diminished DC current I_x which in turn corresponds to an increase in resistance. The reverse applies in the case of a negative detuning: displacements against the electric field prevail which enhance the DC current and reduce the longitudinal resistance. For fixed microwave frequency and a monotonically increasing magnetic field, the resistance oscillates as the detuning changes sign periodically. In the regime of overlapping Landau levels, where the density of states can be approximated as periodic, $D(E) = D(E + N\hbar\omega_c)$, MIRO is well described by Eq. 1.68 with the amplitude independent of temperature. Theoretical work [94, 95, 96] suggests that the displacement mechanism dominates when a sufficient amount of short-range scatterers is present, or at high microwave power and temperatures.

In some high-mobility samples where elastic impurity scattering is less frequent, the displacement mechanism contributes little to the observation of MIRO. Instead the effect is present due to the so-called inelastic mechanism [97, 98]. In this case the MIRO occurs due to a non-equilibrium distribution function $f(E)$ upon illumination, which in turn is related to the oscillating density of states. A schematic of the inelastic mechanism is shown in Fig. 1.14. The distinctive characteristic of this mechanism is that the corresponding change in DC conductivity is proportional to the inelastic relaxation time τ_{in} . This is associated with a temperature dependent amplitude A_ω . Since most inelastic scattering processes occur with phonons, this mechanism dominates at low temperatures where $\tau_{\text{in}} \gg \tau_q$.

Although the presented models describe well most features of MIRO, they do not explain its insensitivity to radiation polarization handedness [99]. Moreover, the current formalism cannot account for the effect of electron-electron interactions, which, in accordance with the Fermi liquid theory, leads to mass renormalization [100, 101]. In an effort to approach these inconsistencies, a few other models have

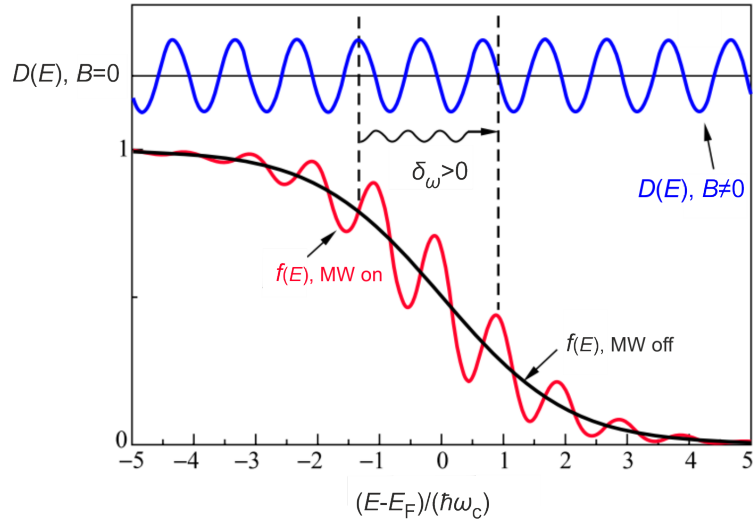


Figure 1.14: Schematic of the inelastic mechanism. The distribution function $f(E)$ gains an oscillatory component due to the oscillating density of states in a magnetic field and to microwave illumination. This leads to a correction to the resistance which is periodic in ω/ω_c . From Ref. [90]

emerged, some of which are also based on a bulk effect [94, 102, 103, 104], while others suggest that MIRO emerges from either the edges [105] or from the metallic contacts or pads on the sample [106, 107]. Measurements performed on Corbino disks have rebutted MIRO as an edge effect [108]. Moreover its observation on contactless samples shows that a contribution from metallic structures can also be neglected [109, 110].

1.6 Electron spin resonance (ESR)

An electron possesses spin angular momentum \mathbf{S} which is associated with a magnetic moment:

$$\boldsymbol{\mu}_S = -g\mu_B \frac{\mathbf{S}}{\hbar}, \quad (1.69)$$

where we denoted the spin g -factor as g which in free space is approximately equal to 2. Since the spin of an electron is $1/2$, the projection of the spin angular momentum along any given axis can take on two values: $+\hbar/2$ or $-\hbar/2$. These two components are generally referred to as spin up ($-1/2$) and spin down ($+1/2$). From Eq. 1.69 we notice that the magnetic moment is antiparallel to the angular momentum. This is due to the negative charge of electrons. When an external magnetic field is applied, the degeneracy between the two spin states is lifted. The energy splitting, called the Zeeman energy, is given by:

$$E_Z = -2\boldsymbol{\mu}_S \cdot \mathbf{B} = g\mu_B B. \quad (1.70)$$

Electron spin resonance is the measurement in which one probes the Zeeman energy. For a free electron, $E_Z \approx 0.12$ meV for $B = 1$ T, which falls in the microwave range. In a crystal, the g -factor can vary from the free-space value due to spin-

orbit coupling, crystal field or hyperfine interaction. Careful examination of the paramagnetic resonance provides information on how these phenomena affect the energy spectrum. The resonance signal is typically measured using sensitive ESR spectrometers, which require positioning the sample inside a resonance cavity and detecting the radiation which passes through this cavity. A detailed description of these techniques can be found in Ref. [111].

To perform an ESR measurement, it is necessary that the system of study contains unpaired (paramagnetic) spins. An external magnetic field $\mathbf{B} = B\mathbf{z}$ creates a torque $\boldsymbol{\mu}_S \times \mathbf{B}$, which causes the direction of $\boldsymbol{\mu}_S$ to precess around \mathbf{B} . The rate of precession is given by the Larmor frequency $\omega_L = g\mu_B B/\hbar$. Applying a radiation field with a frequency equal to ω_L and an oscillating B -field in the xy -plane causes the spins to tip and eventually flip signs. This process is schematically depicted in Fig. 1.15 and can work both ways: a spin up can be flipped to a down-state and the other way around.

In a two-level system picture (see Fig. 1.16), the paramagnetic resonance can be understood as a transition between states of opposite spins upon absorption or emission of photons with energy E_Z . To excite electrons from the lower to the higher energy branch, a spin population difference is required, which at finite temperature T is given by the Boltzmann probability expression:

$$\frac{N_+}{N_-} = \exp(-\hbar\omega_L/k_B T), \quad (1.71)$$

where N_+ and N_- are the number of electrons with spin-up and spin-down, respectively. To improve the ESR signal, it is thus necessary to have $\hbar\omega_L \gg k_B T$. All experiments presented in this thesis were performed in this regime.

If spins were completely isolated excitations would have an infinite lifetime and the population difference would tend to zero. In real systems, however, fluctuations in local effective magnetic field, often caused by spin-orbit interaction (SOI) lead to a finite spin lifetime. Among the most common relaxation mechanisms one can name Elliott-Yafet [112], Dyakonov-Perel [113], and the relaxation via hyperfine interaction with nuclear spins. In experiments, one can distinguish between the relaxation time of the spin component parallel to the direction of the static B -field from the one perpendicular to it. Correspondingly, the two quantities are named the longitudinal relaxation time (T_1) and the transversal relaxation time (T_2). In practice, while T_1 can be in some cases extracted from the width of the ESR line, one would have to employ the pulse electron spin resonance technique to measure T_2 .

As seen in Section 1.2, the g -factor of a system can be renormalized by correlations. According to Yafet [114], for a parabolic 2DES in an isotropic RF field the position of the ESR line is not affected by inter-particle interactions. Thus in a paramagnetic resonance experiment, one would obtain the bare effective g -factor. Exceptions from this theory are expected to occur in systems where the SOC is present [115].

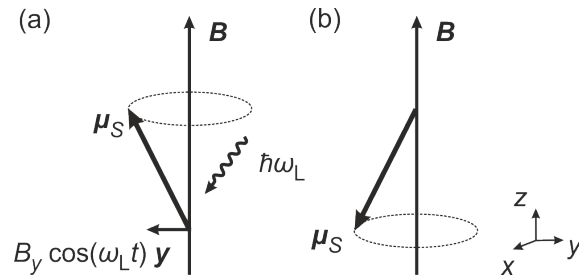


Figure 1.15: The spin magnetic moment precesses around \mathbf{B} with the Larmor frequency ω_L . Resonant absorption of the B -field component of the radiation field causes the magnetic moment to flip.

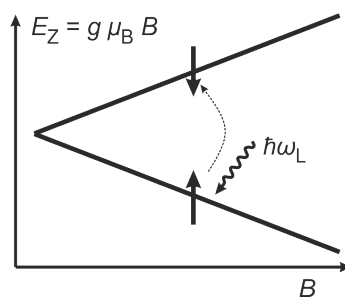


Figure 1.16: A static magnetic field leads to the Zeeman splitting between opposite spin levels. Photons with frequency equal to the Larmor precession frequency can excite electrons between the two states.

Chapter 2

The two-dimensional electron liquid

The 2DES in MgZnO/ZnO heterostructures offers a fruitful platform for the exploration of inter-particle correlations, due to the dominance of the average Coulomb energy over the kinetic energy of particles at the Fermi surface, while disorder plays a marginal role. One manifestation of many-body interactions is the renormalization of the electron effective mass and g -factor, quantities which enter the cyclotron and the Zeeman energy, respectively. In this chapter we explore the accessibility of these parameters through transport measurements and by analysing the microwave-induced effects. A close-up of the microwave response in the form of cyclotron resonance, microwave-induced resistance oscillations and electron spin resonance further the understanding of the 2DES under study.

2.1 Methods

This chapter focuses on the transport properties and the microwave response of various MgZnO/ZnO heterostructures. For studying the response to microwaves we have employed two measurement techniques, namely resistive detection and transmission. The details of each method can be found in Section 2.3.1 of this chapter.

We measured a set of 17 samples with different charge carrier concentrations in the range $2 \times 10^{11} \text{ cm}^{-2} \leq n \leq 20 \times 10^{11} \text{ cm}^{-2}$. The electron density was determined by the Mg content in the cap layer. Based on Fig. 1.10 we approximate that the corresponding alloy content spanned the interval $0.01 \leq x \leq 0.15$. The lateral size varied from sample to sample, but all chips were approximately square and had at least four contacts such that four-point measurements in the Van der Pauw configuration were possible. Soldered indium in the chip corners constituted the contacts.

The experimental setup is shown in Fig. 2.1. A small hole approximately 5 mm in diameter was drilled through the middle of the chip carrier. The top side was then covered with a transparent mylar film to which the ZnO sample was glued. Additionally we used metallized mylar around the perimeter of the sample to ensure that radiation only passes through the chip. On the backside of the carrier we placed a $4 \times 3 \text{ mm}^2$ carbon-covered kapton film with silver paste contacts. It served as a resistor R_t exhibiting a strong temperature dependence. Its bolometric response provided a measure of the microwave power transmitted through the sample containing the 2DES.

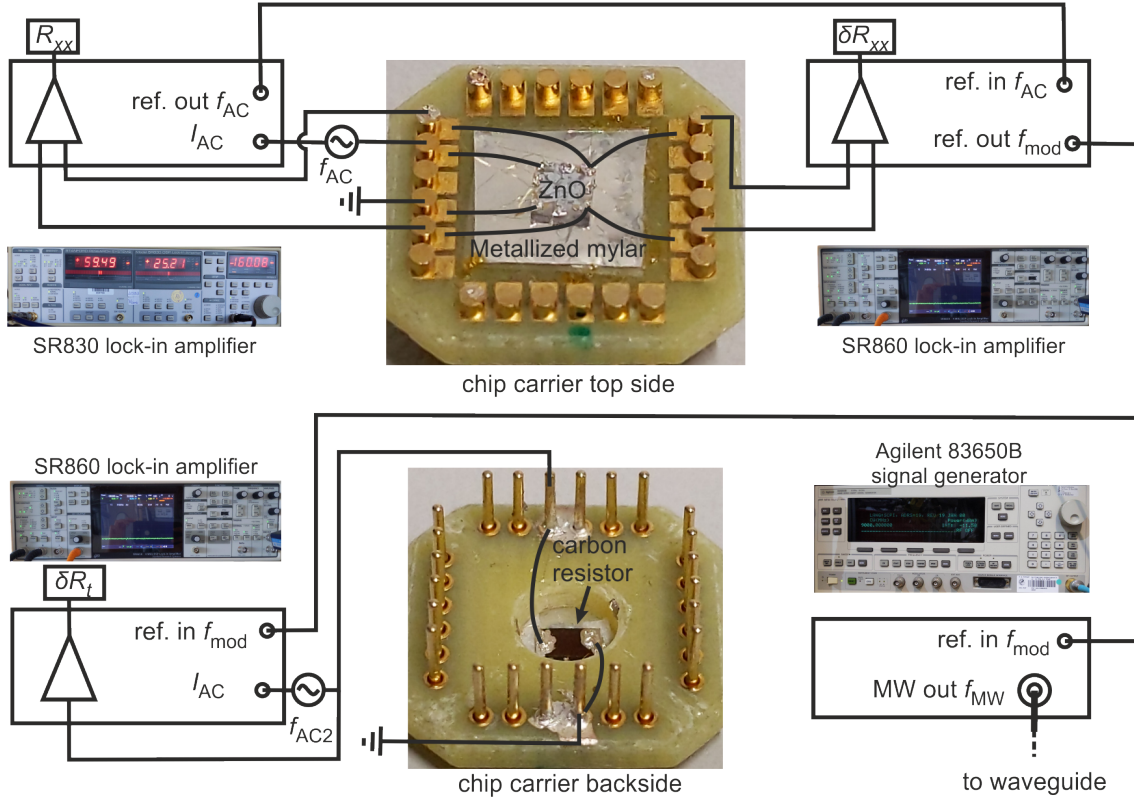


Figure 2.1: Sketch for the experimental setup used to perform simultaneous transmission and photoresistive measurements.

The measurements were carried out in a single shot ^3He cryostat, capable of reaching a base temperature of $T \approx 300$ mK. The cryostat was equipped with a 15 T superconducting coil. An Agilent 83650B signal generator produced monochromatic radiation with frequencies $f_{MW} \leq 50$ GHz. Virginia Diode frequency multipliers were used to access higher frequencies in the range $f_{MW} = 75 - 170$ GHz. The microwaves were carried to the device through a flexible coaxial cable connected to a rectangular rigid waveguide which stretched from the top of the sample holder to the sample space. The output power varied with frequency and was no higher than 10 mW at the input of the rigid waveguide.

The resistance R_{xx} of the 2DES was measured in a four-point configuration using a Stanford Research Systems SR830 lock-in amplifier. The bias AC current $I_{AC} = 500$ nA oscillated at a frequency of $f_{AC} \approx 13$ Hz. To improve detection of the microwave response, we employed the dual modulation technique. The output radiation was amplitude modulated at a frequency of $f_{mod} = 1$ kHz. The dual function of a SR860 lock-in amplifier was then used to directly measure the photoinduced resistance component δR_{xx} which is modulated both at f_{AC} and at f_{mod} . This method ensured that minute changes in the resistance due to microwave absorption could be detected. The same technique was used to measure the microwave response δR_t of the carbon resistor. All samples presented in this chapter were characterized through photoresistive measurements. Transmission experiments have been carried out on a set of four samples with different carrier concentrations such that they covered the entire range of interest.

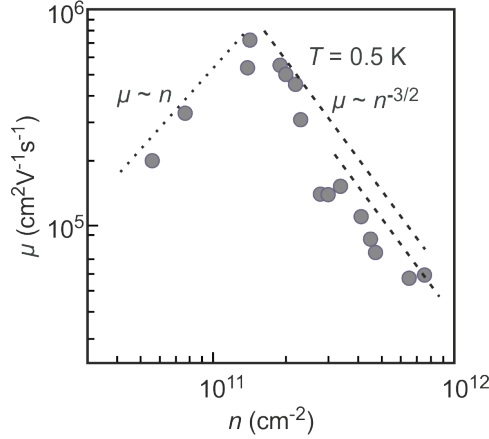


Figure 2.2: Mobility as a function of density in a number of ZnO-based 2DESs. The dotted and dashed lines are guides for the $\mu \sim n$ and $\mu \sim n^{-3/2}$ laws corresponding to charged impurity and interface roughness scattering, respectively. Adapted from Ref. [79].

2.2 Transport characterization

2.2.1 Carrier mobility

The state-of-the-art ZnO-based 2DESs studied in this thesis owe their high quality to the advances made along the years in identification and control of defects upon crystal growth [61]. This progress has allowed the observation of various phenomena which otherwise would have been obscured by strong disorder [81, 82, 83]. One measure of sample quality is the carrier mobility, μ , which in practice can be estimated using the 2DES resistivity ρ and carrier density n :

$$\mu = \frac{1}{ne\rho}. \quad (2.1)$$

Figure 2.2 summarizes the mobility as a function of carrier density for samples with similar properties as the ones characterized in this chapter [79]. The measurements were performed at $T = 0.5$ K. Hence phonon scattering is negligible. On the high density end, the mobility follows an approximate $n^{-3/2}$ law (dashed lines). This dependence has been attributed to alloy scattering and interface roughness [116], which is stronger at high n due to the wave function penetrating further into the barrier. As the carrier concentration is reduced below $n \approx 1.5 \times 10^{11} \text{ cm}^{-2}$, the screening of disorder becomes less efficient, thus leading to a linear decrease of the mobility with n [117]. The focus of this chapter are systems with an electron density in the range of $2 \times 10^{11} \text{ cm}^{-2} \leq n \leq 20 \times 10^{11} \text{ cm}^{-2}$. The corresponding mobilities in this density range vary between $10^4 < \mu < 7 \times 10^5 \text{ cm}^2 \text{ V}^{-1} \text{ s}^{-1}$.

2.2.2 Magnetotransport and electron liquid parameters

Standard lock-in amplifier measurements have been employed for magnetotransport characterization of all samples studied in this chapter. In particular, we have extracted the carrier density from the period of SdHO at low temperatures. Occa-

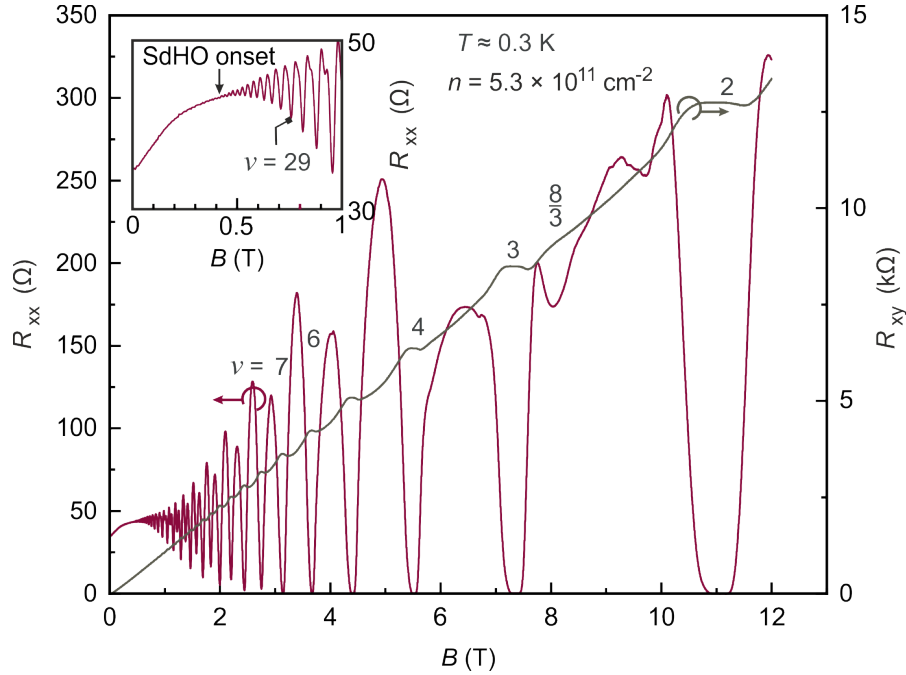


Figure 2.3: Magnetotransport traces for a 2DES with $n = 5.3 \times 10^{11} \text{ cm}^{-2}$ recorded at $T \approx 0.3 \text{ K}$. Inset: low-field SdHO. The arrow marks the onset of the oscillations.

sionally the Hall resistance was monitored for the same purpose. The onset of the SdHO provided an estimate for the quantum lifetime τ_q , by virtue of Eq 1.33. Typical longitudinal (red line) and transversal (black line) resistance traces are shown in Fig. 2.3 recorded for a sample with $n = 5.3 \times 10^{11} \text{ cm}^{-2}$ at $T = 0.3 \text{ K}$. The main plot shows R_{xx} and R_{xy} for magnetic fields up to $B = 12 \text{ T}$. Pronounced QH states up to $\nu = 7$ are marked. Some signatures of an incipient fractional quantum Hall state at $\nu = 8/3$ can also be identified. In the inset the low field resistance oscillations in R_{xx} are displayed. The arrow marks the onset of the SdHO at $B \approx 0.4 \text{ T}$, which corresponds to $\tau_q = 2 \text{ ps}$. Only minima corresponding to odd filling factors are visible at such low B -values, reflecting that the Zeeman splitting is comparable in magnitude with the cyclotron energy.

Due to the nature of the excitations responsible for conduction which typically involve electron-hole pairs with wave-vectors $\vec{k} \rightarrow \infty$, the effects of electron-electron interaction are directly visible in transport measurements. One such example is the fractional quantum Hall effect (FQHE) where electrons and magnetic flux quanta assemble into new quasi-particles in order to screen the Coulomb repulsion [4]. The FQHE can be understood in terms of the composite fermion theory. Strong correlations are present in transport also through the renormalization of measurable quantities such as the carrier effective mass, m^* , the g -factor, g^* , and the spin susceptibility $\chi^* \sim g^* m^* / m_0$. Interaction-induced parameter renormalization can be phenomenologically explained by the Fermi liquid theory (see Section 1.2.1 for details). In practice, the renormalized mass m^* can be obtained by analysing the temperature dependence of the SdHO [118]. Several works have reported the value of m^* in ZnO-based systems [119, 120, 121]. In Fig. 2.4 we replot m^* from Ref. [121] as a function of carrier concentration and interaction parameter. The horizontal

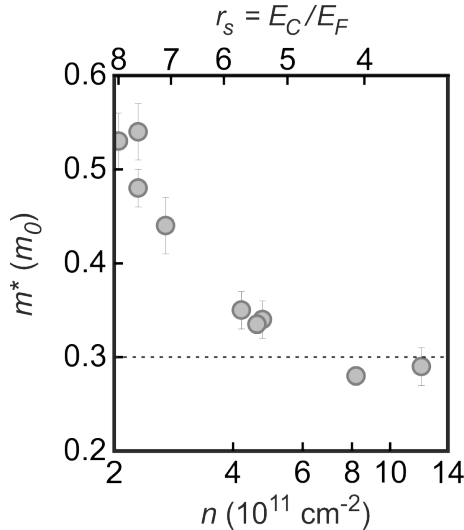


Figure 2.4: Electron liquid mass m^* obtained from the temperature dependence of SdHO as a function of charge carrier density n and interaction parameter r_s . Dashed line marks the band effective mass in bulk ZnO. Adapted from [121].

dashed line marks the bare mass in ZnO, $m = 0.3m_0$ [62]. At high density ($n > 12 \times 10^{11} \text{ cm}^{-2}$), the quasi-particle transport mass is approximately equal to the band mass. As the density is reduced and interactions grow stronger, m^* first falls below the bare value and then increases systematically down to the lowest accessible n . Both the reduction and the increase in m^* have been reported in other materials [15, 118, 122] and can be qualitatively explained as a manifestation of many-body effects within the Fermi liquid paradigm [14, 17].

In transport measurements the dimensionless quasi-particle spin susceptibility, g^*m^*/m_0 , can be estimated by employing the coincidence method [123] or from the parallel magnetic field required to polarize the 2DES [124, 125]. Using the independently measured m^* , one can calculate the renormalized g -factor. It turns out that in ZnO g^* varies only little with electron density and it is approximately twice as large as the band value, $g \approx 2$ [121]. A similar behaviour was observed in Si-based 2DESs [122].

2.3 Cyclotron resonance and magnetoplasmons

Cyclotron resonance (CR) is a tool which is routinely used for determining electronic properties of charge carrier systems in the presence of an external static magnetic field and an alternating electric field [126]. Among the most common quantities which can be studied with CR are the carrier type and concentration, cyclotron mass and scattering time. By studying the cyclotron mass one can obtain details on the non-parabolicity of the band structure and polaron coupling [84, 127].

According to Kohn's theorem [89], in a translationally invariant system uniform radiation can only couple with the centre-of-mass coordinate such that the cyclotron resonance is unaffected by inter-particle correlations. Due to the small momentum of incident photons, CR excitations are characterized by electron-hole pairs with vanishing wave vectors $\vec{k} \rightarrow 0$. The theorem is violated in systems

with non-parabolic band structure where translational invariance is broken [128] and where, consequently, carrier-carrier interactions modify the cyclotron resonance spectrum [129]. Disorder and finite sample size are known to have a similar effect [130, 131]. Translational symmetry breaking can also be achieved artificially, by modulating the charge carrier density through the excitation of surface acoustic waves (SAWs). This method has been successfully employed to study the mass of composite fermions which originates entirely from Coulomb interactions [132]. Another way to bypass Kohn's theorem is by modulating the incident radiation field with the help of metallic grating patterned on the surface of the device [133]. Both SAWs and the grating coupler allow a systematic study of CR dispersion as a function of the wave vector \vec{k} , where $|\vec{k}|$ is determined by the periodicity of the grating or the wavelength of the SAW.

Previously CR was observed in ZnO-based 2DESs by recording the photoluminescence spectra with and without microwaves [134, 135]. By analysing the dispersion relation $f_{\text{MW}}(B_{\text{res}})$ the authors have extracted the electron effective mass which showed an increase with increasing density. The rise was attributed to non-parabolicity effects in conjunction with strong Coulomb interactions. In this section we revisit the density-dependent CR experiments in ZnO heterostructures and analyse the finite-size effects which lead to the hybridization of the Kohn mode with magnetoplasma oscillations.

2.3.1 Detection scheme

CR experiments were performed using two detection methods. The first was transmission which was achieved by monitoring the resistance of a carbon resistor placed underneath the ZnO sample, as illustrated in Fig. 2.1. Its resistance R_t increased significantly as the temperature was reduced below 4 K. At base T , upon irradiation with microwaves R_t dropped, indicating a strong negative bolometric response:

$$\delta R_t(B) = -CT_s(B)P_{\text{ext}}. \quad (2.2)$$

In the equation above C is a parameter characterising the sensitivity of the resistor to the microwave power P_{ext} and $T_s(B)$ is the transmission coefficient. Both C and P_{ext} are B -independent. Therefore in a magnetic field, the variations of $\delta R_t(B)$ directly reflect the B -dependence of the transmission coefficient.

Figure 2.5 shows the representative microwave response of the carbon resistor in a magnetic field for a sample with $n = 7.2 \times 10^{11} \text{ cm}^{-2}$. The bath temperature was $T = 1.4 \text{ K}$. In the absence of microwave radiation the resistor displays a weak negative magnetoresistance. Upon illumination with monochromatic microwaves of frequency $f_{\text{MW}} = 95 \text{ GHz}$, the whole $R_t(B)$ trace shifts to lower values due to heating induced by absorption of radiation which passed through the ZnO sample. At magnetic field values where the cyclotron resonance condition $\omega_c = \pm 2\pi f_{\text{MW}}$ is satisfied the 2DES absorbs and/or reflects most of the radiation, leading to the cooling of the carbon resistor. This results in two evident peaks positioned symmetrically with respect to $B = 0$.

While the example shown in Fig. 2.5 demonstrates that the resonance field can be extracted directly from $R_t(B)$ traces, in most cases the CR signal is too weak to be

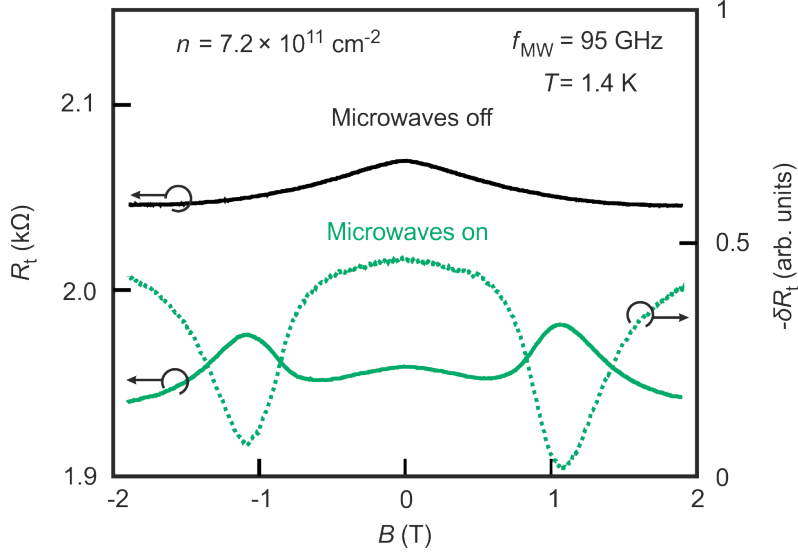


Figure 2.5: Demonstration of the transmission measurement technique using a carbon resistor for a 2DES with $n = 7.2 \times 10^{11} \text{ cm}^{-2}$. The microwave frequency was fixed to $f_{\text{MW}} = 95 \text{ GHz}$ and the temperature was $T = 1.4 \text{ K}$. The bolometer magnetoresistance curve $R_t(B)$ shifted to lower values when the microwaves were switched on. Additionally two peaks appear, their positions corresponding to the CR condition. The strong bolometric response δR_t was detected using the dual-modulation technique. Its negation reflects the B -dependence of the transmission.

clearly identified. The signal strength depends on the radiation power that reaches the sample, which in turn varies significantly with radiation wavelength. This is due to the output power determined by the device construction as well as standing waves forming along the waveguide. To improve the signal to noise ratio, we use the dual-modulation technique and recorded the change $\delta R_t(B)$ due to microwaves directly. The measured transmittance $T_s(B) = -\delta R_t(B)$ is plotted in Fig. 2.5 with dotted line.

The second method which we employed for CR detection relies on the bolometric effect of the 2DES itself [136]. In this approach, the system absorbs energy from the microwave field which leads to an increase in electron temperature. The microwave induced heating can be expressed as $(\delta R_{xx}/\delta T)\Delta T$ and therefore reflects the sensitivity of the sample resistance to temperature.

We measured the microwave response δR_{xx} of the 2DES utilizing the dual-modulation technique illustrated in Fig. 2.1. In Fig. 2.6 we plot example traces at different radiation frequencies for a sample with $n = 2.05 \times 10^{11} \text{ cm}^{-2}$ (dashed lines). A strong peak is observed in each curve which is aligned with the minimum measured concomitantly using the transmission scheme (solid lines). We can therefore associate the peaks in δR_{xx} with resonant absorption of microwaves and heating of the 2DES at CR.

Although the resistive detection of CR is convenient as it simplifies the experimental setup, the method cannot be applied in samples with $n \geq 4.7 \times 10^{11} \text{ cm}^{-2}$ where no resonant features in δR_{xx} were observed. In contrast, we were able to measure CR in the transmission signal over the whole range of charge carrier concentrations of interest. The disappearance of CR in δR_{xx} is accompanied by the

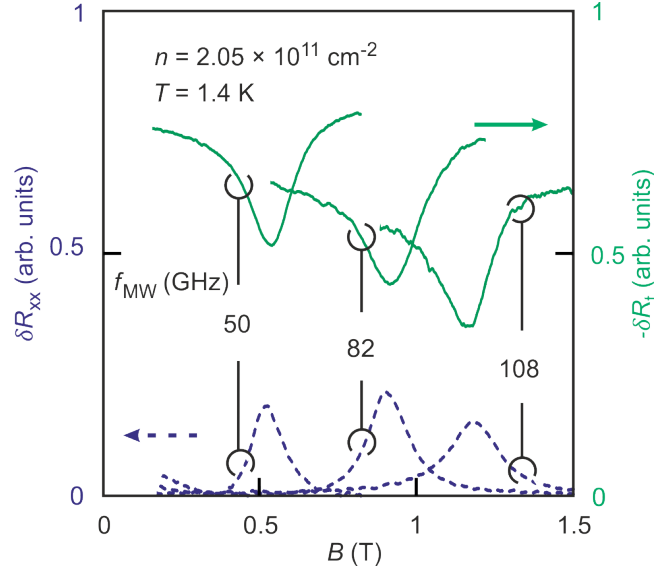


Figure 2.6: Magnetotransmission data $-\delta R_t(B)$ (solid lines) and photoresistance $\delta R_{xx}(B)$ for three different microwave frequencies (as marked) measured at $T = 1.4$ K on a sample with $n = 2.05 \times 10^{11} \text{ cm}^{-2}$. Curves are shifted vertically for clarity.

emergence of another radiation-related effect, namely microwave-induced resistance oscillations (MIRO). A detailed analysis of this phenomenon will be given in the next section.

As discussed above, the strength of the 2DES bolometric response depends on the temperature sensitivity $\delta R_{xx}/\delta T$ of its resistance. It is therefore tempting to attribute the distinct microwave response in low- and high- density samples with the different $R(T)$ profiles in the two charge carrier concentration regimes. In Fig. 2.7 we compare the $R(T)$ traces for two samples with densities $n = 2.3 \times 10^{11} \text{ cm}^{-2}$ and $n = 7.5 \times 10^{11} \text{ cm}^{-2}$ in the absence of microwaves and magnetic field. Both systems display a metal-like behaviour with $dR/dT > 0$. The resistance of the high density system bottoms out below $T \approx 1$ K, while in the low density sample R continues to decrease as T is reduced down to base temperature $T_{\text{base}} \approx 300$ mK. Since our CR measurements are performed at $T \leq 1$ K, we would indeed expect a greater photoresponse in the lower density samples.

2.3.2 Frequency dependence

In Fig. 2.8 we present the positions of the cyclotron resonance for a set of microwave frequencies in a sample with $n = 2.3 \times 10^{11} \text{ cm}^{-2}$. The resonance field was obtained from the maximum of the photoresistive response δR_{xx} . Taking the average between the CR positions at negative and positive fields we eliminate the zero-field offset due to trapped flux in the superconducting coil. Additional errors stem from the width and the asymmetry of the CR signal. The broadening of the line shape is likely to originate from so-called radioactive decay while the asymmetry may be attributed to interference effects within the sample [137, 138]. Assuming a linear dispersion

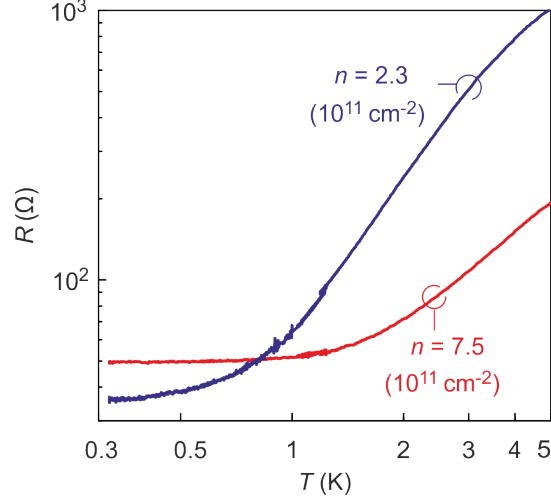


Figure 2.7: Temperature dependence of the resistance at $B = 0$ for two samples with $n = 2.3 \times 10^{11} \text{ cm}^{-2}$ (blue line) and $n = 7.5 \times 10^{11} \text{ cm}^{-2}$ (red line). CR and MIRO were dominated the photoresponse of the low- and the high-density sample, respectively.

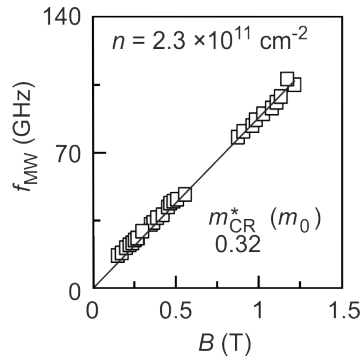


Figure 2.8: Positions of the cyclotron resonance maxima measured in δR_{xx} for a sample with $n = 2.3 \times 10^{11} \text{ cm}^{-2}$. The solid line represents a fit of the high frequency $f_{\text{MW}} \geq 75$ data to Eq. 2.3. From the slope we obtain $m_{\text{CR}}^* = (0.32 \pm 0.01)m_0$.

following the resonance condition

$$f_{\text{MW}} = f_c \equiv \frac{eB}{2\pi m_{\text{CR}}^*}, \quad (2.3)$$

we perform a linear regression with m_{CR}^* as a fitting parameter. The result is shown in Fig. 2.8 as a solid line. In this analysis we exclude data points with $f_{\text{MW}} < 75$ GHz where deviations from the linear dispersion owing to magnetoplasma oscillations occur. The obtained value of the cyclotron mass is $m_{\text{CR}}^* = (0.32 \pm 0.01)m_0$, which is close to the band mass $m_b \approx 0.3m_0$ of carriers in bulk ZnO [62].

Let us now shift our attention to the low frequency regime $f_{\text{MW}} < 50$ GHz. Here we find a systematic deviation from the linear dependence $f_{\text{MW}}(B)$. We attribute this behaviour to the hybridization of the CR with the lowest-order magnetoplasmon mode. To show that this is indeed the case, we consider the model of a clean 2DES where retardation effects can be neglected [138]. Its spectrum in a magnetic field is described by [139]:

$$f_{\text{mp}}^2 = f_p^2 + f_c^2, \quad (2.4)$$

where f_p^2 is the zero-field plasma frequency and is given by:

$$f_p^2 = \frac{ne^2}{8\pi^2 m^* \bar{\epsilon}} q. \quad (2.5)$$

In a square-shaped sample such as ours the fundamental magnetoplasmon mode corresponds to the wave vector $q = \pi/L$. Since the thickness of the sample $w \approx 0.3$ mm is much smaller than the lateral size L , we can express the effective dielectric constant $\bar{\epsilon}$ in terms of the ZnO dielectric constant $\epsilon = 8.5\epsilon_0$ as [140]:

$$\bar{\epsilon} = \frac{\epsilon_0}{2} + \frac{\epsilon}{2} \cdot \frac{\epsilon \tanh(qw) + \epsilon_0}{\epsilon + \epsilon_0 \tanh(qw)} \approx 2.23\epsilon_0. \quad (2.6)$$

In Fig. 2.9 we plot the square of the resonance positions from Fig. 2.8 against the square of the corresponding radiation frequencies. The dashed line in the main plot represents the high frequency $f_{\text{MW}} \geq 75$ GHz linear fit with zero intercept which yielded the cyclotron mass $m_{\text{CR}}^* = (0.32 \pm 0.01)m_0$. Plotted in this manner, we notice that even at lower frequencies the deviation due to magnetoplasma oscillations is barely visible. We can attribute this to the smallness of the plasma frequency, because of the large sample size. It is therefore reasonable to neglect this effect in the high frequency range.

In the inset of Fig. 2.9 a narrower range with $f_{\text{MW}} < 50$ GHz of the same data set is shown. A small positive vertical offset becomes visible, corresponding to f_p^2 . Using Eqs. 2.4 and fixing the effective mass to $m^* = 0.32$, we fit this portion of the data and obtain $f_p = 11.8$ GHz. Comparing this value with the one calculated using Eq. 2.5 we find the same value. Exact agreement between the theoretical model and experiment might also be coincidental, given the loose approximations. Despite the simplicity of the model, it appears that the spectrum can be qualitatively explained in terms of the hybridization between CR and magnetoplasma oscillations [141].

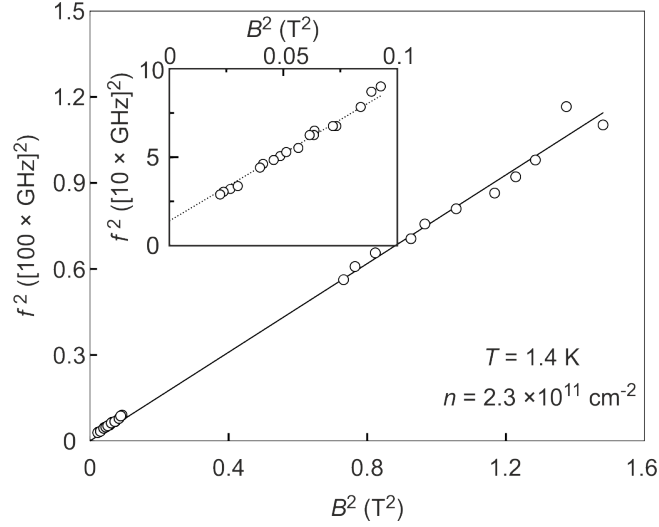


Figure 2.9: CR spectrum plotted with quadratic scales (f_{MW}^2, B^2). The main panel presents data for the entire frequency set, while the inset only includes data for $f_{\text{MW}} < 30$ GHz. The solid line in the main plot is the linear fit from Fig. 2.8. The dashed line in the inset is a linear fit to Eq. 2.4 which yields $f_p = 11.8$ GHz.

2.3.3 Density dependence

The cyclotron mass analysis described in the previous section has been performed on a set of samples of various charge carrier densities. The results obtained from both transmission (diamonds) and photoresistance (triangles) measurements are displayed in Fig. 2.10. Due to the absence of a resonant photoresponse in high-density samples, we were able to estimate the mass through transmission measurements alone for $n > 4 \times 10^{11} \text{ cm}^{-2}$. The error bars represent the standard deviation of the linear regression performed on each $f_{\text{MW}}(B)$ data set. Using only the high-frequency range of the spectrum ($f_{\text{MW}} \geq 75$ GHz), we neglected the corrections due to magnetoplasma oscillations.

Across the range of n of interest the cyclotron mass appears to be independent of electron density. The average value of $m_{\text{CR}}^* = 0.3 \pm 0.01 m_0$, shown as a horizontal dashed line, coincides with the band mass reported in bulk ZnO [62]. We therefore conclude that indeed the measured cyclotron mass is independent of many-body effects, as predicted by Kohn's theorem.

The above result contrasts with the findings in Ref. [135] where a systematic increase of the cyclotron mass with n is found. The authors attempted to explain this behaviour by taking into account non-parabolicity effects. Using the $\vec{k} \cdot \vec{p}$ model including three bands [127], the energy dependence of the effective mass is given by:

$$\frac{1}{m^*(E)} = \frac{1}{m_0^*} \left(1 + \frac{2K_2}{E_g} E \right), \quad (2.7)$$

where m_0^* is the band-edge effective mass and E_g is the band gap. The size of the non-parabolicity at electron energy E is gauged by the coefficient K_2 . Analysing the density dependence using the above equation, the parameter K_2 is estimated at -15.2 , well above the bulk ZnO value of $K_2^{\text{bulk}} = -1.2$. This discrepancy has led

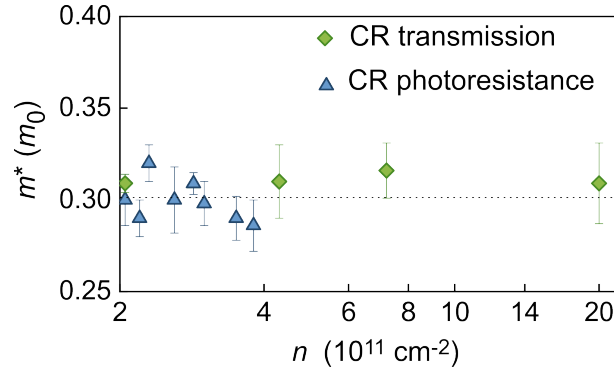


Figure 2.10: Cyclotron effective mass obtained from transmission (diamonds) and photoresistance (triangles) measurements. The horizontal dashed line marks the average value over the whole electron density range under study.

the authors to conclude that due to finite non-parabolicity of the system Kohn's theorem is invalid, thus allowing Coulomb interactions to shift the energy of the cyclotron resonance. Whether that is indeed the case still remains to be clarified. The drastically different behaviour of the cyclotron mass in this thesis compared to the one in Ref. [135] also remains a subject of debate.

2.4 Microwave-induced resistance oscillations

Upon irradiation with microwaves the photoresponse of a 2DES in a magnetic field is conventionally dominated by the heating-induced resonant absorption at CR. However in high-mobility systems a distinct effect can emerge, namely microwave-induced resistance oscillations (MIRO). Unlike CR, MIRO relies on non-resonant absorption of microwaves which allows transitions to available states in distant LLs.

From the period of MIRO, which is determined by the ratio $2\pi f_{\text{MW}}/\omega_c$, one can extract the electron effective mass. The fact that the mass thus obtained is different from the band mass was first reported in a GaAs-based 2DES by Hatke et al. in Ref. [100]. This result has triggered a series of charge carrier density dependent studies which suggest that MIRO probes the interaction-renormalized effective mass [101, 142]. Experimental studies of MIRO in ZnO 2DESs yield similar findings [143, 144, 145]. In this section we revisit the topic of MIRO mass and present concomitant transmission and photoresponse measurements. This allows a direct comparison between the bare CR mass and the correlations-sensitive MIRO mass. Additionally, we investigate the regime where both MIRO and CR are present in the 2DES photoresponse.

2.4.1 Detection

In most reports MIROs are measured as a response in the longitudinal magnetoresistance of the sample. Some signatures of MIRO in the transversal resistance have been observed [146], in qualitative accordance to theory [92]. Higher harmonics of CR in differential absorption [147] and in transmittance have also been resolved

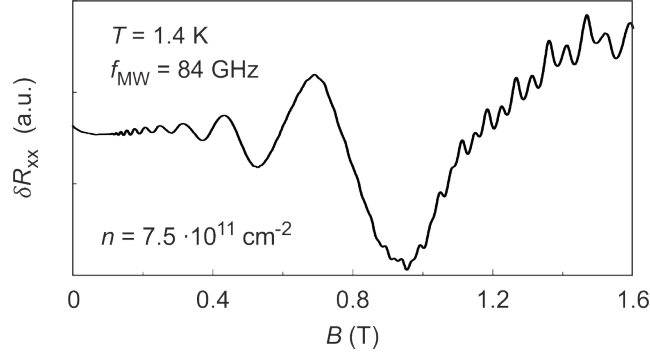


Figure 2.11: The photoresponse of a sample with $n = 7.5 \times 10^{11} \text{ cm}^{-2}$ when the microwave frequency equals 84 GHz and $T = 1.4 \text{ K}$. Prominent MIRO periodic in $1/B$ appear. At high field, $B > 1 \text{ T}$, they overlap weaker oscillations which correspond to the heating-induced modulation of the SdHO.

[148], providing evidence for MIRO-like quantum corrections to the dissipative part of the dynamic conductivity.

MIRO is also present in a set of 2DESs studied in this thesis. In some samples the modulation due to microwave radiation was sufficiently pronounced to be observed in $R_{xx}(B)$. In most cases, however, the dual-modulation technique illustrated in Fig. 2.1 was necessary to resolve the oscillations. Figure 2.11 displays a typical differential magnetoresistance trace for a sample with $n = 7.5 \times 10^{11} \text{ cm}^{-2}$ at $T = 1.4 \text{ K}$. The sample was illuminated with microwave radiation of frequency $f_{\text{MW}} = 84 \text{ GHz}$. Pronounced oscillations the amplitude of which increases with B appear at magnetic fields as low as $B = 0.1 \text{ T}$. At high field ($B \gtrsim 0.8 \text{ T}$), MIRO overlaps with another set of oscillations, which we identify as the Shubnikov-de Haas oscillations. Their appearance in δR_{xx} is due to the heating-induced modulation.

2.4.2 Determination of MIRO effective mass

In this study MIROs are well reproduced by the expression [90]:

$$\delta R_{xx} \propto -\sin(2\pi\varepsilon) \exp(-2\pi/\omega_c \tau_q^{\text{MIRO}}), \quad (2.8)$$

with the period determined by the ratio $\varepsilon = 2\pi f_{\text{MW}}/\omega_c$. The presence of the effective mass in ω_c allows us to determine its value from the position of the MIRO extrema. We denote the mass thus extracted as m_{MIRO}^* to differentiate it from the one obtained from temperature dependent SdHO measurements m_{SdHO}^* and from CR experiments m_{CR}^* .

Figure 2.12 illustrates the procedure for determining m_{MIRO}^* from the trace presented in Fig. 2.11. In panel (a) we plot the inverse values of the extrema positions $1/B_e$ against ε (open circles). We assumed a $\mp 1/4$ offset of the maxima (minima) with respect to the nodes of at integer values $\varepsilon = N$ and omitted the extrema around $N = 1$ where a more complex phase behaviour is expected [90]. Using the relation

$$\varepsilon = 2\pi f_{\text{MW}} m_{\text{MIRO}}^* / eB, \quad (2.9)$$

we perform a linear fit with zero intercept (solid line) which yields $m_{\text{MIRO}}^* = (0.335 \pm$

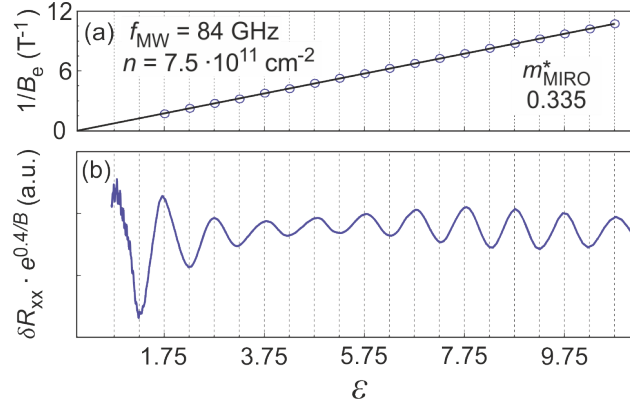


Figure 2.12: Demonstration of effective mass analysis from MIRO for the trace in Fig. 2.11. The electron density of the system was $n = 7.5 \times 10^{11} \text{ cm}^{-2}$. Panel (a): the inverse of the extrema positions are plotted against ε . The solid line represents a linear fit to Eq. 2.9. It yields $m_{\text{MIRO}}^* = 0.335m_0$. Panel (b): δR_{xx} as a function of ε . The photoresponse is multiplied by a factor $\exp(0.4/B)$ for better visibility of the low-field oscillations.

$0.006)m_0$. To illustrate the accuracy of this analysis we plot in Fig. 2.12(b) the resistive response against ε which was calculated by assuming the value $m_{\text{MIRO}}^* = 0.335m_0$. We multiplied δR_{xx} by $\exp(0.4/B)$ to improve the visibility of the low-field oscillations. Represented in this manner, all maxima (minima) fall precisely at $\varepsilon = N \mp 1/4$ for $N > 1$.

The low fit error in the presented method for extracting m_{MIRO}^* is due to the visibility of many extrema on the same trace. This is however not the case for all samples. In particular at low densities where MIRO becomes weak, only oscillations with $\varepsilon < 4$ are apparent. In this case we employed a different method for estimating m_{MIRO}^* with high accuracy. First we measured MIRO traces at different microwave frequencies. The position of each maximum (minimum) is extracted and plotted against f_{MW} . Assuming an offset of $1/4$, the f_{MW} -dependence of the N th maximum (minimum) is then fitted to the expression

$$f_{\text{MW}} = (N \mp 1/4)eB/2\pi m_{\text{MIRO}}^*. \quad (2.10)$$

From the slope of each fit we obtain m_{MIRO}^* . The average of all values yields the final result, with the standard deviation as the estimated error. The analysis of several selected extrema is presented in Fig. 2.13. The numbers marked on the graph correspond to $N \mp 1/4$. The resulting effective mass is $m_{\text{MIRO}}^* = (0.335 \pm 0.006)m_0$.

2.4.3 Competition with CR

Pronounced MIROs were detected in samples with $n \gtrsim 4.7 \times 10^{11} \text{ cm}^{-2}$, while in low-density systems ($n \lesssim 3.8 \times 10^{11} \text{ cm}^{-2}$) the photoresponse was dominated by the bolometric response due to cyclotron resonance. In the narrow density interval $3.8 \times 10^{11} \text{ cm}^{-2} \lesssim n \lesssim 4.7 \times 10^{11} \text{ cm}^{-2}$ features from both types of response could be seen. Such an example is shown in Fig. 2.14(a), where MIRO and CR coexist on the same differential magnetoresistance trace recorded on a sample with $n = 4.3 \times 10^{11}$

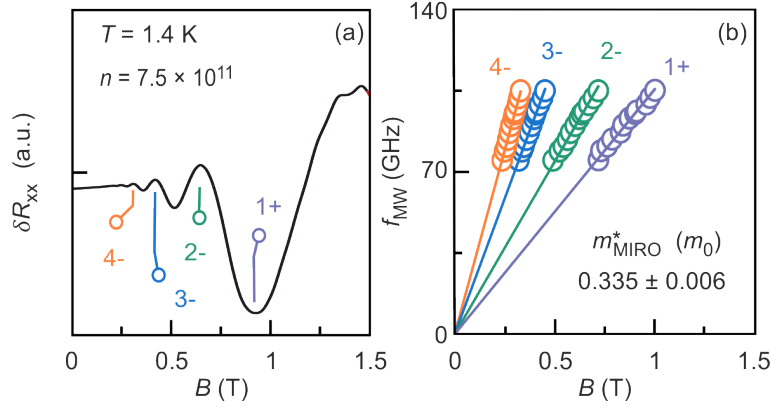


Figure 2.13: Effective mass extraction method based on microwave frequency dependence. (a) MIRO trace recorded at $f_{MW} = 96$ GHz. (b) The positions of the extrema identified in panel (a) are plotted against radiation frequency. The solid lines represent linear fits to Eq. 2.10. Each slope gives a value of m_{MIRO}^* which average to $(0.335 \pm 0.006)m_0$.

cm $^{-2}$. The plot shows the evolution of the photoresponse as we decrease the output power P_{out} of microwaves with $f_{MW} = 95$ GHz. The bath temperature was $T = 1.2$ K. At the highest output power, $P_{out} = 6.3$ mW, a strong CR response appears at the position corresponding to the bare mass m_{CR}^* (blue line). Additional features are present which, by reducing the microwave power sufficiently ($P_{out} = 0.78$ mW, red trace), can be identified as MIRO. The near disappearance of the CR signal at low power suggests its much faster decay with P_{out} than MIRO.

The independently measured magnetotransmission is presented in Fig. 2.14(b). Here a strong CR response is detected, the position of which matches that of the bolometric signal in δR_{xx} . This justifies the interpretation of the δR_{xx} peak as resonant absorption-induced heating of the 2DES.

Having isolated MIRO from the CR signal by reducing the radiation power, we can now estimate the effective mass using the frequency-dependent method described in the previous section. To improve the signal further, we have cooled the bath temperature to $T = 600$ mK and maintained an output power of $P_{out} = 0.78$ mW. The analysis yields $m_{MIRO}^* = (0.375 \pm 0.008)m_0$, which is 25% higher than the average bare cyclotron mass $m_{CR}^* \approx 0.3m_0$. This difference can be seen directly in Fig. 2.15 where we plot the differential magnetoresistance traces at high and low power against ϵ . The values of ϵ were calculated using the $m_{MIRO}^* = 0.375m_0$. In the low-power trace (red line) we see that the extrema of MIRO fall at the positions $\epsilon = N \pm 1/4$ ($N = 1, 2, 3$), as expected for a quarter phase. If the cyclotron mass were equal to the MIRO mass, the CR peak should have emerged at $\epsilon = 1$. Instead, it coincides to the first minimum of MIRO, corresponding to $\epsilon = 1.25$. We were therefore able to demonstrate through power-dependent photoresistance measurements that the MIRO mass is indeed renormalized with respect to the bare cyclotron mass.

MIRO could not be resolved in samples with carrier densities below 3.5×10^{11} cm $^{-2}$. Both microwave power and temperature dependent measurements were carried out on lower n systems in an effort to detect it. One experiment was performed at dilution refrigerator temperatures ($T \approx 20$ mK), accessing a regime where the

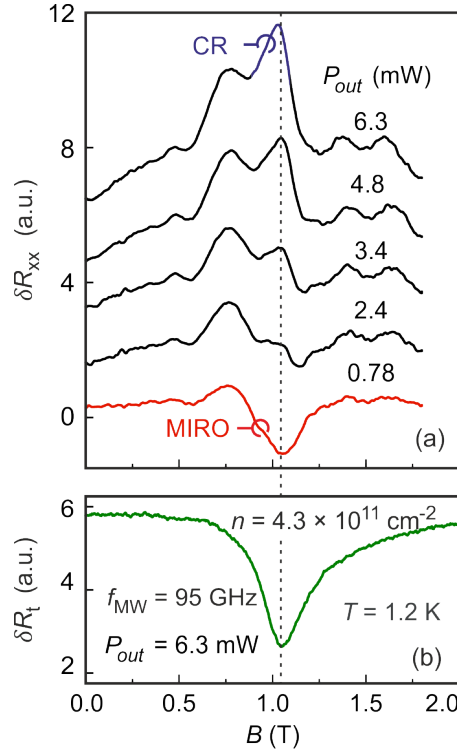


Figure 2.14: Photoresistance (a) and transmission (b) measured in a sample with $n = 4.3 \times 10^{11} \text{ cm}^{-2}$. Panel (a): Power dependent measurement of δR_{xx} . At high power, both CR and MIRO are visible in the same trace. At $P_{out} = 0.78 \text{ mW}$ only MIRO persist. Panel (b): The independently measured transmission features a strong CR signal. It coincides with the bolometric peak in δR_{xx} .

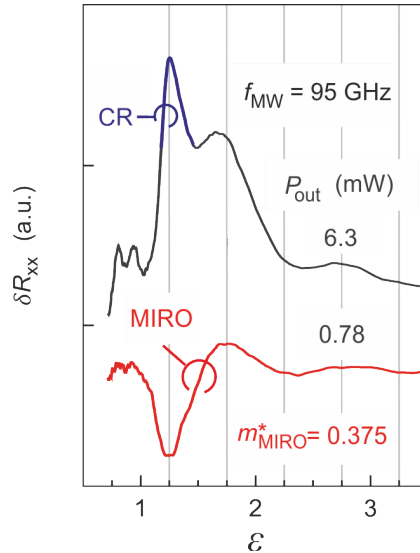


Figure 2.15: The photoresponse in Fig. 2.14 is replotted against ϵ , which is calculated using $m_{MIRO}^* = 0.375m_0$. The difference between the cyclotron and MIRO mass becomes evident.

resistance becomes independent of T . Neither CR nor MIRO features were found in δR_{xx} .

While the disappearance of CR as a photoresponse in high-density systems may be attributed to the weak temperature dependence of the resistance at low T , the vanishing of MIRO as the electron density is reduced below $n \approx 3.5 \times 10^{11} \text{ cm}^{-2}$ is more enigmatic. The low- T measurements show that the disappearance cannot be attributed to the overpowering CR signal. The oscillations have diminished amplitude at intermediate values of n , compared to the ones measured in systems with $n > 6 \times 10^{11} \text{ cm}^{-2}$. This gradual damping may be connected to the decreasing transport scattering rate $1/\tau$ as n is reduced. A low $1/\tau$ would in turn lead to less effective scattering-assisted excitations to higher LLs, which is a prerequisite for the displacement mechanism of MIRO. Indeed, in high-density ZnO 2DESs, τ is limited by impurities and interface roughness. The latter is more pronounced at high Mg content [149, 150] and thus at higher n . A study of Hall field-induced resistance oscillations (HIRO) in a high-density ZnO 2DES reconfirms that large-angle scattering off impurities close to the 2DES and/or interface roughness are the main source of scattering [151]. This assumption is supported by theory, which predicts a heavy reliance of the displacement mechanism on short-range scattering [96]. However, the presented explanation is not sufficient to understand why other mechanisms, such as the inelastic mechanism, would not play a role. All in all, it is highly probable that the resistance contribution of the displacement mechanism is diminished at low n . The relative contribution of different MIRO mechanisms may constitute the focus of future work.

2.4.4 Power dependence of the microwave response

To better understand the power-dependent photoresponse in Fig. 2.14(a) we have investigated the MIRO and CR amplitudes as a function of P_{out} . The measurements were carried out on two separate samples, one with high density which displayed MIRO ($n = 7.5 \times 10^{11} \text{ cm}^{-2}$) and the other with low density ($n = 2.3 \times 10^{11} \text{ cm}^{-2}$) in which δR_{xx} showed a strong CR response. The result is illustrated in Fig. 2.16 for $f_{\text{MW}} = 95 \text{ GHz}$ and $T = 1.2 \text{ K}$. The amplitude of MIRO is found to increase linearly with power for $P_{\text{out}} < 1.5 \text{ mW}$. At higher values, the P_{out} -dependence is sub-linear and can be approximated as square-root. Above radiation powers of 4 mW , the oscillations saturate in amplitude and eventually start to decay for $P_{\text{out}} \gtrsim 5 \text{ mW}$. We observe no shift from the conventional $1/4$ phase of the minima and maxima associated with the power dependence. Moreover no additional oscillations are observed which may indicate multi-photon processes. Therefore the saturation and decay of MIRO cannot be attributed to intrinsic non-linear effects [152, 153]. Instead, we associate the power dependence at high P_{out} to heating. The CR amplitude, on the other hand, displays a sub-linear growth over the entire range of power under study.

2.4.5 Discussion: effective mass

Using the methods described in section 2.4.2., we have extracted the effective mass in a set of ten samples that displayed MIRO. Based on the sample availability

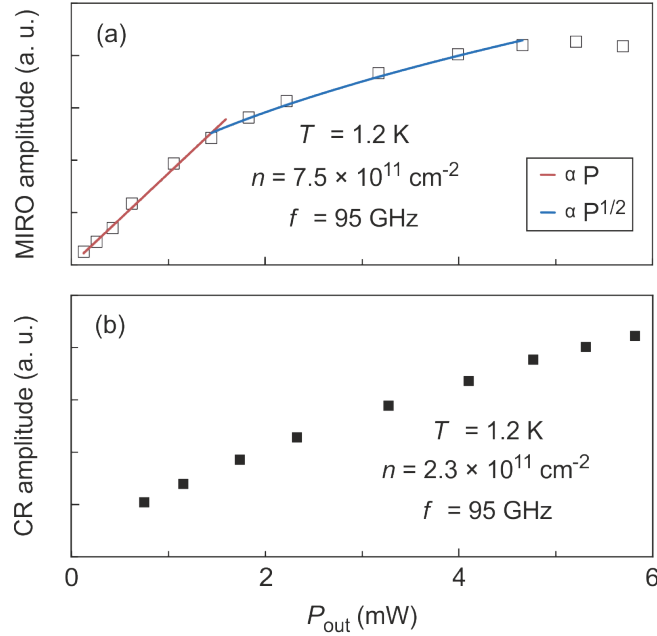


Figure 2.16: Microwave power dependence of (a) MIRO and (b) CR amplitude. Both experiments were performed under the conditions f_{MW} and $T = 1.2$ K.

and/or the presence of MIRO, we have studied systems with electron densities in the range $3.5 < n < 20 \times 10^{11} \text{ cm}^{-2}$, which spans the interaction parameter values $2.6 \leq r_s \leq 6.3$. The results are shown in Fig. 2.17 (squares). For comparison we have also plotted the bare cyclotron mass obtained from both photoresistance (triangles) and transmission measurements (diamonds), as well as the interaction renormalized mass extracted from temperature dependent SdHO [81, 121]. At high n the MIRO mass falls below the average cyclotron mass of $m_{\text{CR}}^* = 0.3m_0$. As the electron density is lowered, m_{MIRO}^* appears to increase monotonically and a 33% enhancement with respect to m_{CR}^* is observed at the lowest density where MIRO could still be detected. Unfortunately, a relatively large interval ($11 \lesssim n \lesssim 20 \times 10^{11} \text{ cm}^{-2}$) is left unexplored, and therefore we cannot be certain that a non-monotonic dependence does not occur.

Both the effective mass reduction at high density and the sharp enhancement as n decreases are also present in SdHO measurements which are known to probe the interactions-renormalized quasiparticle mass [15, 154]. Although there is a discrepancy between the m_{MIRO}^* and m_{SdHO}^* , the two quantities display approximately the same trend. Theoretical studies of excitations and energy bands of interacting 2DESs [14, 17, 155] qualitatively reproduce this behaviour. However neither the quantum Monte Carlo method [14, 155] nor the many-body local fields approach [17] describe the mass renormalization in ZnO quantitatively. In particular, most theoretical calculations either predict a much weaker or a stronger enhancement as the interaction parameter increases. Limitations may come from the assumption of a perfectly 2D system as well as the absence of a finite magnetic field in the models.

The findings presented in Fig. 2.17 reconfirm the premise that the MIRO mass is sensitive to electron-electron correlations. As revealed in Section 2.3, the cyclotron resonance probes the non-interacting electron mass due to the nature of CR excita-

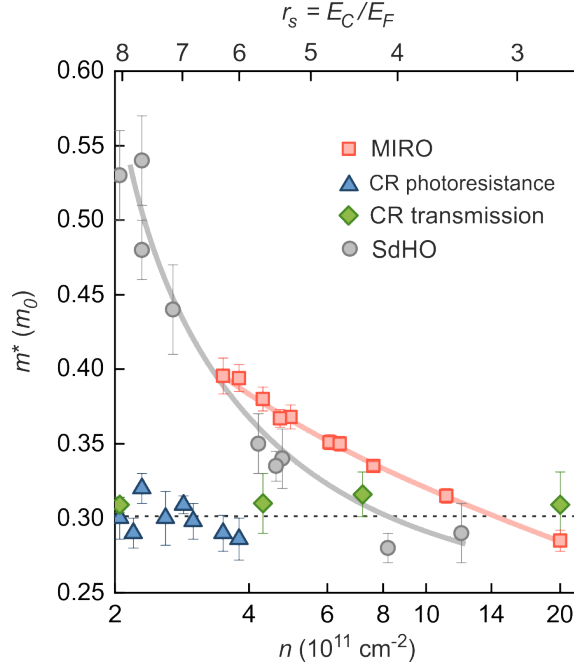


Figure 2.17: Summary of effective mass values obtained from MIRO (squares), CR in photoresistance (triangles) and transmission (diamonds), as well as SdHO (circles). The dashed line represents the average cyclotron mass, $m_{\text{CR}}^* = 0.3m_0$. The solid curves are guides for the eye.

tions: upon the absorption of a photon, an electron-hole pair with wave vector $\vec{k} \rightarrow 0$ forms; in view of momentum conservation and Kohn's theorem [89], the energy at which resonant absorption occurs remains unaffected by interactions. By contrast, MIRO involves scattering-assisted excitations which, in a magnetic field, can have large spatial electron-hole separation l . This separation translates to a large k wave number, by virtue of the relation:

$$k = \frac{l}{l_B}. \quad (2.11)$$

Therefore the MIRO mass is expected to be renormalized by correlations in a similar way as the SdHO mass.

MIRO poses a big advantage over the conventional SdHO analysis for extracting the interacting-electrons effective mass, since it does not require time-consuming temperature dependent measurements. Moreover, if sufficient oscillations are visible, the effective mass can be extracted with much higher precision, as is obvious from Fig. 2.17.

2.5 Electron spin resonance

The coupling of an external static magnetic field with the spin of a conduction electron results in the lifting of the spin degeneracy. The splitting between the spin subbands is given by the Zeeman energy, $E_Z = g\mu_B B$. Electron spin resonance (ESR) experiments can probe the size of this splitting if an external radiation field

of frequency commensurate to the Larmor frequency $g\mu_B B/\hbar$ is applied.

In various 2D materials, ESR has been extensively studied to obtain the g -factor value and anisotropy, as well as the spin relaxation times [156, 157, 158, 159, 160, 161, 162, 163]. The former aids in assessing the strength of spin-orbit coupling (SOC), while the latter offers an indication of the abundance of magnetic impurities and nuclear spins. The utility of ESR is not restricted to these quantities however. Careful analysis of the Overhauser shift of the ESR line can yield information on the hyperfine coupling [164, 165]. Recently, evidence for an intrinsic spin-orbit bulk gap has been found in monolayer graphene by investigating the paramagnetic resonance spectrum. Studies of ESR as a function of filling factor have yielded interesting results in an AlAs 2DES: two spectral lines were observed in the vicinity of even ν [166], which were associated with excitations occurring within two LLs of different index.

According to Larmor's theorem [167], the position of ESR is insensitive to electron-electron interactions in the long wavelength limit, provided that the system is spin-rotational invariant. Therefore the g -factor obtained from the paramagnetic resonance condition reflects the single-particle band g -factor, rather than the renormalized value expected in a Fermi liquid system. To circumvent this theorem, surface acoustic waves have been generated to investigate ESR at large wave-vectors in the quantum Hall regime [168]. Strong enhancement of g^* was observed around odd filling factors, where exchange energy contributions to the spin wave energy is expected to peak [169]. Although breaking of Larmor's theorem is also expected in systems with strong spin-orbit coupling [115], so far no strong evidence of this effect has been reported.

In ZnO-based 2DESs ESR measurements have revealed extremely sharp resonance lines ($\Delta B \approx 0.5$ mT) [134], which correspond to a spin-spin relaxation time T_2 as large as 27 ns, comparable to the values reported in Si/SiGe heterostructures [170]. The long coherence time owes to the low natural abundance of Zn or O isotopes with unpaired nuclear spins. The only such species is the ^{67}Zn isotope which has a nuclear spin of 5/2. A small deviation from the linear resonance relation was attributed to the Rashba SOC, the strength of which, characterized by the Rashba parameter, is 7×10^{-14} eV m. In a study performed by Shchepetilnikov et al. [166] on a ZnO 2DES, the filling factor dependence of the ESR amplitude revealed an interesting alternation between peaks around odd ν and dips in the vicinity of even ν . The mere existence of a finite ESR signal at even filling factors is puzzling, as spin-flip excitations within a fully occupied LL are not possible. The interpretation of the ESR line shape is also worthy of discussion. Here we revisit these findings and attempt to explain the phenomenon.

2.5.1 Detection

The conventional way of detecting ESR is by using a dedicated spectrometer [171]. Microresonators may be patterned on the samples to improve the signal-to-noise ratio [172]. Nonetheless, direct measurement of ESR signals in 2D systems is challenging due to the reduced number of paramagnetic spins. Electrical detection is preferred in this case, as the signal amplitude does not scale with the size of the system [159]. The underlying mechanism relies on the change in the resistance upon

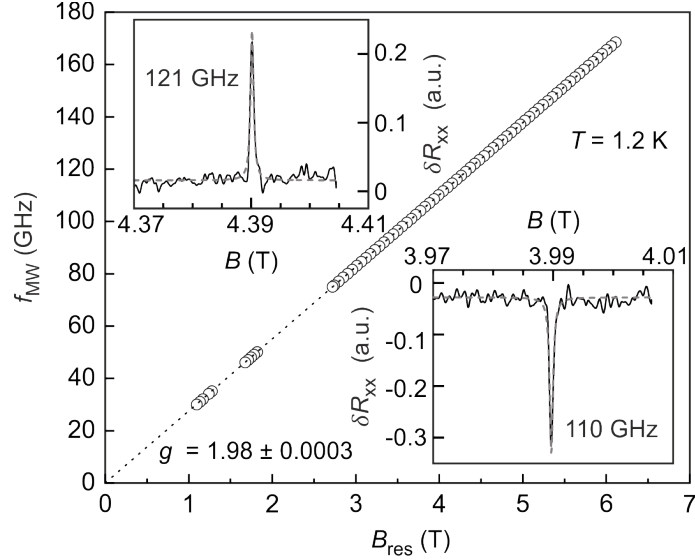


Figure 2.18: Paramagnetic resonance in a sample with $n = 5.3 \times 10^{11} \text{ cm}^{-2}$. Main plot: a straight line describes the microwave frequency dependence of the resonance field. Its slope yields the g -factor value of 1.98. Insets: ESR signals at $f_{\text{MW}} = 121 \text{ GHz}$ and 110 GHz , as marked. The solid lines represent Lorentzian fits.

resonant absorption of microwaves, when the radiation frequency matches the Larmor frequency. The sensitivity to microwave absorption is generally attributed to an increase in the 2DES temperature, but other factors such as a change in spin polarization may come into play.

In this section we present electrically detected ESR measurements around integer filling factors. While in most cases an ESR response could be detected directly in the sample resistance, R_{xx} , concomitant measurements of the differential resistance δR_{xx} have been performed, as illustrated in Fig. 2.1.

2.5.2 ESR spectrum

ESR measurements were performed on a sample with $n = 5.3 \times 10^{11} \text{ cm}^{-2}$ in a perpendicular magnetic field. A single ESR line was observed. The insets of Fig. 2.18 show two representative differential magnetoresistance traces in the vicinity of the paramagnetic resonance at $f_{\text{MW}} = 121 \text{ GHz}$ and $f_{\text{MW}} = 110 \text{ GHz}$. A Lorentzian function was used to fit the curves (dashed lines) and obtain the resonance B -field. In some cases the ESR line was asymmetric, yielding a larger standard deviation when approximated with a Lorentzian function. Nevertheless, the error did not exceed the full width at half maximum of the ESR line. The main plot displays the positions of the ESR as a function of radiation frequency. A linear dependence with zero intercept is found. Using the resonance condition $hf_{\text{MW}} = g\mu_{\text{B}}B$, we obtain the g -factor value $g = 1.98 \pm 0.0003$, where the error represents the standard deviation from the linear fit. This value is fairly close to the reported band value in bulk $\text{Mg}_x\text{Zn}_{1-x}\text{O}$, $g_{\text{b}} = 1.96$ [173] (we assumed a Mg concentration of $x = 0.05$). A comparison with the interaction-renormalized value obtained from transport measurement, $g^* \approx 4$, suggests that ESR probes the single-particle Zeeman splitting,

aligning with Larmor's theory [167].

A small rise ($\sim 1\%$) of the g -factor was observed with increasing microwave frequency when the value of g was directly calculated from the resonance equation. However, this estimate should be taken with caution. Precise measurements require careful monitoring of the magnetic field which in practice can be done with the use of a Hall sensor. In the absence of such a device, we refrain from interpreting small changes in the value of the g -factor, which may occur due to field dependent trapped flux in the superconducting coil.

2.5.3 Filling factor dependence

Monitoring the evolution of the ESR line shape with B -field reveals that the signal alternates between a peak and a dip depending on the parity of the filling factor. A summary of the line shape character as a function of ν and T is illustrated in Fig. 2.19. The main plot shows the longitudinal magnetoresistance curves at three different temperatures. In the panels above it representative ESR lines corresponding to $\nu = 4, 5, \dots, 8$ are shown. At $T = 1.2$ K ESR can be detected around all filling factors under study, with the line shape alternating systematically between a dip around even ν and a peak at odd ν . As the temperature is reduced, the width and shape of the resonance at $\nu = 5$ and $\nu = 7$ remains approximately the same. At $\nu = 6$ and $\nu = 8$, however, the ESR lines broaden and change from a simple dip to a derivative-like signal. Finally, at $\nu = 4$ no ESR could be detected at $T \leq 0.6$ K. A more complete evolution with microwave frequency can be found in Fig. 2.20 where both the δR_{xx} and R_{xx} are shown in the vicinity of four selected filling factors. The bath temperature was $T = 1.2$ K.

To understand the origin and shape of the ESR signal, it is helpful to consider the effect of resonant absorption and finite temperature on the LL occupation. The longitudinal resistance R_{xx} displays thermally activated behaviour around integer filling, which can be described by the relation [174]:

$$R_{xx} \approx R_0 \exp\{-(E_{N,\downarrow} - \mu_{\downarrow})/k_B T_e\} + R_1 \exp\{-(\mu_{\uparrow} - E_{N,\uparrow})/k_B T_e\}, \quad (2.12)$$

where $E_{N,\downarrow}$ and $E_{N,\uparrow}$ denote the N th spin-down and spin-up LLs, respectively, and μ_{\downarrow} (μ_{\uparrow}) is the chemical potential of spin-down (spin-up) electrons. From this equation it becomes clear that at resonance, the electron temperature T_e may increase due to radiation absorption, which leads to a rise of the longitudinal resistance. Electron heating is therefore often used to explain the ESR peaks around integer filling.

A second mechanism for a resistance change at resonance stems from the non-equilibrium chemical potential corresponding to spin-up and spin-down populations. We exemplify this schematically in Fig. 2.21 for $\nu = 4$ and $\nu = 5$. Off resonance, a few thermally activated electrons may populate the LL right above the chemical potential. This is definitely the case for $\nu = 4$ and $\nu = 5$ at $T = 1.2$ K, where the longitudinal resistance is finite (see Fig. 2.19). At resonance and $\nu = 5$, the chemical potential of the spin-up (spin-down) electrons moves closer to the $E_{2,\uparrow}$ ($E_{2,\downarrow}$) LL. By virtue of Eq. 2.12, this leads to an increase in R_{xx} . It is therefore possible that both electron heating and the upward (downward) shift of μ_{\downarrow} (μ_{\uparrow}) contribute to the ESR signal at odd filling factors. In the case $\nu = 4$, however, the opposite happens:

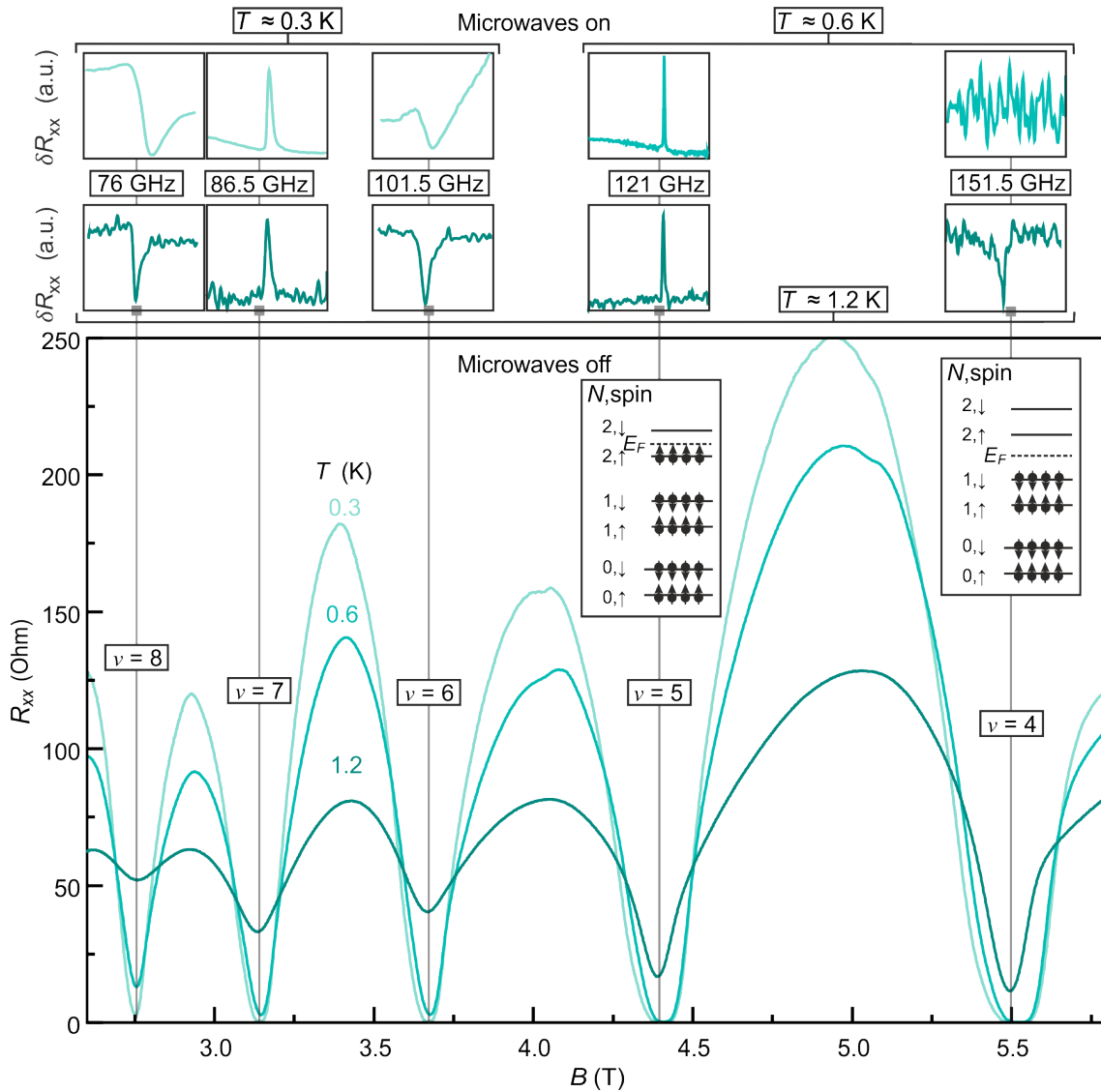


Figure 2.19: Study of ESR line shape as a function of filling factor and temperature. The main plot shows traces of the longitudinal magnetoresistance in the absence of illumination at a set of three temperatures, as indicated. The occupation of LLs at $\nu = 5$ and $\nu = 4$ is illustrated for $T = 0$. Top panels: ESR signals detected in δR_{xx} in the vicinity of integer ν . The x -axis is the magnetic field in a range of ≈ 50 mT. The first row of graphs were measured at $T = 0.3$ K or $T = 0.6$ K, as marked. The second row corresponds to $T = 1.2$ K.

resonant absorption leads to a shift of μ_\downarrow (μ_\uparrow) further away from the closest LL, namely $E_{1,\downarrow}$ ($E_{2,\uparrow}$), resulting in a decrease in R_{xx} . Note that a finite ESR signal at even filling factors should not be present at all in the absence of thermally activated carriers, as spin-flip excitations can only occur within the same LL. The fact that around $\nu = 4$ ESR diminishes and eventually disappears as T is lowered is most likely a consequence of the $(2, \uparrow)$ LL becoming depleted of electrons.

The above explanation is only valid if the longitudinal spin relaxation time T_1 is much longer than the electron-lattice relaxation time [174] such that a non-equilibrium shift of the spin-up and spin-down electrons can occur. This implies that photoexcited electrons will more likely relax to a same-spin LL rather than to the same-index LL of opposite spin. This is a reasonable assumption in our samples, as T_1 can be as long as 100 ms in bulk ZnO [175], while the transport relaxation time is of the order of 10 ps.

The above results corroborate fairly well with the findings presented in Ref. [176] and later republished in Ref. [177]. In this study the amplitude of ESR is monitored as the system is driven through a ferromagnetic-to-paramagnetic transition at filling factor $\nu = 2$. This is achieved in a sample of density $n = 1.8 \times 10^{11} \text{ cm}^{-2}$, where the condition $E_Z/E_c = 1$ is met due to the interaction-renormalized g -factor and effective mass. The LL coincidence is marked by a resistance peak in the $\nu = 2$ minimum (see Fig. 2.22). On the low field side of this peak ($\nu \gtrsim 2$), strong ESR could be detected, while on the high B side ($\nu \lesssim 2$) the resonance disappears. We associated this abrupt change in the ESR amplitude with a spontaneous spin depolarization due to the rearrangement of the LLs. The presence of strong ESR peaks on the ferromagnetic side of the transition agrees well with both the electron heating and chemical potential shift model presented above. Due to the inverted order of $(0, \downarrow)$ and $(1, \uparrow)$ LLs, the non-equilibrium shift of μ_\downarrow and μ_\uparrow lead to a positive change in resistance. On the paramagnetic side, however, one would expect a finite, though perhaps weaker, ESR signal of opposite sign. Instead, no resonance could be detected. It is possible that, given the relatively low bath temperature of the experiment, $T = 500\text{mK}$, only few thermally activated electrons populate the $(1, \uparrow)$ LL, leading to a undetectably small resistance change.

An alternative roadmap has been used to justify the existence of ESR at even filling factors in ZnO in an unpublished manuscript by Shchepetilnikov et al. [178]. Here, the authors argue that thermal excitations are insufficient to account for the comparably large amplitude at even ν and odd ν . Instead the effect of strong electron-electron interactions is brought into view. At even filling factors, the lowest energy excitation involves a spin flip and a change $\Delta N = 1$ in the LL index. Such an excitation is often referred to as a cyclotron spin flip mode (CSFM). Its energy at zero wave-number can be written as [167]:

$$E_{\text{CSFM}} = \hbar\omega_c + g\mu_B B \Delta S_z + \Delta, \quad (2.13)$$

where $\Delta S_z = 1, 0 - 1$ is the change in the projection of the electron spin; Δ stands for an interaction-mediated shift and is approximated as $\Delta \approx -\hbar\omega_c \kappa = -m^* e^4 / \epsilon \hbar^2$ [179]. Here κ denotes the interaction parameter in a magnetic field and is defined as the ratio between the Coulomb energy $E_C(B) \approx e^2 / 4\pi\epsilon l_B$ and the cyclotron energy. If κ is sufficiently large such that Δ is comparable or exceeds $\hbar\omega_c$, then

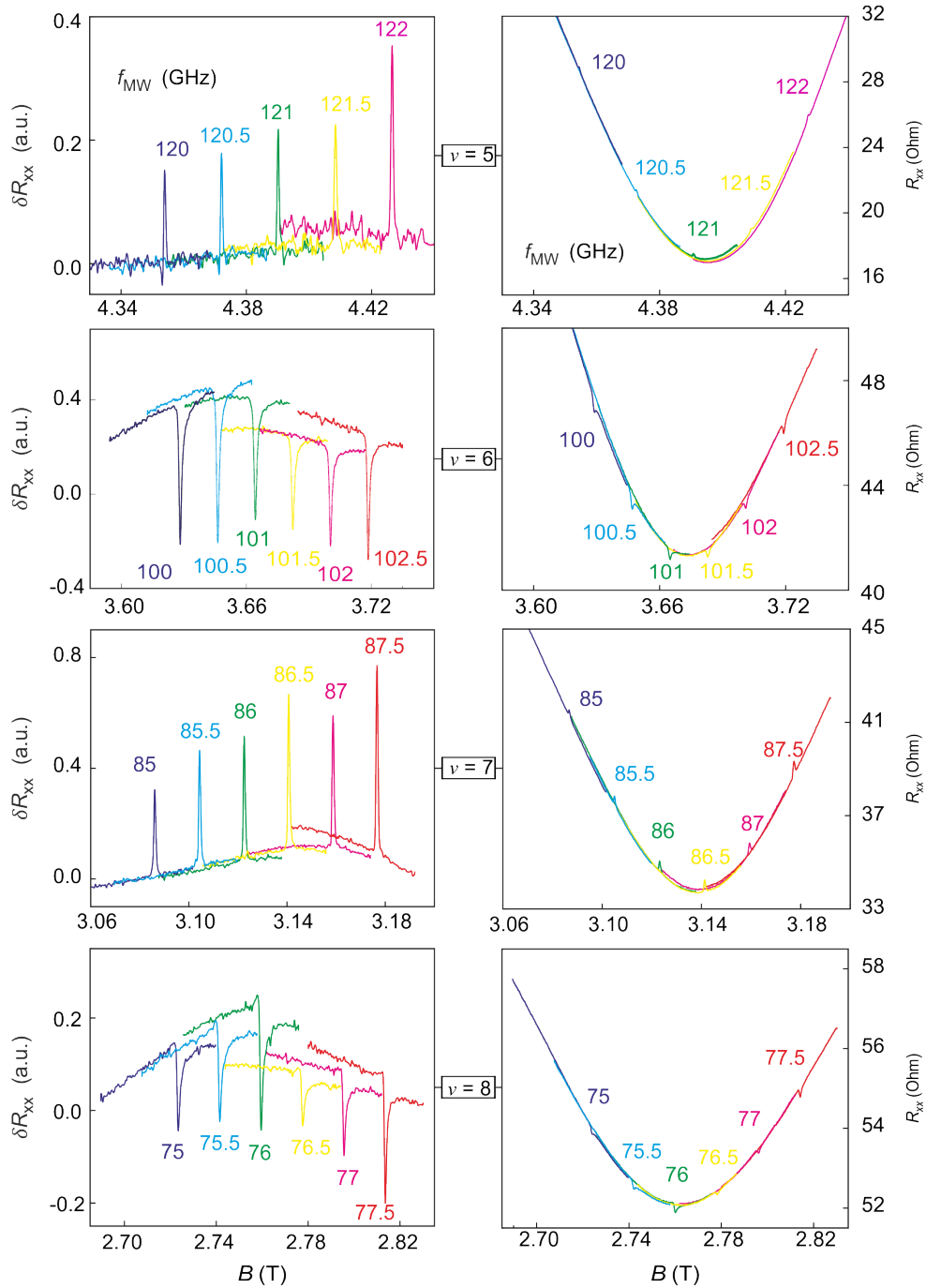


Figure 2.20: Evolution with frequency of ESR line shape around four selected filling factors. The left and right panels correspond to the response in δR_{xx} and R_{xx} , respectively. The bath temperature was $T = 1.2$ K.

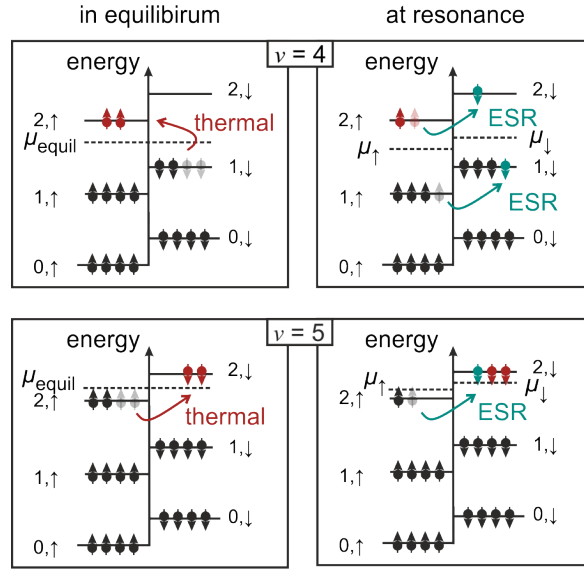


Figure 2.21: Sketch of the LL occupation at $\nu = 4$ and $\nu = 5$, in equilibrium and at resonance. Thermally excited carriers (red symbols) aid spin-flip excitations around $\nu = 4$.

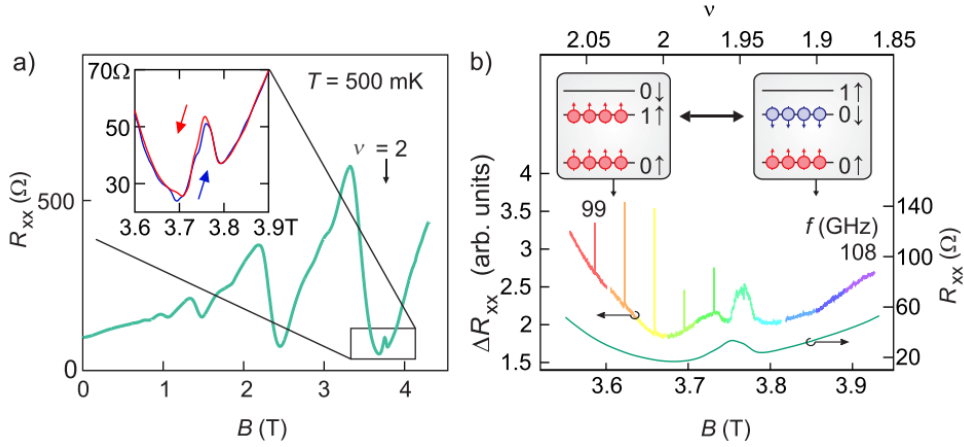


Figure 2.22: ESR study of the transition from a fully spin polarized to an unpolarized state around $\nu = 2$. The sample electron density was $1.8 \times 10^{11} \text{ cm}^{-2}$ and $T = 500 \text{ mK}$. (a) In the absence of illumination, the longitudinal magnetoresistance features a strong resistance peak in the $\nu = 2$ minimum, which is associated to scattering off domain wall boundaries. Inset: hysteretic behaviour is observed upon sweeping the magnetic field in opposite directions. (b) Longitudinal resistance and photoresistance in the vicinity of the ferromagnetic-to-paramagnetic transition. At $\nu \gtrsim 2$, strong ESR signals were found, reflecting the large spin polarization illustrated in the box on the left. For magnetic fields above the coincidence resistance peak, the ESR signal vanishes. This is consistent with the LL arrangement in the right box, where the $N = 0$ LL is fully occupied, thus forbidding any spin-flip excitations. From [176], adapted for [177].

a large number of CSFM excitations would occur, populating the adjacent higher-energy LL. The authors suspect that this is the cause of finite spin polarization at even filling factors which allows the observation of ESR. Interestingly, Δ turns out to greatly exceed $\hbar\omega_c$: for $B = 5.5$, $\kappa \approx 7$, leading to values of Δ an order of magnitude larger than the cyclotron resonance. This calls into question the validity of the expression for Δ , which was obtained under the assumption that κ is small [179]. According to this interpretation, a finite spin polarization at even filling should still exist even at zero temperature. We would therefore expect an equally robust ESR signal when T is reduced, as it is observed for example at $\nu = 5$. We will discuss this matter in more detail in the next section. Although we cannot refute that level mixing due to strong interactions do play a role, we find it more likely that thermal excitations are dominant mechanism for spin polarization at even ν .

2.5.4 Temperature dependence

The interpretation of the ESR line shape dependence on filling factor based on the effect of a non-equilibrium change of μ_\downarrow and μ_\uparrow cannot give a plausible explanation why the ESR signal is comparable in strength at even and odd filling factors. Moreover, it does not include the effect of heating of the 2DES, which should lead to an increase in R_{xx} at integer filling. While the disappearance of ESR at $\nu = 4$ as T decreases does agree well with the reduced number of thermally activated carriers in the $(2, \downarrow)$ LL, it can also be the result of approaching zero longitudinal resistance. In that case a further decrease in R_{xx} would no longer be possible. The effect of photo-induced heating may also not be visible if the increase in electron temperature is not sufficiently large. In both cases the resistance becomes insensitive to resonant absorption. Driven by this dilemma, in this section we explore the temperature dependence of the ESR line shape at $\nu = 6$ and $\nu = 7$.

Let us first investigate the evolution of the ESR line shape around an odd filling factor. Figure 2.23(a) presents the differential magnetoresistance for the $f_{\text{MW}} = 86.5$ GHz paramagnetic resonance as the sample is cooled down from 1.2 K to 0.35 K. The output power was fixed at $P_{\text{out}} = 0.35$ mW. The position of ESR at this radiation frequency corresponds to $\nu \approx 7$. The line shape can be approximated to a Lorentzian at all temperatures. In the inset we plot the extracted amplitude as a function of T . It increases abruptly as T is reduced to ≈ 0.6 K, but it appears that saturation begins at even lower temperature. This could be related to the resistance sensitivity on the electron temperature. Far from zero, R_{xx} decreases rapidly with T_e . As $T_e = 0$ is approached, the resistance bottoms out. Within the model of the chemical potential shift, an increase in photosensitivity at low T may be related to a larger population difference between spin-up and spin-down electrons, which in turn increases the probability of photoexcited carriers.

In Fig. 2.23(b) and (c) the width and position of the ESR line are plotted against temperature. We notice that the width varies little when the sample is cooled down. A small but systematic shift of the resonance peak is observed, which corresponds to a decrease of less than 0.01% in the g -factor value. Given the accuracy of the experiment, this shift can be neglected.

Shifting our attention to the ESR line around $\nu = 6$, we find a considerably different behaviour. We display the temperature dependence of the spin resonance

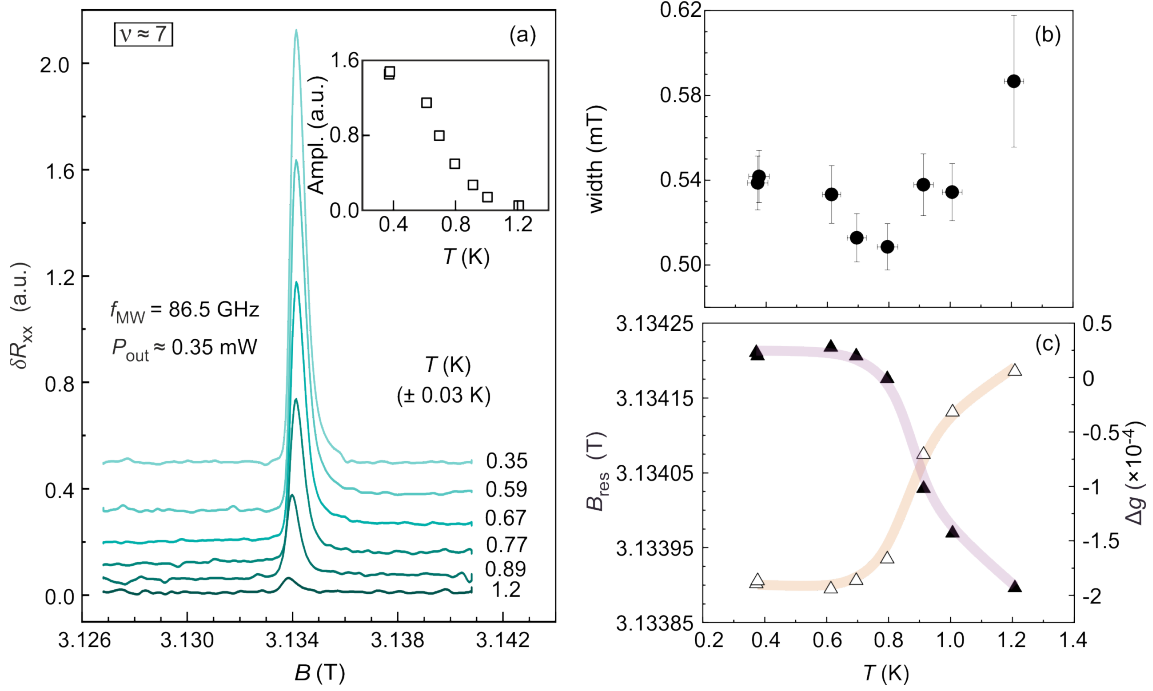


Figure 2.23: Analysis of the ESR line dependence with temperature in the vicinity of $\nu = 7$. (a) Evolution of ESR for $f_{\text{MW}} = 86.5$ GHz as T is reduced from 1.2 K to 0.35 K. Inset: T -dependence of ESR amplitude. (b) Width, (c) position and g -factor of the resonance traces in panel (a). Solid lines in (c) are guides for the eye.

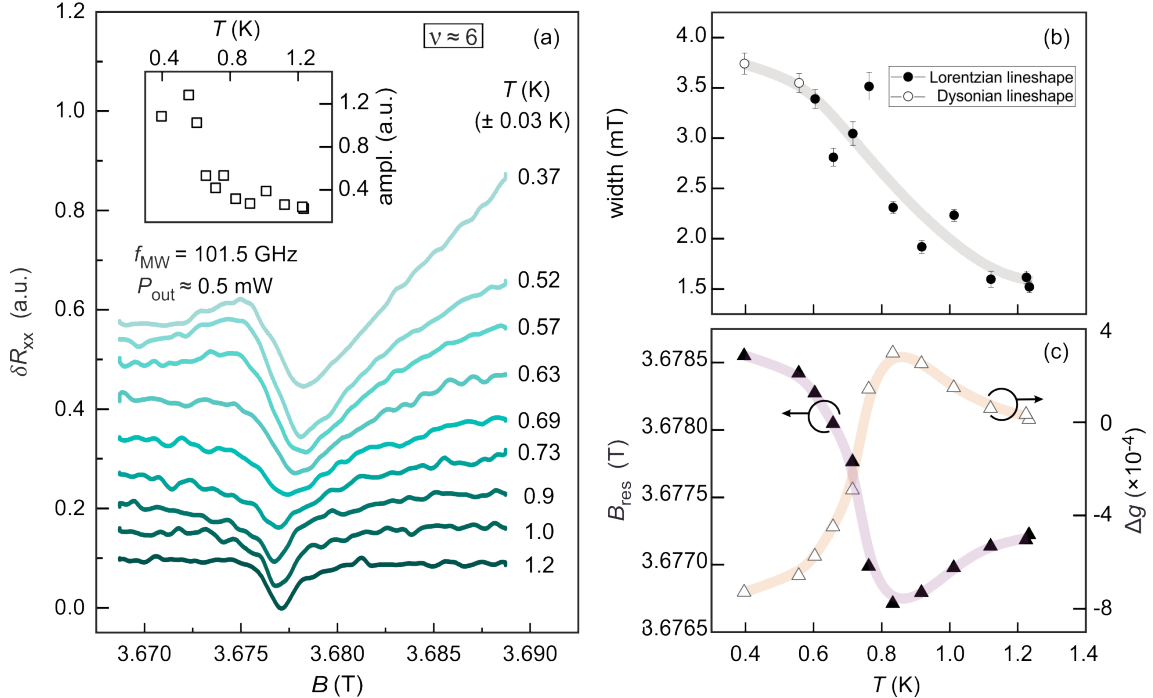


Figure 2.24: Analysis of the ESR line dependence with temperature in the vicinity of $\nu = 6$. (a) Evolution of ESR for $f_{\text{MW}} = 101.5$ GHz as T is reduced from 1.2 K to 0.37 K. Inset: T -dependence of ESR amplitude. (b) Width, (c) position and g -factor of the resonance traces in panel (a). Solid lines in (b) and (c) are guides for the eye.

at $f_{\text{MW}} = 101.5$ GHz and $P_{\text{out}} = 0.5$ mK in Fig. 2.24(a). Firstly, the line shape changes gradually from a Lorentzian at $T = 1.2$ K to a derivative-like signal at $T \lesssim 0.55$ mK. We speculate that at lower T , the effect of heating becomes more prominent, leading to an additional contribution to the photo-induced change in R_{xx} .

To approximate the amplitude at low T , we attempted to fit the ESR line with a Dysonian function [180] but the result was not satisfactory. Instead, we estimate it as the peak-to-peak differential resistance change, assuming a background value equal to δR_{xx} at the low B -side of the trace. The inset of Fig. 2.24(a) shows the result. The amplitude rises three fold in the available temperature range. This is in contrast to the behaviour of ESR at $\nu = 4$ where it vanishes as T is reduced. This is rather puzzling and does not agree with the model of finite polarization due to thermally activated carriers. The increase in amplitude is also difficult to be reconciled with the interaction-mediated excitations, as temperature does not enter the expression of Δ .

The width and position, alongside the corresponding g -factor of the ESR signal at $\nu = 6$ are plotted in Fig. 2.24(b) and (c), respectively. The g -factor displays a non-monotonic dependence on T , with an overall reduction of $\approx 0.04\%$. As for the width, the resonance line becomes significantly broader at low T , in contrast to the $\nu = 7$ case. In Si-based 2DESs, the increase of the line with decreasing T has been associated with motional narrowing [157]. However to our knowledge, no theoretical model accounting for filling factor dependence of the ESR line width has been reported.

Chapter 3

The 2DES in the ultra-low density regime

When the average Coulomb interaction greatly exceeds the kinetic energy, and other factors such as thermal fluctuations and disorder are reduced to a minimum, the 2DES is expected to transition to a charge- or spin-ordered state. Here we explore the possibility of such transitions in a very dilute ZnO 2DES through DC transport. In addition we perform EDSR measurements, which reveal a double spectral line.

3.1 Methods

The results presented in this chapter have been measured on two MBE-grown MgZnO/ZnO samples originating from the same wafer. We refer to them as S6481 and S6482. While their growth process was the same, one of the samples (S6482) presented higher mobility. Moreover in S6482 the SdHO were visible down to lower magnetic field values, which, by virtue of Eq. 1.33, corresponds to a longer quantum lifetime. For this reason, all transport measurements shown in this chapter were taken on S6482.

The chips were cleaved into rectangles with an approximate area of $A = 4 \times 2 \text{ mm}^2$. Ti/Au contacts were thermally evaporated on the MgZnO surface. Since the 2DES populates the triangular quantum well that forms self-consistently at the heterostructure interface, it is buried below the MgZnO cap layer. To improve the contacts to the two-dimensional conducting layer, indium leads were soldered on top and at the edge of the chips. Figure 3.1 shows top-view SEM images of sample S6481. In the image on the right one can see a smaller portion of the surface with circular defects with a diameter of about $2 \mu\text{m}$. Generally these pits have a larger size and density in heterostructures grown under high ozone flux [77]. The samples were glued on a gold-plated chip carrier using conducting Sigma-Aldrich silver paste. A metallic layer evaporated on the back side of the chips constitutes the backgate. Gold wires are used to connect the leads and the backgate to the chip carrier pins.

Observation of exotic phenomena such as the metal-insulator transition (MIT), Wigner crystallization and spin-ordering would not be possible unless thermal energy is reduced well below the characteristic interaction energy. For instance, according

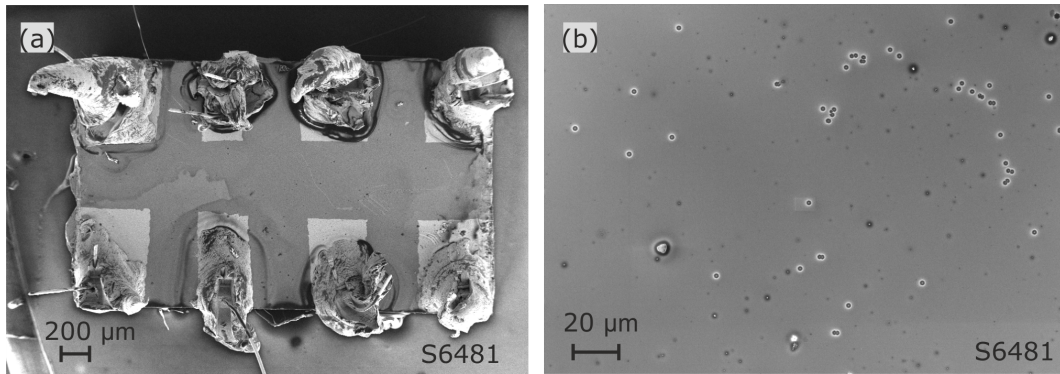


Figure 3.1: SEM images of the MgZnO/ZnO sample S6481. (a) Top view of the chip with Ti/Au and indium contacts. (b) Close-up of the MgZnO surface.

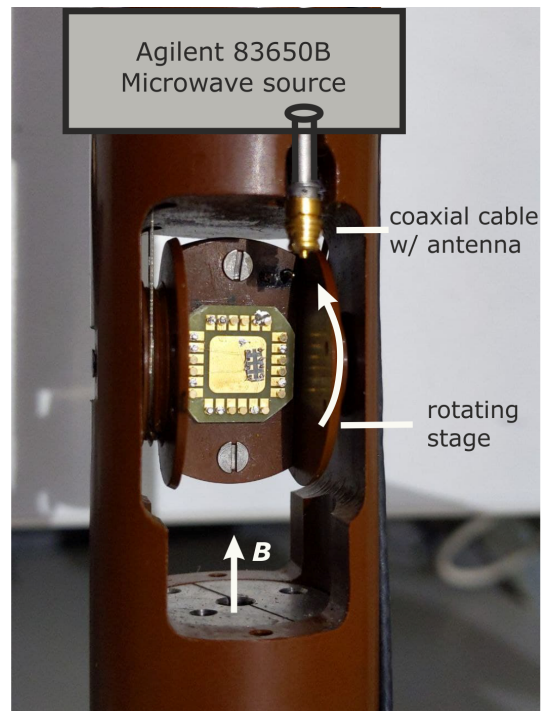


Figure 3.2: Segment of the dilution refrigerator sample probe. The ZnO chip is mounted on a stage capable of 90° rotation. In the present configuration the magnetic field would point in the plane of the 2DES. A coaxial cable terminating in an antenna guides monochromatic radiation from an Agilent 83650B microwave source ($f \leq 50$ GHz).

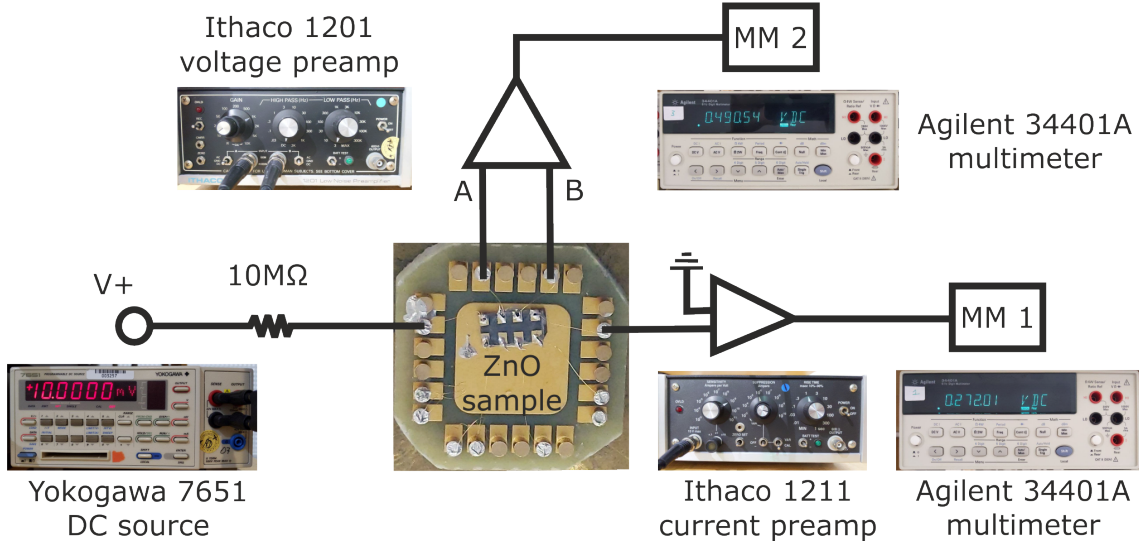


Figure 3.3: Four terminal DC measurement setup. The sample is biased using a Yokogawa voltage source. The current and the potential drop are amplified using Ithaco preamplifiers. The two signals are then separately output to Agilent digital multimeters.

to Ref. [20] the Wigner crystal melting point can be as low as 30 mK. To access such low temperatures we make use of a dilution refrigerator. Most measurements shown in this chapter were taken in an Oxford Instruments cryostat with top-loading capability. The temperature at the mixing chamber (MC) was monitored with the help of a calibrated ruthenium oxide resistor. Its resistance was recorded continuously during measurements. Due to the sample location in the mixing chamber, a base-temperature of ≈ 15 mK can be reached. The cryostat is equipped with a 15 T superconducting magnet. The lower section of the sample probe used for the top-loading cryostat is presented in Fig. 3.2. The chip carrier holding the ZnO sample was mounted on a rotating stage which can be controlled remotely. The stage is turned with the help of stainless steel strings attached to a motor at the top of the probe. In the configuration shown in Fig. 3.2, the external magnetic field points in the plane of the 2DES. A 90° rotation of the stage brings the sample surface perpendicular to the magnetic field direction. The angle θ between the normal to the 2DES and the B -field can be obtained from quantum Hall features. Shubnikov-de Haas oscillations are visible down to approximately 0.1 T, which allows the determination of θ with a precision of approximately 1° .

The sample probe is additionally equipped with a semi-rigid coaxial line which runs from the top of the probe down to the sample space. At the bottom, the inner conductor of the cable extends a few millimetres below the outer conductor, acting as an antenna. The top termination is connected through an adaptor to a flexible coaxial cable which is used to guide monochromatic microwave radiation up to 50 GHz generated by an Agilent 83650 B source.

For the experiments presented in the previous chapter an AC measurement setup was employed to reduce the signal-to-noise ratio. In the very dilute regime, however, where the 2DES displays insulating behaviour, the use of lock-in amplifiers is not advantageous. One reason is that the input impedance of most lock-in

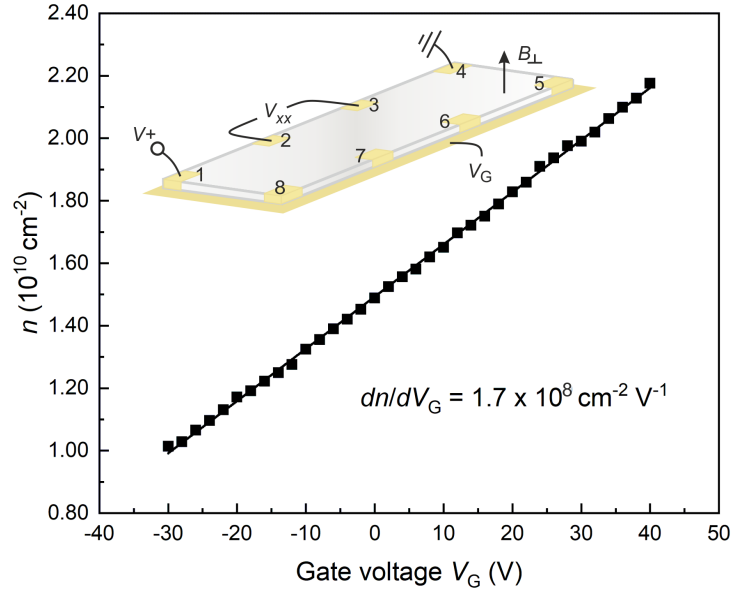


Figure 3.4: Charge carrier density as a function of backgate voltage. n has been obtained from SdHO. The line represents a linear fit which yields a modulation ratio of $1.7 \times 10^8 \text{ cm}^{-2} \text{ V}^{-1}$.

amplifiers is limited to $10 \text{ M}\Omega$, setting a relatively low maximum resistance which can be reliably measured. A second reason is that at such low densities capacitive coupling can occur at the sample leads. Both of these problems can be circumvented in the 4-point DC setup presented in Fig. 3.3. A Yokogawa 7651 source applies a DC voltage to the sample, which is connected in series with a $10 \text{ M}\Omega$ resistor. The role of the resistor is to limit the current through the sample. An Ithaco 1211 preamplifier collects the current at the drain, amplifies it and converts it to a voltage. Its output is measured with an Agilent 34401A digital multimeter. The potential drop along the sample is fed to an Ithaco 1201 voltage preamplifier. The amplified signal is read with the help of a second digital multimeter. The input impedance of the preamplifier is $1 \text{ G}\Omega$, two orders of magnitude larger than that of a lock-in amplifier. Bias to the backgate is provided by two Yokogawa 7651 sources connected in series (not shown in Fig. 3.3).

The 2D electron density represents an important parameter in the study of metal-insulator transitions and Wigner crystals as the strength of electron-electron interaction is directly correlated to it. In situ control of the electron concentration is achieved here with the aid of a backgate. The device can be understood as a parallel plate capacitor, where one of the plates is the 2DES and the other the metallic layer on the back side of the sample. The capacitor dielectric is represented by the ZnO substrate. Demonstration of the gating effect is shown in Fig. 3.4, where n was obtained from the Shubnikov-de Haas at base temperature. The modulation ratio

$dn/dV_G = 1.7 \cdot 10^8 \text{ cm}^{-2} \text{ V}^{-1}$ allows us to estimate the device capacitance:

$$C_{\text{ZnO}} = eA \frac{dn}{dV_G} = 2.18 \text{ pF}. \quad (3.1)$$

Taking $\epsilon = 8.3\epsilon_0$ as the dielectric constant, we obtain the value of $270 \mu\text{m}$ for the ZnO layer thickness. With $500 \mu\text{m}$ the total thickness of the sample we can conclude that the 2DES is buried approximately $220 \mu\text{m}$ below the surface. These results agree well with the thickness values obtained in the growth process.

Some of the data presented here were taken in a Leiden Cryogenics refrigerator equipped with a home-built ^3He cell. The full set of experiments and the description of the setup have been published in Ref. [83].

3.2 Transport characterization

3.2.1 Temperature dependent study

According to the scaling theory of localization developed by Abrahams et al. in Ref. [181], in the absence of an external magnetic field there is no true metallic behaviour in two dimensional systems ($\sigma_{T=0} \neq 0$). The argument is based on Anderson's theory of localization, which predicts that as long as disorder is present, particles can be scattered back to their starting point. Constructive interference between the forward and the backward propagating wave leads to the trapping of carriers within a certain localization length. Experiments on early realizations of 2D devices where interactions between charge carriers and disorder dominate have indeed supported this theory. Fabrication of high-mobility two-dimensional systems has revealed a much more nuanced picture. In the low disorder limit the localization length exceeds the size of the system. In this regime the resistivity decreases with temperature, and the 2DES is considered to be metal-like. A common localization mechanism in relatively clean systems where the phase coherence length is longer than the transport scattering time is due to closed loops along possible percolation paths. This process, known as weak localization, brings a logarithmic contribution to resistance [182]. According to this model, as T approaches 0 K, weak localization would eventually lead to a vanishing conductivity [183].

Further insight was brought when a transition from insulator to metal (MIT) in the high-mobility regime was observed in 1987 in a Si MOSFET [184] and reproduced later in the same material [40]. A sharp decrease in resistivity as the temperature was reduced suggested a true metallic state. Moreover, using a single scaling parameter, resistivity traces could be collapsed onto the same curve on both sides of the transition [185]. The subject gained momentum and the MIT was reported in various other 2D systems, among which p -type GaAs [183, 186], n -type AlAs [187], p -type SiGe [188], and p -type Si/SiGe quantum wells [189]. In contrast to the early devices where scattering by impurities was dominant, in these systems the inter-particle correlations are strong enough such that their effect cannot be neglected. As a matter of fact, the MIT could only be observed in samples where the interaction parameter $r_s \gtrsim 5$. This has led to the possibility that both

the metallic and the insulating phases are aided by Coulomb repulsion. On the metallic side, correlations may suppress the quantum interference leading to weak localization [190]. On the insulating side, conduction could be reduced due to the formation of a Coulomb gap: a reduction in the single-particle DOS at the Fermi energy due to interactions. This manifests in an activated temperature dependence of the resistivity owing to variable range hopping (VRH) [191]. The Coulomb gap VRH should be distinguished from the Mott-like VRH, where interactions do not play a role [192].

When interactions are very strong ($r_s \approx 38$), the 2D system is expected to become a Wigner solid. In the presence of disorder, the electron solid is pinned at impurity sites, preventing crystal sliding and causing insulating behaviour. It is likely that the insulating phase occurs before the high r_s regime is reached, making the crystalline phase difficult to distinguish from a Mott insulator or a correlation-induced glass state. Here we attempt to investigate different localization models and their validity in the ZnO-based 2DES.

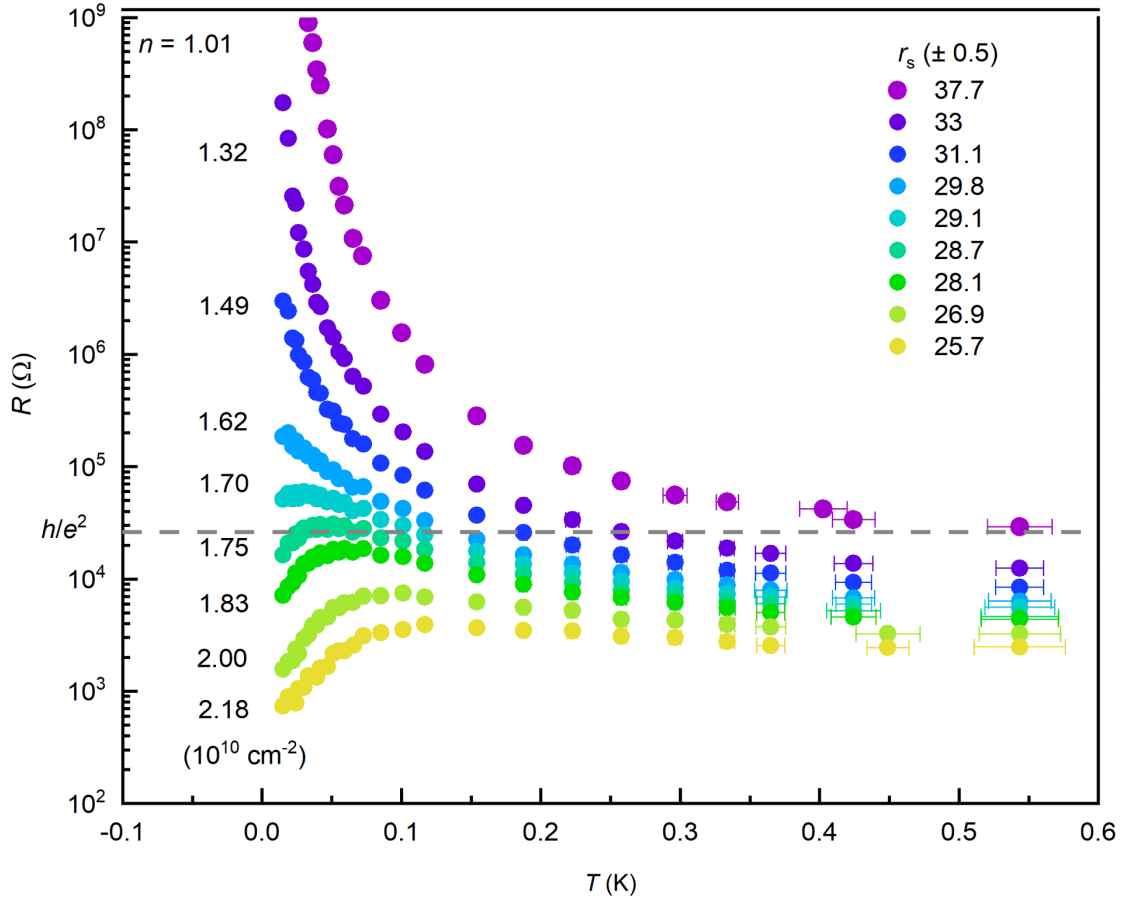


Figure 3.5: Apparent metal to insulator transition (MIT) as the density is tuned from $n = 2.18 \times 10^{10} \text{ cm}^{-2}$ to $n = 1.01 \times 10^{10} \text{ cm}^{-2}$. The corresponding interaction parameter is marked in the legend. At the critical density $n_c \approx 1.7 \times 10^{10} \text{ cm}^{-2}$ the resistance is of the order of $2h/e^2$. In the metallic phase $R(T)$ displays a local maximum at a T_{max} which varies with n . On the insulating side the resistance spans over four orders of magnitude, showing no sign of saturation down to base T .

In Fig. 3.5 we present a metal to insulator transition in the dilute sample S4682 at $B = 0$ T. The curves correspond to different charge carrier densities between $1.01 - 2.18 \times 10^{10} \text{ cm}^{-2}$, spanning the interaction strength range $r_s = 25.7 - 37.7$. The temperature was tuned from ≈ 550 mK down to base $T \approx 15$ mK. Each data point was extracted from individual $I - V$ curves in the low current limit ($I < 1$ nA). This is necessary due to the high degree of $I - V$ non-linearity at low density, but it is also a means to reduce Joule heating of the sample. At high density ($n > 1.70 \times 10^{10} \text{ cm}^{-2}$) the system behaves like a metal with the resistance decreasing as the temperature is reduced. At low density ($n < 1.70 \times 10^{10} \text{ cm}^{-2}$), the system exhibits insulating behaviour - the resistance increases as the sample is cooled down. The density at which the transition occurs is approximately $n_c = 1.70 \times 10^{10} \text{ cm}^{-2}$. Here the resistivity stays almost constant below $T \approx 40$ mK and it is approximately equal to h/e^2 at base temperature.¹ This is in accordance to the Ioffe-Regel criterion for the metal-insulator transition, in which the Drude mean-free path is equal to the Fermi wavelength ($k_F l \approx 1$).

The critical density corresponds to an interaction parameter of $r_s \approx 29$, which is comparable to the recently reported critical value in AlAs, where $r_s \approx 27$. While in most studies the critical value of r_s is larger than 5, the interaction strength varies widely across materials. As a rule of thumb the transition occurs at lower n (higher r_s) for samples of higher mobility. This may suggest that indeed disorder plays an important role in carrier localization.

Turning our attention to the metallic side of the transition, one may notice that $R(T)$ is non-monotonic over the temperature range of interest. At low T , $dR/dT > 0$ as expected from a metal. However, at a certain $T_{\text{max}}(n)$ the resistance displays a reduction with increasing temperature. Eventually, at higher T (> 600 mK, not shown here) dR/dT changes sign again, indicating that conductivity is limited by phonon scattering. We note that the peak in R occurs well below the onset of the Bloch-Grüneisen (BG) regime given by the temperature:

$$T_{\text{BG}} = 2\hbar k_F v_s / k_B = 2.2 \dots 2.5 \text{ K}, \quad (3.2)$$

where we have used the average between the longitudinal and the shear velocity $v_s = 4400$ m/s [193]. As seen in the previous chapter, the resistance of the Fermi liquid system saturated below the BG regime: as the phonons modes freeze out, scattering off impurities is the only mechanism limiting mobility. Here however we observe the resistance dropping by a factor of 2 – 5 from T_{max} down to base T . This may be an indication of temperature-dependent screening of charged impurities at low n [194]. The local maximum in $R(T)$ can then be attributed to the quantum to classical crossover where the renormalized Fermi energy approaches the carrier thermal energy. The two parameters are indeed comparable, as seen in Fig. 3.6 for a selected number of carrier density values.²

While the temperature dependence below T_{max} for $n > 1.70 \times 10^{10} \text{ cm}^{-2}$ is

¹Throughout this chapter we present the results in terms of the resistance. This is due to the fact that calculating the resistivity using the van der Pauw method has proven challenging. The estimation $\rho \approx h/e^2$ at the MIT should be taken with caution.

² T_{F}^* is calculated using the renormalized effective mass m^* extracted from magnetic field dependent measurements. See Section 3.1.5 for details.

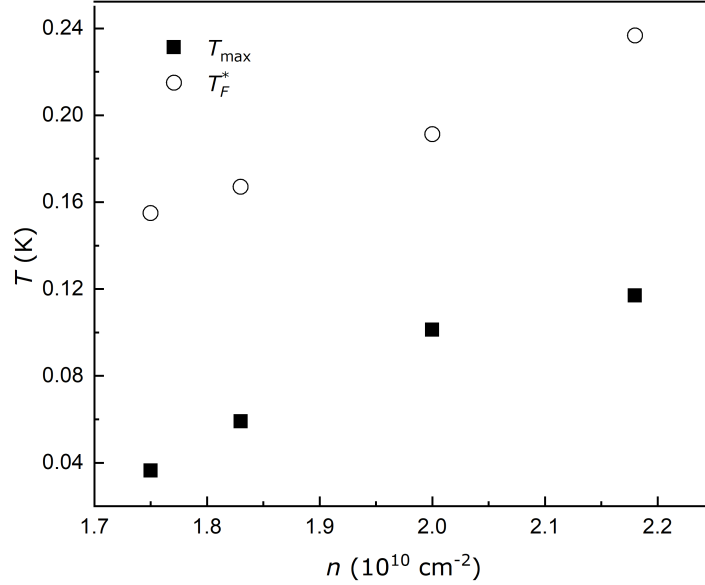


Figure 3.6: Comparison between the temperature T_{\max} where the local maximum in $R(T)$ occurs and the renormalized Fermi temperature T_F^* .

suggestive of a metallic phase, there is no practical way to test whether the condition $\sigma(T = 0) \neq 0$ for a true metal is met. To our knowledge there is also no theoretical model for disordered and strongly correlated systems which predicts a finite conductivity at zero temperature. For the sake of simplicity we shall refer to the regime where $n > 1.70 \times 10^{10} \text{ cm}^{-2}$ as the metallic phase.

Shifting our focus on the low density regime, we notice that $dR/dT < 0$ for the entire range of temperature. As in the case of the metallic phase, the derivative changes sign at high T where phonon scattering becomes important. The resistance increases dramatically as the temperature is lowered, reaching the upper limit of our experimental capabilities ($\approx 1\text{G}\Omega$). For the lowest density, $n = 1.01 \times 10^{10} \text{ cm}^{-2}$, R rises over four orders of magnitude. It is therefore very tempting to associate this behaviour with an insulating phase. However we cannot completely exclude that accessing lower temperatures may reveal a change in derivative sign. Again, for all practical purposes, we will refer to this regime as the insulating phase.

To identify the carrier localization mechanism, it is useful to characterize the temperature dependence of individual curves. Generally, the resistance in an insulating state can be described by:

$$R(T) \propto R_0 \exp \left[\left(\frac{T_0}{T} \right)^\beta \right], \quad (3.3)$$

where the prefactor R_0 can have a weaker than exponential T -dependence and T_0 is some characteristic temperature. The exponent β dominates the behaviour of R and varies with the transport mechanism. Mott predicted [196] that in a disordered sys-

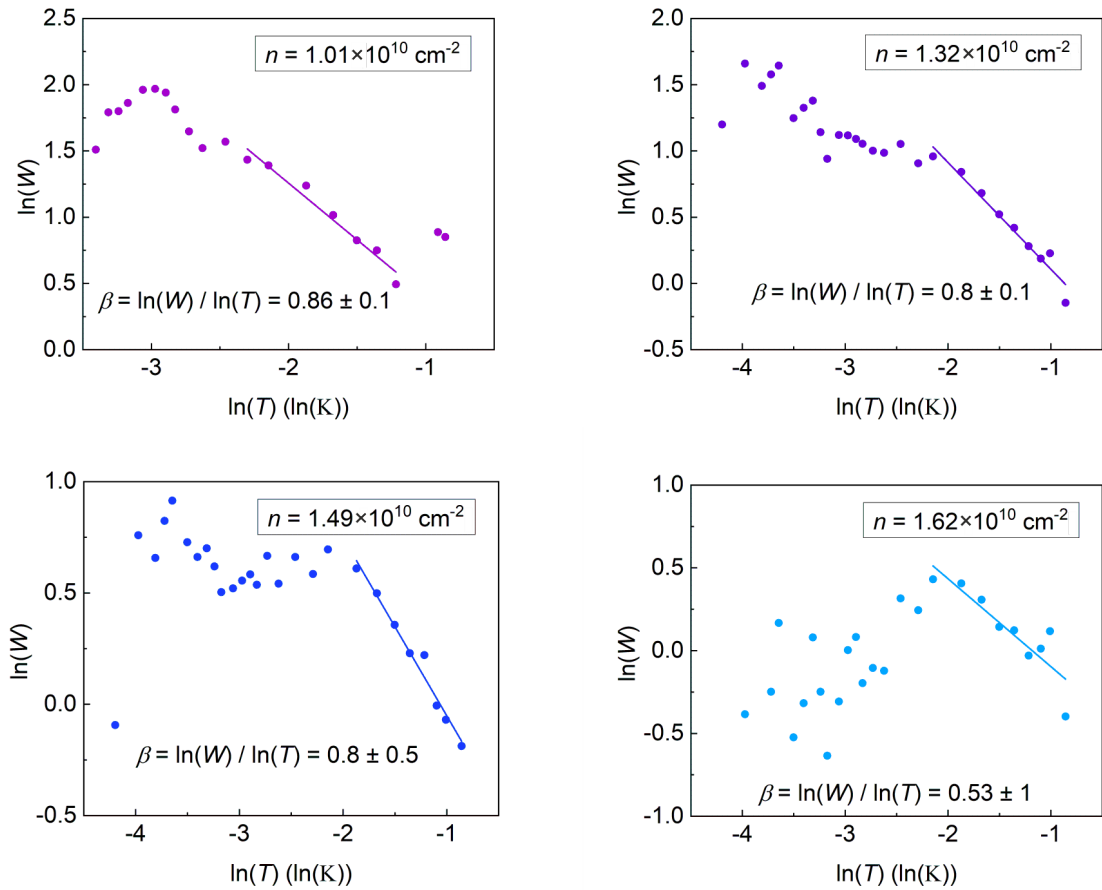


Figure 3.7: Zabrodskii-Zinov'eva method [195] for analysing the temperature dependence in the insulating phase. Each panel corresponds to a different carrier density, as marked. The high- T range can be approximated to the exponential law in Eq. 3.3 where $\beta = 0.86, 0.8, 0.8, 0.53$ for $n = 1.01, 1.32, 1.49$ and $1.62 (\times 10^{10} \text{ cm}^{-2})$, respectively.

tem with a constant density of states at the Fermi level, conduction occurs through hopping between sites which are located within variable distance (giving it the name variable range hopping). The exponent corresponding to this transport mechanism is $\beta = 1/3$. Efros and Shklovskii have shown [197] that, if correlations are sufficiently strong ($r_s \gg 1$), a gap in the density of states can open at the chemical potential. Coined the Coulomb gap, this depletion of states due to inter-particle repulsion leads to an exponential law with $\beta = 1/2$. A simple Arrhenius-type activation with $\beta = 1$ can also occur. This law does not pin-point a certain transport mechanism. Among the contenders which are described by an Arrhenius activation law is the formation of a “hard gap” in the DOS, as suggested for example in Ref. [198]. Unlike the Coulomb gap where the DOS vanishes only at $E = E_F$, the “hard gap” has a finite width. Excitations over the gap leads to an Arrhenius temperature dependence. This behaviour however is by no means universal. More recent studies of high-quality systems point to non-activated behaviour in the strongly-interacting regime [199, 200]. A more plausible explanation for the $\ln(R) \propto T^{-\beta}$ law is thermal activation of localized carriers in Anderson insulators [191, 201].

To facilitate the temperature-dependent analysis we employ the Zabrodskii-Zinov’eva method [195]. Using Eq. 3.3, we define the local activation energy:

$$W = -\frac{d \ln R}{d \ln T} = \beta \left(\frac{T_0}{T} \right)^\beta + \alpha, \quad (3.4)$$

where we considered $R_0 \propto T^{-\alpha}$. Assuming the first term on the right-hand side much larger than the second term (which is true for exponential dependence), we can write:

$$\ln(W) \approx \ln(\beta T_0^\beta) - \beta \ln(T). \quad (3.5)$$

Plotting $\ln(W)$ against $\ln(T)$, we can obtain β from the slope. This is demonstrated in Fig. 3.7 for the first four curves in Fig. 3.5 corresponding to electron densities $n = 1.01 - 1.62 (\times 10^{10} \text{ cm}^{-2})$. At high temperatures ($T \gtrsim 100 \text{ mK}$) we can identify a linear dependence in $\ln(W)(\ln(T))$. The exponent β varies from 0.86 at the lowest density to 0.53 at the highest. A transition to a different regime is apparent at lower T where the data deviates from a simple linear function. Given the high degree of scatter, it is difficult to draw conclusions on the exponential law. A similar analysis performed on the same sample in Ref. [83] suggests a crossover between an activated behaviour at large T and a Coulomb gap law with $\beta = 1/2$ as T is reduced.

The temperature dependence curves can also be analysed using an approach similar to one used in Ref. [199], namely by fitting Eq. 3.3 with T_0 and β as parameters to be determined. Following this method however leads to an unphysically large T_0 .

Finally, inspired by the results in Ref. [83], a third approach was tested: assuming $\beta = 1/2$, we plot $\ln(R)$ against $T^{-1/2}$, as shown in Fig. 3.8. A linear fit is then performed in the low T regime. From the slope one obtains $T_0 = 0.016 \text{ K}$ for $n = 1.62 \times 10^{10} \text{ cm}^{-2}$ and $T_0 = 8.24 \text{ K}$ for $n = 1.01 \times 10^{10} \text{ cm}^{-2}$. In the Coulomb gap model, the characteristic temperature is connected to the correlation length ξ by [191]:

$$T_0 = \frac{6.2e^2}{4\pi\epsilon k_B \xi}. \quad (3.6)$$

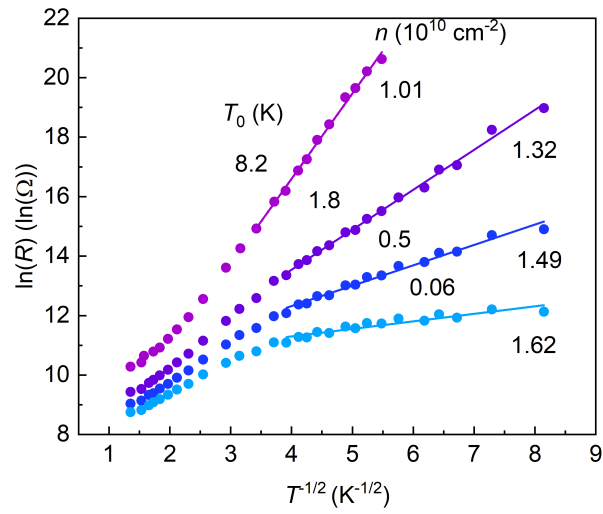


Figure 3.8: Temperature scaling analysis assuming an Efros–Shklovskii exponential law ($\beta = 1/2$). The traces correspond to four different charge carrier densities below n_c . The characteristic temperature T_0 is obtained from linear fits in the low- T regime ($T \lesssim 100$ mK).

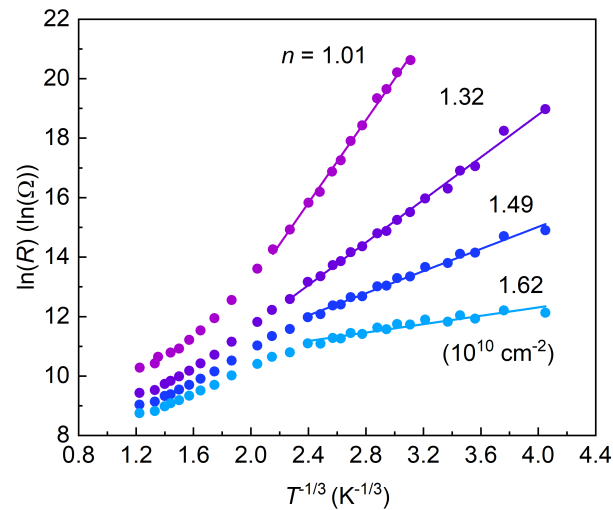


Figure 3.9: Temperature scaling analysis assuming a Mott-like exponential law ($\beta = 1/3$).

Using the above equation, one obtains $\xi \approx 20 \mu\text{m}$ at the lowest charge carrier density. The correlation length increases up to 2.5 mm for $n = 1.62 \times 10^{10} \text{ cm}^{-2}$. The steep rise of ξ close to the critical density is consistent with the divergence of the correlation length at the MIT. While this method provides accurate linear fitting ($R^2 \gtrsim 0.9$) and a qualitative agreement with theory, inconsistency with the Zabrodskii-Zinov'eva analysis may indicate an incomplete picture. A first obvious drawback of this approach is that it assumes a temperature independent prefactor. The Zabrodskii-Zinov'eva method circumvents this issue, as a dependency of the type $R_0 \propto T^{-\alpha}$ does not contribute to the slope of $\ln(W)(\ln(T))$. A second drawback is related to the narrow temperature range available for analysis. An exponential law with $\beta = 1/3$ can fit the data with comparable accuracy. Comparing Figs. 3.8 and 3.9 we conclude that this method alone is insufficient to determine the localization mechanism.

3.2.2 Electron pinning in an electric field

Transport in the insulating regime is often accompanied by non-linear current - voltage ($I - V$) characteristics. The origin of the non-linearity has been associated both with impurity-driven localization and interaction-related phenomena. By comparing the insulating phase ($\sigma_{xx} \rightarrow 0$) in quantum Hall regime with the low-density insulating phase in Si-MOSFETs, Shashkin et al. have concluded [202] that transport in the two cases occurs in a similar fashion: by applying a sufficiently large electric field, carriers localized by disorder gain enough energy to percolate through the sample. This mechanism can be explained in the single-particle picture for a regime where the disorder potential $e\langle V_{\text{dis}} \rangle$ dominates over the Coulomb energy. A combination of finite disorder and strong interactions may also lead to non-linear $I - V$ characteristics. In the theory of Efros and Shklovskii (ES), transport is mediated by variable range hopping of carriers in the presence of a Coulomb gap. The field effect (FE) model of ES-VRH predicts that at electric fields satisfying $k_{\text{B}}T/eL_{\text{FE}} < E_{\text{FE}} < k_{\text{B}}T/el_0$, the conduction is described by the equation [203]:

$$\sigma(T, E_{\text{FE}}) = \sigma(T, 0) \exp\left(\frac{eE_{\text{FE}}L_{\text{FE}}}{k_{\text{B}}T}\right). \quad (3.7)$$

Here l_0 is the average distance between impurities and L_{FE} is a characteristic length scale which depends on temperature. A second model describing conduction in the Coulomb gap regime is the so-called hot-carrier (HE) model: the electric energy is transferred to the charge carriers which are unable to thermalize with the lattice due to weak electron-phonon coupling. This leads to a higher effective carrier temperature T_{eff} than the bath T . The conductivity then only depends on the effective temperature [203]:

$$\sigma(T, E_{\text{HE}}) = \sigma(T, 0) \propto \exp[-(T_0/T_{\text{eff}})]. \quad (3.8)$$

Strong non-linear behaviour has also been used as evidence for the formation of a Wigner solid pinned at impurity sites [20, 31, 32, 41]. This crystalline order is defined by a characteristic domain size or correlation length. A finite threshold voltage corresponds to the energy required for depinning, leading to the Wigner

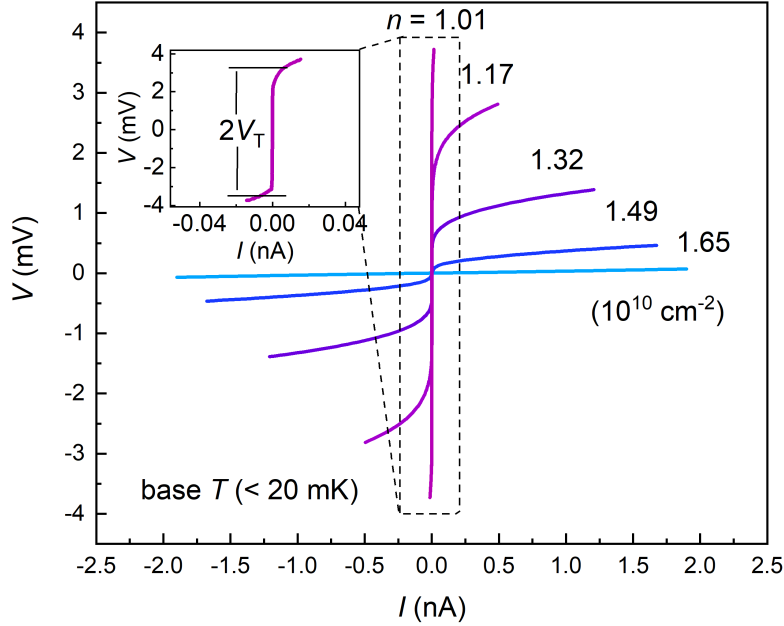


Figure 3.10: $I - V$ characteristics recorded in a four terminal configuration for the different charge carrier densities marked next to each trace. A strong non-linearity develops below $1.6 \times 10^{10} \text{ cm}^{-2}$. Inset: view of $V(I)$ at $n = 1.01 \times 10^{10} \text{ cm}^{-2}$ in a narrower current range.

crystal to move as a whole.

At sufficiently low temperatures and charge carrier densities strong non-linear current - voltage characteristics are also present in our ZnO-based 2DES. Figure 3.10 displays the evolution of $I - V$ curves with decreasing electron density, measured at base temperature. At high carrier concentration ($n \gtrsim 1.83 \times 10^{10} \text{ cm}^{-2}$), the traces are linear. As n is reduced, the $I - V$ curves become gradually rounded in the vicinity of zero current. In the interval $1.65 \lesssim n \lesssim 1.83 (\times 10^{10} \text{ cm}^{-2})$ the characteristics contain a region of “excess conductivity”: dV/dI presents a minimum at low current and seems to saturate at high I . Representative traces of this regime are shown in Fig. 3.11. Similar behaviour in the vicinity of the MIT has been reported elsewhere [19, 204]. Its origin is currently unclear and we cannot exclude it is an effect of Joule heating.

As the electron density is reduced below $n \approx 1.6 \times 10^{10} \text{ cm}^{-2}$, the minimum in dV/dI converts into a peak around $I = 0$. For $n \leq 1.6 \times 10^{10} \text{ cm}^{-2}$ the $I - V$ traces develop a sharp threshold voltage V_T below which I tends to zero. Above V_T , the current is “switched on”, leading to a reduced and almost constant dV/dI . Figure 3.12 displays the $I - V$ characteristic at base T deep in the insulating regime ($n = 1.01 \times 10^{10} \text{ cm}^{-2}$). The high-current differential resistance rises at least two orders of magnitude below the threshold voltage.

The non-linearity becomes ever more pronounced at lower n . By taking 0.5 mm as the distance between the voltage electrodes we can estimate the threshold

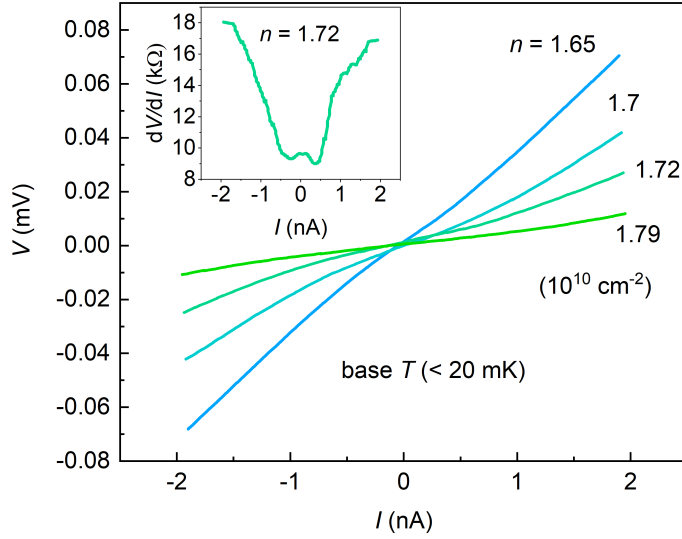


Figure 3.11: $I - V$ curves at intermediate densities $1.65 \leq n \leq 1.83$ ($\times 10^{10} \text{ cm}^{-2}$). A region of reduced resistivity can be identified in each trace at low current. Inset: dV/dI for $n = 1.72 \times 10^{10} \text{ cm}^{-2}$.

electric field: $E_T = V_T/0.5$.³ The resulting values are plotted in Fig. 3.13 as a function of charge carrier density. The dependency is well described by a fit of the form $E_T = C(n_T - n)^k$, with $k = 2.5 \pm 0.1$ and $n_T = 1.6 \times 10^{10} \text{ cm}^{-2}$. A similar analysis performed in Ref. [41] led to $k = 1.7 - 1.8$. We note that the density at which the threshold voltage vanishes, n_T , is close to the MIT critical density $n_c \approx 1.7 \times 10^{10} \text{ cm}^{-2}$.

In a single-particle (SP) picture of localization, conduction in the insulating regime occurs through charge carriers whose mean free path λ is larger than their de Broglie wavelength. An electric field can increase the mean free path such that, at sufficiently large fields, carriers are no longer pinned to impurities. Lee et al. have obtained the following expression for the threshold electric field necessary for delocalizing electrons [205]:

$$E_{\text{SP,T}} = \frac{mv_{\text{SP,T}}}{e\tau}, \quad (3.9)$$

where the limiting drift velocity $v_{\text{SP,T}}$ is given by:

$$v_{\text{SP,T}}^2 \sim v_{\text{F}}^2 \exp \left[- \left(\frac{4\pi}{3} k_{\text{F}} \lambda + \gamma \right) \right]. \quad (3.10)$$

Here γ is the Euler constant. Taking $\lambda = 6 \times 10^{-6} \text{ m}$ and $\tau = 6 \times 10^{-11} \text{ s}$, we obtain $E_{\text{SP,T}} = 0.15 \text{ V/m}$ for $n = 1.01 \times 10^{10} \text{ cm}^{-2}$. This value is significantly lower than the measured E -field of $\approx 3.3 \text{ V/m}$ at which the current switches on, suggesting that localization due to disorder alone cannot explain the large threshold voltage. Calculating the single particle energy $eE_T \langle r \rangle$ corresponding to the threshold field

³We define V_T as the voltage where 5 pA flows through the sample.

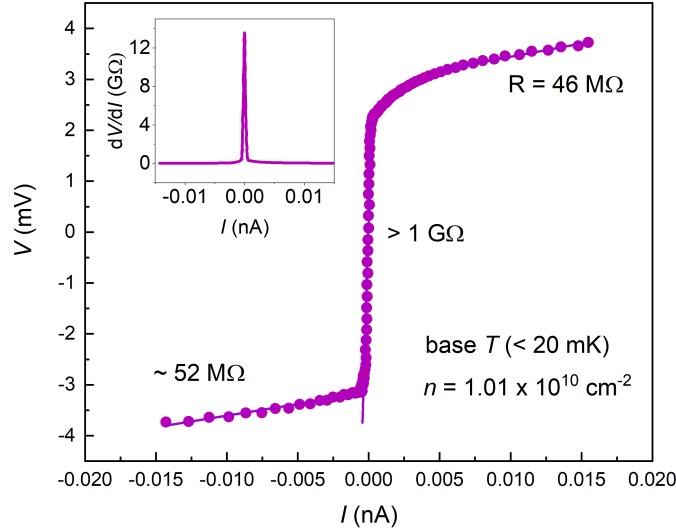


Figure 3.12: $I - V$ characteristic deep in the insulating regime ($n = 1.01 \times 10^{10} \text{ cm}^{-2}$) at base T . The differential resistance decreases sharply above the threshold voltage.

E_T , we obtain a value of $2 \text{ mK} < \text{base } T \approx 15 \text{ mK}$. The smallness of the SP energy compared to the bath temperature has been routinely used as an argument against single-particle localization models [20, 32]. This condition, however, is also met in systems where $I - V$ non-linearity is attributed to Anderson localization [202].

An attempt to address the $I - V$ non-linearity in the field effect ES-VRH model is illustrated in Fig. 3.14 for $n = 1.17, 23$ and $32 (\times 10^{10} \text{ cm}^{-2})$, where we plot the differential resistance (panel (a)) and the logarithm of conductivity (panel (b)) against the electric field. Equation 3.7 can be applied when $E_{\text{FE}} < k_B T / e l_0$ is satisfied. Taking $l_0 = 2 \times 10^{-5} \text{ m}$ as the average distance between impurities in our ZnO samples [149] and $T = 15 \text{ mK}$, we obtain an upper limit of 0.065 V/m . Turning our attention to Fig. 3.14(a) we observe that this value is well below the threshold E -field of $\sim 1.3 \text{ V/m}$. The resistance stays approximately constant up to this value. According to Eq. 3.7, however, the resistance should decrease exponentially with the field strength. Figure 3.14(b) reinforces the statement that no linear regime is seen in $\ln(\sigma/\sigma_0)$ at low E -fields. We therefore find it improbable that the low current and dilute regime is described by the field effect ES-VRH model.

Investigating whether the hot-electron model explains the non-linearity in $I - V$ requires careful temperature dependent measurements of the Joule power $P = IV$. A comparison between the change in resistance due to Joule and mixing chamber heating can yield a relation between power, electron temperature and bath temperature, as performed for example in Ref. [206] on n -type GaAs 2DES. Some studies suggest that the hot electron model applies to systems where the localization length is large, i.e. the ES temperature T_0 is small ($T_0/T < 135$), while the field effect model is more appropriate for $T_0/T > 135$ [206, 207, 208]. Using the ES analysis in Fig. 3.8 in the dilute regime we find $T_0 = 8.2 \text{ K}$ and $T_0/T \approx 547$, suggesting the

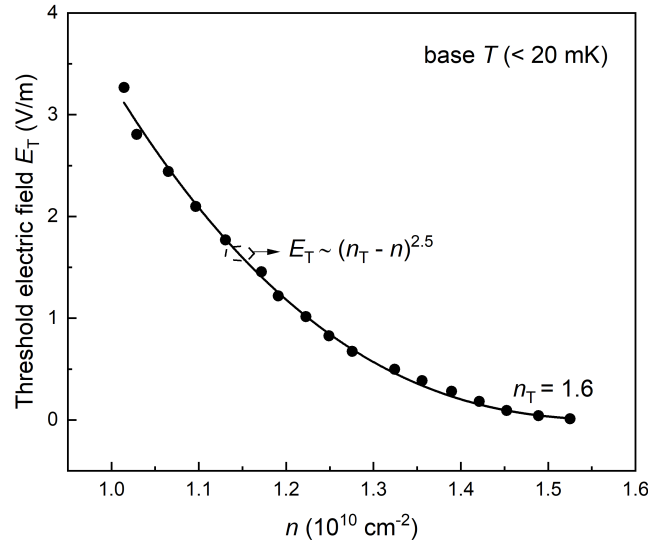


Figure 3.13: Threshold electric field $E_T = V_T/0.5$ as a function of electron density. Using $n_T = 1.6 \times 10^{10} \text{ cm}^{-2}$ as the carrier concentration at which the $I - V$ non-linearity vanishes, we find $E_T \sim (n_T - n)^{2.5}$.

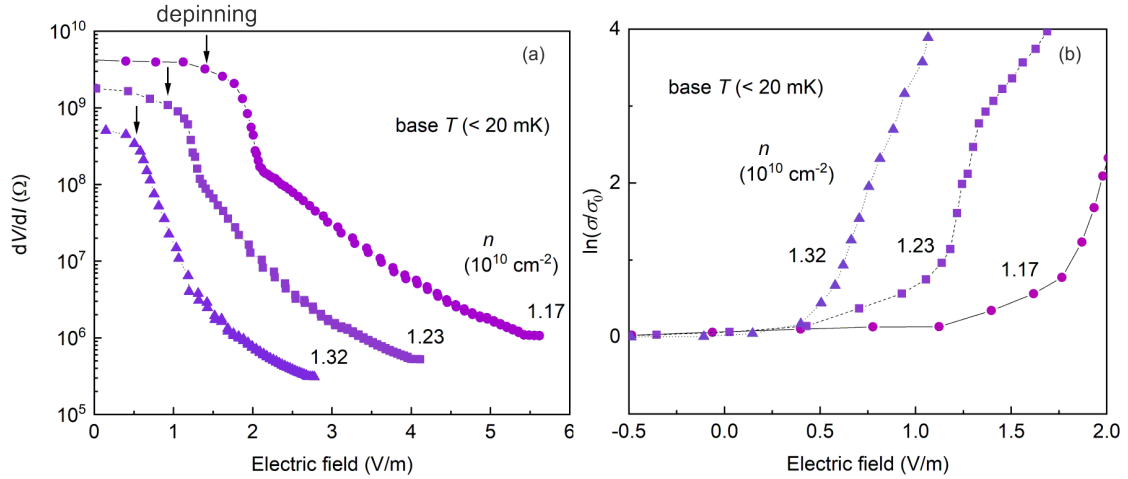


Figure 3.14: Examination of differential resistance dV/dI and logarithm of conductivity $\ln(\sigma/\sigma_0)$ as a function of electric field for $n = 1.17, 1.23$ and 1.32 ($\times 10^{10} \text{ cm}^{-2}$) at base temperature. Below the threshold electric field both quantities are approximately constant. A comparison between E_T and the upper limit electric field for the EF-induced VRH $E_{\text{EF},T} = 0.065 \text{ V/m}$ indicates that the EF model is inappropriate in this regime.

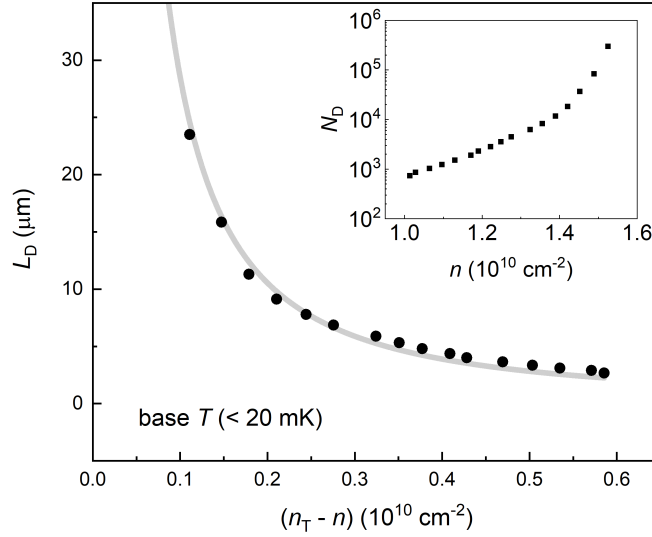


Figure 3.15: Estimation of the electron solid domain size L_D (main plot) and number of particles per domain N_D (inset) based on the weak pinning model in CDW. Following $E_T \sim (n_T - n)^{2.5}$, we obtain $L_D \sim (n_T - n)^{-1.25}$.

small localization length limit. However this argument alone is insufficient to rule out hot-electron effects. Detailed measurements on carrier heating can be performed in our setup and may present the subject of future research.

The strong non-linearity in $I - V$ along with large electron-electron interaction energy in our samples ($24 \lesssim r_s \lesssim 38$) may indicate the existence of a pinned Wigner solid, as commonly suggested for other systems with similar properties [19, 20, 32, 209]. Disorder determines the size L_D of the crystalline domains which contain on average $N_D = nL_D^2$ electrons. Using the model for weak pinning in charge density waves (CDW) [20, 32, 41], the force required to move a domain can be approximated to [210]:

$$F_D = \kappa \langle r \rangle, \quad (3.11)$$

where $\langle r \rangle = 1/\sqrt{\pi n}$ and the shear modulus κ is given by [28]:

$$\kappa = 0.245 \frac{e^2 n^{3/2}}{4\pi\epsilon}. \quad (3.12)$$

Conduction can then occur only when the electric force per domain exceeds the pinning force:

$$N_D e E_{WS,T} \geq \kappa \langle r \rangle. \quad (3.13)$$

Identifying $E_{WS,T}$ with the threshold electric field E_T in our $I - V$ characteristics, we plot in Fig. 3.15 the correlation length and the number of electrons per domain as a function of $n_T - n$ and n , respectively. Having $E_T \propto L_D^2$ and $E_T \propto (n_T - n)^{2.5}$ from Fig. 3.13, we find that $L_D \propto (n_T - n)^{-1.25}$, assuming the crystalline state survives up to the MIT. The drop in correlation length as n decreases has been associated to a transition to single particle localization in the extremely dilute regime where the

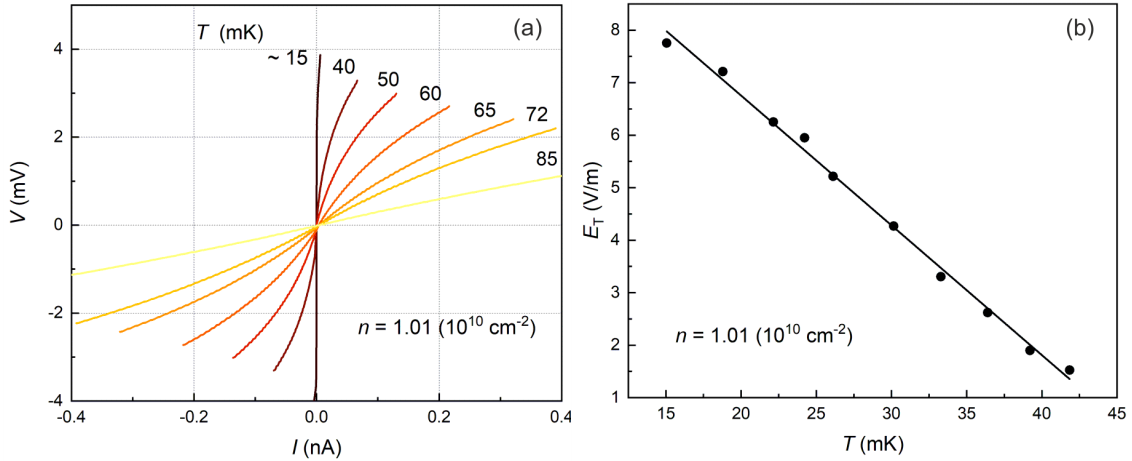


Figure 3.16: Temperature analysis of $I - V$ non-linearity for $n = 1.01 \times 10^{10} \text{ cm}^{-2}$. (a) $I - V$ curves at various temperatures, as marked. Linear $I - V$ profile is restored above $T = 85 \text{ mK}$. (b) Threshold electric field extracted from (a) as a function of temperature. The threshold disappears around $T = 40 \text{ mK}$.

L_D approaches $\langle r \rangle$ [41]. An electron density of $n = 1.01 \times 10^{10} \text{ cm}^{-2}$ corresponds to $\langle r \rangle = 5.6 \times 10^{-8}$ which is two orders of magnitude smaller than the corresponding correlation length $L_D = 2.7 \mu\text{m}$.

As the temperature is increased the $I - V$ non-linearity becomes less pronounced and eventually disappears. Figure 3.16(a) displays the $I - V$ characteristic at several temperatures and a constant electron density of $n = 1.01 \times 10^{10} \text{ cm}^{-2}$. At approximately 85 mK ohmic conduction is recovered. However a well-defined threshold voltage disappears much earlier, around 40 mK. Up to this temperature, E_T varies linearly with T , as shown in Fig. 3.16(b). In the Wigner crystal scenario, $T = 40 \text{ mK}$ can be associated with the melting of the electron solid.

3.2.3 Magnetoresistance in a perpendicular magnetic field

Applying an external magnetic field B_{\perp} perpendicular to the plane of the 2DES leads to Landau quantization of the energy spectrum described by Eq. 1.25. In Fig. 3.17 we plot the longitudinal resistance as a function of B_{\perp} for a set of different charge carrier densities. The traces are taken at base temperature. A constant voltage $V_{\text{bias}} = 20 \text{ mV}$ is used to bias the sample. In the very dilute regime, the magnetoresistance greatly exceeds the upper limit imposed by our experimental setup, which leads to a distorted signal. We therefore not present traces for $n < 1.17 \times 10^{10} \text{ cm}^{-2}$. In the interest of clarity, the traces were shifted vertically and, where needed, multiplied with a number, as marked.

Shubnikov-de Haas oscillations (SdHO) become visible at approximately 0.12 T. Using this onset value and Eq. 1.33, we obtain the quantum lifetime $\tau_q = 7 \text{ ps}$. This value is comparable to the τ_q of higher density ZnO-based 2DESs [150]. Both $\nu = 1$ and $\nu = 2$ states (with the filling factor ν given by Eq. 1.23) are visible down

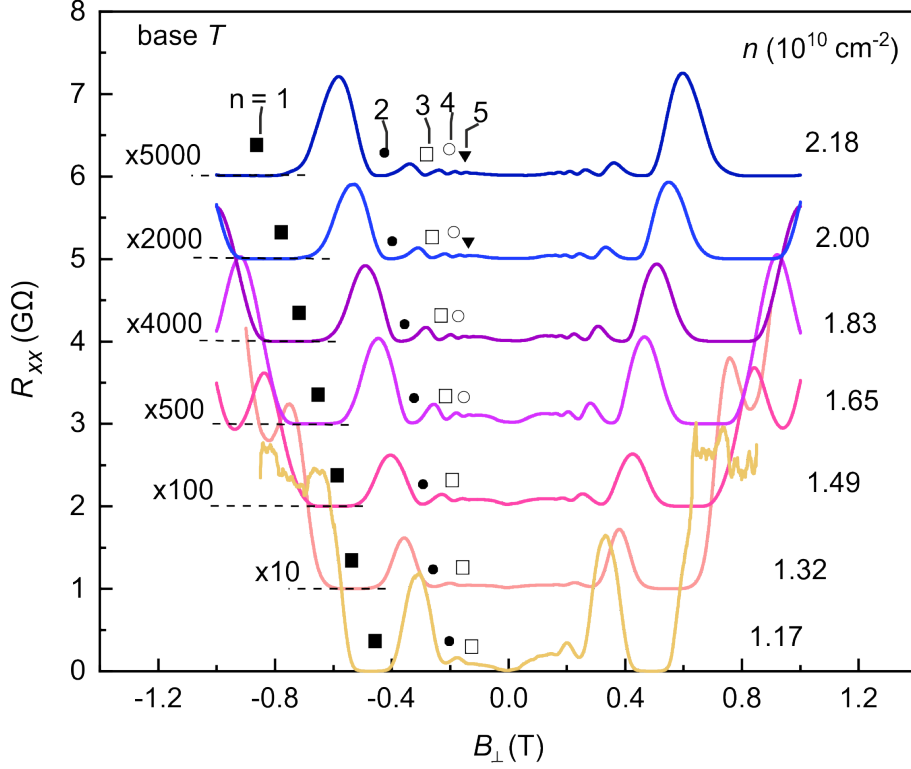


Figure 3.17: Resistance traces in perpendicular magnetic field for several charge carrier densities. Symbols mark the visible SdHO.

to $n = 1.17 \times 10^{10} \text{ cm}^{-2}$, which allows us to extract the carrier concentration with fairly good precision. At lower densities signatures of the $\nu = 1$ state are still visible, despite the high-impedance induced signal distortion.

A positive low-field magnetoresistance is present in each trace and it becomes ever stronger at low densities. This has been associated with a transition to a fully spin-polarized state, as discussed at large in the following section. The strength of the current flowing through the sample has a pronounced effect on both the low-field magnetoresistance as well as on the SdHO minima, as exemplified in Fig. 3.18 for $n = 1.8 \times 10^{10} \text{ cm}^{-2}$. In panel (a) the differential resistance at base temperature in the (B_{\perp}, I) plane is plotted. Panel (b) shows two line cuts corresponding to $I = 5 \text{ nA}$ (green trace) and $I \rightarrow 0 \text{ nA}$ (purple trace). The U-shaped magnetoresistance around zero field which is very prominent when $I \rightarrow 0$ nearly vanishes as the current is increased. Additionally the amplitude of the SdHO is overall reduced.

3.2.4 Magnetoresistance in a parallel magnetic field

An external magnetic field B_{\parallel} applied parallel to the plane of the 2DES couples only to the electron spin when the effective well width is small compared to the magnetic length l_B . In our dilute samples the 2DES thickness is approximately 10 nm [80], which is sufficiently small compared to the minimum value of $l_B = 20 \text{ nm}$ (for $B = 1 \text{ T}$) in these experiments. This thickness estimate should however be

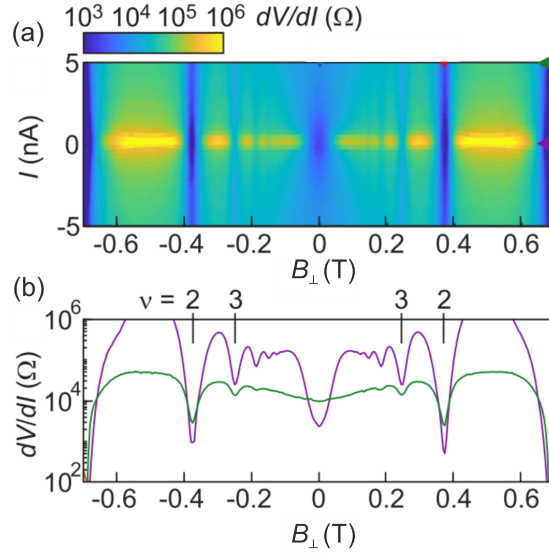


Figure 3.18: Effect of current intensity on the sample differential resistance. (a) Colour plot of dV/dI as a function of B and I . (b) Comparison between resistance traces at $I \rightarrow 0$ (purple) and $I = 5$ nA (green). (c) dV/dI versus current for $B = 0$ T (blue) and $B = 0.375$ T (red, corresponding to $\nu = 2$). (d) Power dissipation $P = IV$ as a function of current for $B = 0$ T (blue) and $B = 0.375$ T (red). From [83].

taken with caution as it is a mere extrapolation from higher density data.⁴ The net effect of B_{\parallel} is to shift the energy of the spin-up electrons with respect to the spin-down electrons as depicted in Fig. 3.19. The energy splitting between the two spin subbands is termed Zeeman energy E_Z and is given by Eq. 1.70. At sufficiently large B -fields where $E_Z = 2E_F$, the system becomes fully spin polarized, as illustrated in Fig. 3.19(c). The critical value of the magnetic field B_c where this occurs can then be written:

$$B_c = \frac{2\pi\hbar^2}{\mu_B} \frac{n}{g^*m^*} = \frac{2\pi\hbar^2}{\mu_B} \frac{n}{\chi^*}, \quad (3.14)$$

where χ^* is the spin susceptibility in Eq. 1.55. We have assumed that the g -factor and the effective mass entering the Zeeman and the Fermi energy, respectively, are the Fermi liquid renormalized parameters g^* and m^* . As we will see, this assumption holds true for the experimental technique used in this section for identifying the fully spin polarization state.

Due to the relatively few magnetic moments in the system, the magnetization M of a 2DES has been challenging to determine. Measurements using SQUID (superconducting quantum interference device) magnetometers [211] or micromechanical cantilevers [212, 213] are rare as they often involve home-built devices for improving sensitivity. A more practical method involves applying a modulated B -field in addition to the static field and measuring the out-of-phase component of the current

⁴Due to the small concentration of Mg in the cap layer, the QW barrier is expected to be low. Therefore the wave function may have a larger width than expected from the photoluminescence data at high n .

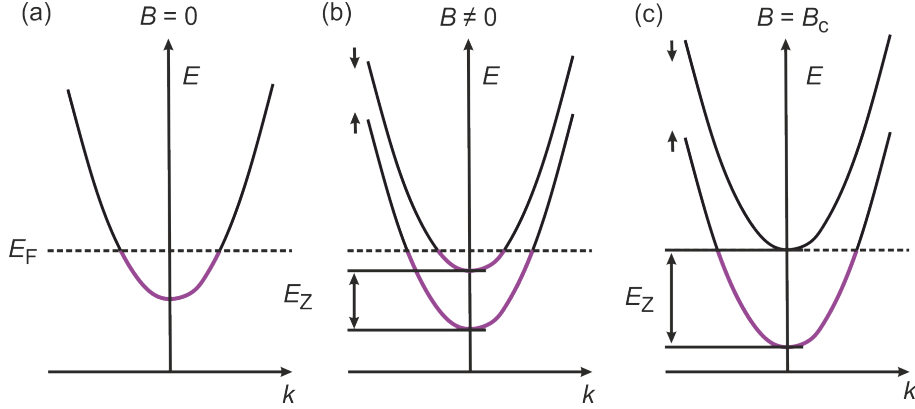


Figure 3.19: Schematic energy band diagram in k -space. The band is filled up to the Fermi energy E_F . (a) In the absence of a magnetic field the two spin subbands are degenerate. (b) If a magnetic field B is applied, the splitting between the spin subbands is given by the Zeeman energy E_Z . (c) At sufficiently large B -fields, the spin-down subband is completely depopulated and the system becomes fully spin polarized.

flowing between the gate and the 2DES. This quantity is proportional to $\partial M/\partial n$, which allows the determination of M by integrating the induced current over the carrier density. Employing this method in the vicinity of the MIT, Shashkin et al. [214] have shown that the spin susceptibility increases significantly with respect to the non-interacting value close to the critical density n_c .

A convenient method to determine the critical B -field necessary to polarize a 2DES relies on magnetotransport measurements. In a parallel magnetic field, the resistance increases sharply with B_{\parallel} and then stays approximately constant for $B_{\parallel} > B_c$ [215]. The effect is due to less efficient screening of disorder as the density of states is reduced by a factor of two [125, 216]. A comparison between thermodynamic magnetization data and magnetotransport measurements confirms that the 2DES is fully spin polarized at B_c [214].

In Fig. 3.20 we plot the voltage drop as a function of parallel magnetic field for several charge carrier densities. The measurement configuration employed is the same as described in Fig. 3.3. A constant bias voltage of $V_{\text{bias}} = 20$ mV was applied to the sample. In each trace a strong increase in the voltage is visible at low field, followed by a region of almost constant V . We associate the value of the magnetic field above which V saturates as the critical field B_c necessary to spin polarize the 2DES. The dashed lines demonstrate how we extract the critical field: the intersection point between an extrapolated low-field linear fit and the line corresponding to saturated V determines B_c . A small difference between B_c at negative field and at positive field arises due to trapped flux in the superconducting coil, resulting in an incorrect position of the data points on the horizontal B_{\parallel} axis. To eliminate this error, we take the average between the two values. The resulting dependence of B_c on charge carrier density is shown in Fig. 3.21 as black squares. Additionally we plot the resistance in the $(B_{\parallel} - n)$ plane. A dashed horizontal line marks the critical density n_c where the MIT occurs. Over the presented range of charge carrier concentration B_c is non-monotonic. Above n_c the critical field decreases steadily as

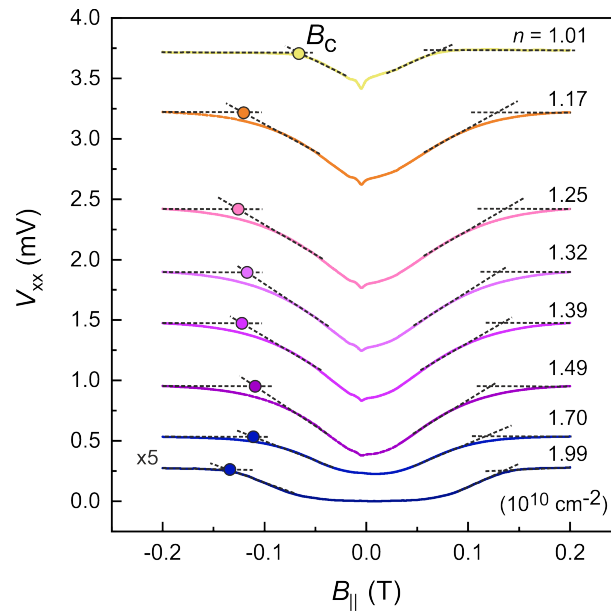


Figure 3.20: Voltage traces as a function of parallel magnetic field for several electron densities. The critical field B_c is extracted from the intersection point between the extrapolated lines corresponding to low-field linear increase and high-field saturation.

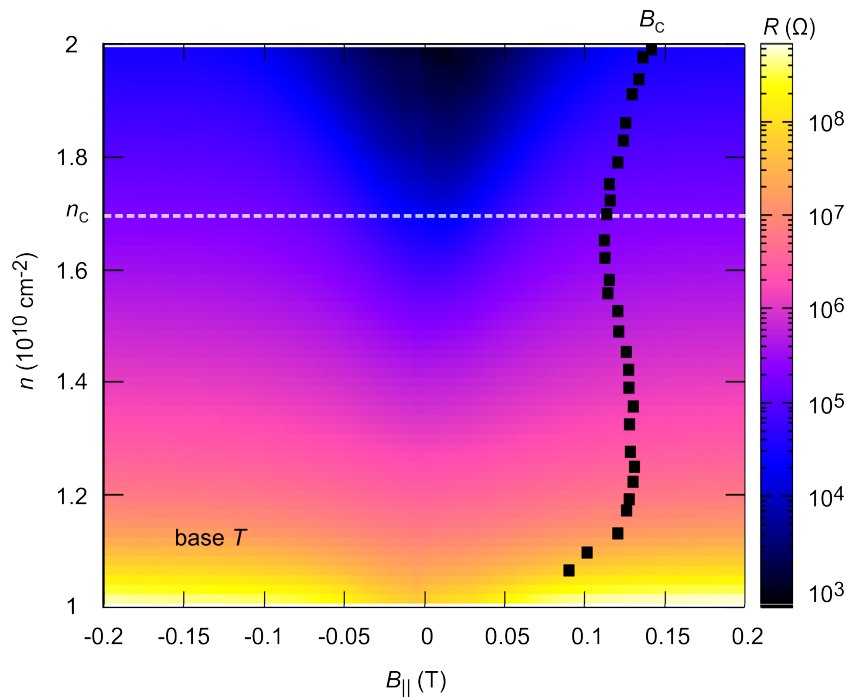


Figure 3.21: Mapping of the resistance in the $(B_{\parallel} - n)$ plane at base temperature. The MIT critical density n_c is indicated with a dash line. Solid squares mark the critical field at several densities.

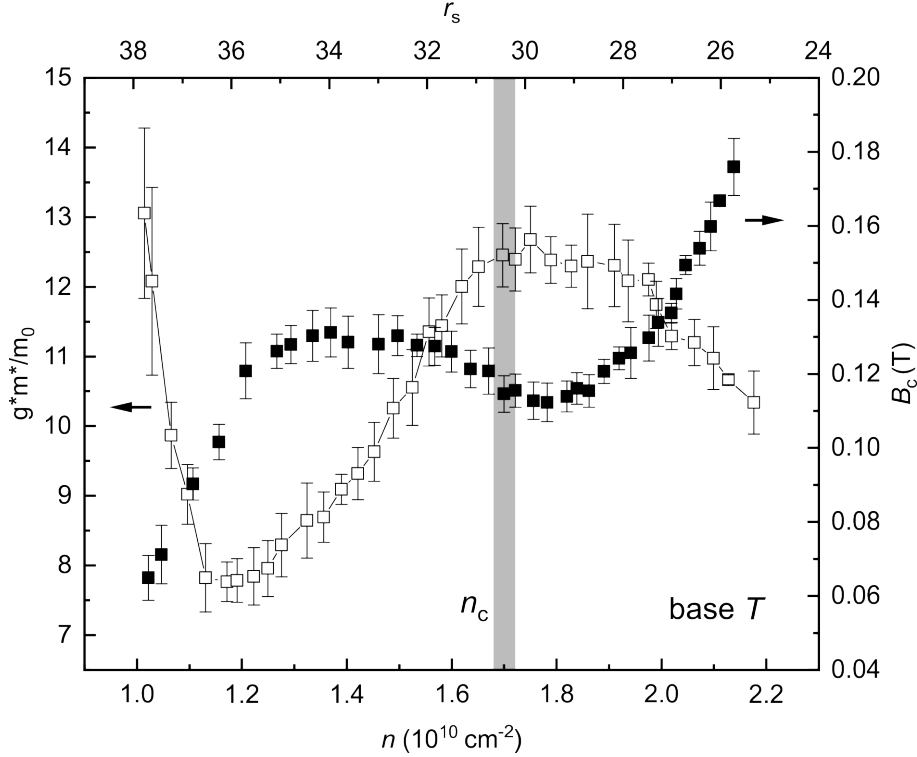


Figure 3.22: Dimensionless susceptibility χ^* (open squares) and critical magnetic field B_c (solid squares) as a function of electron density and r_s at base temperature. The critical charge carrier concentration is marked as a vertical grey box.

the density is reduced. An inflection point occurs at approximately $n = 1.6 - 1.7 \times 10^{10} \text{ cm}^{-2}$ followed by a rise in the interval $n = 1.6 - 1.2 \times 10^{10} \text{ cm}^{-2}$. Below this density B_c decreases steadily with n once again. Below $n \approx 1.01 \times 10^{10} \text{ cm}^{-2}$ the sample impedance becomes too large and signal distortion ensues.

Evaluating Eq. 3.14 we notice that the critical field should increase proportionally with carrier density. With the exception of spin susceptibility, the other parameters entering the equation are constants. This leads us to conclude that the product g^*m^* is indeed renormalized by interactions, as it is expected in the Fermi liquid model. Applying Landau's theory of interacting systems for such large values of r_s should however be done with caution, as it may be inappropriate in the vicinity of a phase transition. In the absence of a better theory, we will continue to mark the g -factor and the effective mass in the similar fashion as the Fermi liquid renormalized parameters. The dimensionless spin susceptibility g^*m^*/m_0 obtained from Eq. 3.14 is plotted against electron density (lower axis) and r_s (upper axis) in Fig. 3.22. Alongside we present the critical field. The non-monotonic behaviour of B_c and spin susceptibility with density is in contrast to several previous reports where both quantities varied monotonically with n [26, 124, 215, 217]. The critical increase of χ^* as the density is reduced has led to the hypothesis that a Stoner transition to a ferromagnetic state at zero field may occur at some finite carrier concentration. Most reports have arrived to this conclusion by extrapolating $B_c(n)$ to lower n [124, 215, 217]. In a recent study [26] the critical field decreases steadily with n until the magnetoresistance completely vanishes below a certain density cor-

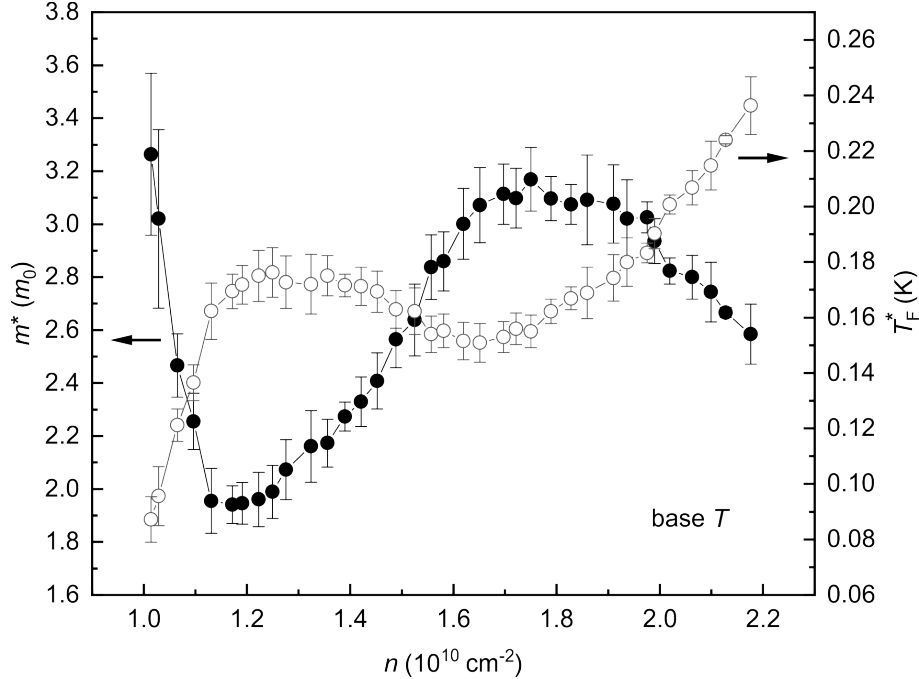


Figure 3.23: Electron density dependence of the renormalized effective mass (solid circles) and Fermi temperature (open circles). For these estimates a value of $g^* = 4$ was assumed.

responding to $r_s = 34.5$. This behaviour has been associated with spontaneous spin polarization of the 2DES.

Melnikov et al. have reported similar magnetoresistance experiments in Ref. [46] for a Si-MOSFET 2DES where $r_s \leq 12$. Here the authors distinguish between methods which probe the system as a whole (e.g. measurements of magnetization, the critical B -field or the thermodynamic density of states) and those which analyse the properties of carriers at the Fermi level (such as the temperature dependent measurements of SdHO). Examining the density dependence of the critical field they find that the product g^*m^* rises and then saturates at low n , while temperature dependent analysis of the SdHO yields an effective mass which increases steadily as n is reduced. Assuming that the g -factor remains constant, the authors have concluded that the effective mass extracted from the SdHO data reflects the spectrum flattening at the Fermi level due to fermionic condensation, while the values obtained from parallel-field measurements are only weakly affected by this flattening. This explanation does not seem to fit our dataset. While a local saturation occurs for values of n around the critical density, the susceptibility displays a more complicated dependence as n is lowered further.

Saturation of the critical field in the vicinity of the MIT has also been reported by Noh et al. in Ref. [218]. Making use of Eq. 1.54 which relates the Fermi liquid interaction parameter F_0^a to the g -factor g^* , the authors extract F_0^a as a function of density. This dataset is then compared to the values of F_0^a obtained by analysing the linear temperature dependence of the conductivity in the metallic regime ($n > n_c$) according to the theory of Zala et al. [219]. Both results display a non-monotonic dependence of the Fermi liquid parameter F_0^a with density in the vicinity of the MIT.

The renormalized g -factor g^* first increases with decreasing n and then exhibits a reduction down to $n < n_c$. The renormalized effective mass is shown to decrease and then saturate at lowest n . An overall reduction in the spin susceptibility g^*m^* follows as the MIT is approached. This result suggests that the two parameters, g^* and m^* , can contribute differently to the behaviour of χ^* .

So far measurements of χ^* and m^* in ZnO-based 2DESs suggest that the divergent behaviour of the susceptibility is due to a steep rise in the effective mass, while the g -factor remains almost constant (albeit twice as large as the band value) [121]. A similar trend was observed in Si-MOSFETs [22]. Assuming the renormalized g -factor remains constant $g^* = 4$, we can extract the values of m^* . In Fig. 3.23 we plot the result, alongside the values of the Fermi energy. This indirect way of obtaining the Fermi temperature was also employed in Fig. 3.6 where it is compared to the cross-over temperature T_{\max} . The renormalized effective mass is overall strongly enhanced with respect to the band mass: taking $m = 0.3m_0$, the enhancement ratio m^*/m varies non-monotonically from 8.6 at $n = 2.18 \times 10^{10} \text{ cm}^{-2}$ to 10.9 at $n = 1.01 \times 10^{10} \text{ cm}^{-2}$. Unlike in the low and intermediate density regimes presented in Chapter 2 where m^* increases monotonically with decreasing n , here in the ultra dilute system we observe a more complex behaviour which may be a consequence of instability in the vicinity of a phase transition. To our knowledge, there is currently no theoretical model based on the Fermi liquid paradigm which can account for these observations.

3.2.5 Temperature analysis of the resistance in a parallel B -field

In Section 3.1.2 we have seen that applying a parallel magnetic field strongly suppresses the conductivity as the 2DES is polarized. Fixing the charge carrier density to a value above $n = 1.6 \times 10^{10} \text{ cm}^{-2}$ and varying the temperature we find that the resistance decreases with increasing T above a certain value of the magnetic field B^* . This apparent metal-to-insulator transition [220] at finite B_{\parallel} is presented in Fig. 3.24(a)-(c) for three distinct electron concentrations. Open circles mark the values of B^* , which are then plotted against n in Fig. 3.24(d). A linear dependence on electron density is found which extrapolated to zero field yields $n = 1.6 \times 10^{10} \text{ cm}^{-2}$, which is close to the critical value n_c .⁵ Below this carrier concentration, the system displays an insulating behaviour (increasing resistance as T is reduced) for all values of the magnetic field. Temperature dependent measurements (see section 7 in Ref. [83]) in the regime $B > B^*$ and $n > n_c$ reveal that the conductivity varies linearly with T . According to Zala et al. [219], a linear dependence on temperature can be attributed to corrections due to electron-electron interaction in a spin polarized Fermi liquid. This result supports the assumption that the Fermi model can be

⁵The data in Fig. 3.24 and Fig. 3.27 have been gathered in a Leiden dilution refrigerator by J. Falson prior to the other measurements presented in this chapter. Due to repeated cooldowns it is expected that some qualitative results change slightly, such as the exact density at which the 2DES becomes insulating. This may explain why in Ref. [83] the carrier concentration at which B^* vanishes exactly matches the critical density $n_c = 1.6 \times 10^{10} \text{ cm}^{-2}$, but it is only comparable to the critical density $n_c \approx 1.7 \times 10^{10} \text{ cm}^{-2}$ estimated in this thesis.

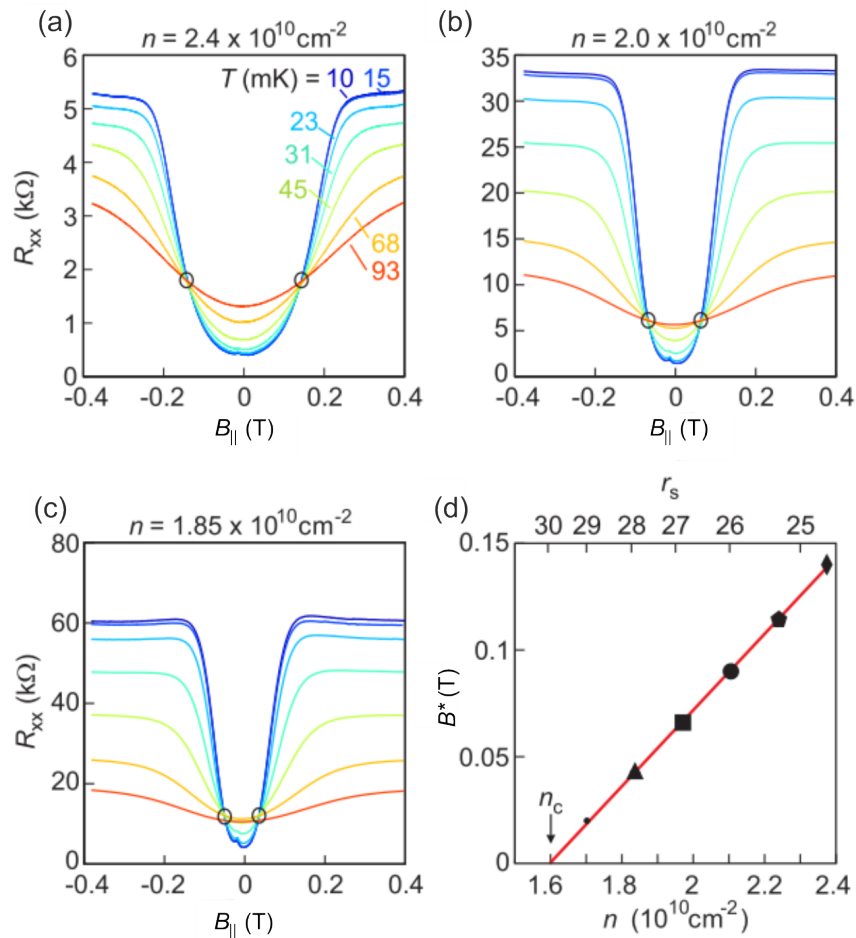


Figure 3.24: Apparent metal-insulator transition induced by a parallel magnetic field at (a) $n = 2.4$, (b) $n = 2.0$ and (c) $n = 1.85 \times 10^{10} \text{ cm}^{-2}$. Open circles mark the values B^* where MIT occurs. (d) Electron density dependence of B^* . A linear regression (red line) extrapolates at zero field to n_c .

applied at least down to the critical density n_c .

3.2.6 Transition to a spin-ordered state

The possibility of a ferromagnetic (Stoner) instability in a strongly interacting itinerant liquid has been a topic of intense debate. Theoretical calculations using Monte Carlo simulations [24] predict that a fully spin polarized phase occurs above a value of 26 of the interaction parameter r_s . Recent magnetotransport measurements performed on an AlAs-based 2DES [26] support the theoretical claims in Ref. [24]. Extracting the magnetic field required to polarize the 2DES in a similar fashion as presented in Section 3.1.5, the authors find that below a certain value of the carrier density corresponding to $r_s = 34.5$ the resistance becomes independent of the in-plane field. The strong magnetoresistance below $r_s = 34.5$ followed by its vanishing as r_s is increased above 34.5 is interpreted as a transition from a paramagnetic to a ferromagnetic state: for a spin-less (fully spin polarized) system where orbital effects can be neglected the resistance is independent of B_{\parallel} . While the results in Ref. [26] are in accordance with the expected behaviour around a ferromagnetic transition, it is important to point out that the experiments were carried out at a relatively high temperature, namely at $T = 300$ mK. Depending to which degree the renormalized parameters, g^* and m^* , individually contribute to the susceptibility enhancement, the Fermi energy can be larger or comparable to the thermal energy. The latter case is undesirable as it may diminish magnetoresistive features, leading to false conclusions.⁶ It would therefore be helpful to aid the study with direct measurements of the quasi-particle mass in the proximity of the ferromagnetic transition to obtain a relevant comparison between different energy scales. While a spin-polarized state agrees fairly well with the theoretical calculations in Ref. [24], it is not supported by more recent simulations reported in Ref. [25] where a paramagnetic-to-ferromagnetic Fermi liquid transition is ruled out from the phase diagram.

In Section 3.1.5 we investigated how the presence of a parallel magnetic field can fully spin polarize the 2DES. While the critical B -field displays an overall decrease as the density is reduced (from $B_c \approx 180$ mT at $n = 2.18 \times 10^{10}$ cm⁻² to $B_c \approx 60$ mT at $n = 1.01 \times 10^{10}$ cm⁻²), we observe no sign of spontaneous polarization at zero field. The spin susceptibility varies non-monotonically with n (thus excluding a divergent behaviour near a spin-ordered transition) and a finite magnetoresistance is present down to the lowest accessible carrier concentrations. Other similar experimental works on Si-MOSFETs [222, 223] also report the absence of clear evidence for ferromagnetism in the strongly-interacting regime.

The aforementioned observations are qualitatively consistent with the Quantum Monte Carlo (QMC) calculations in Ref. [25]. An adapted version of its main result is illustrated in Fig. 3.25, where the energy at $T = 0$ of different competing states

⁶Reference [26] only reports the renormalized susceptibility χ^* , which is insufficient to calculate the interaction-modified Zeeman energy and the Fermi energy, which depend on the g -factor g^* and the effective mass m^* , respectively. Calculating E_F at the ferromagnetic transition ($n = 2 \times 10^{10}$ cm⁻²) using the band mass $m = 0.46 m_e$ yields 1.2 K, which is well above the bath temperature. However, according to a study performed on a similar AlAs-based 2DES [221], the effective mass is greatly enhanced as n is reduced. An increase in the effective mass may bring the Fermi temperature on equal footing with the bath temperature.

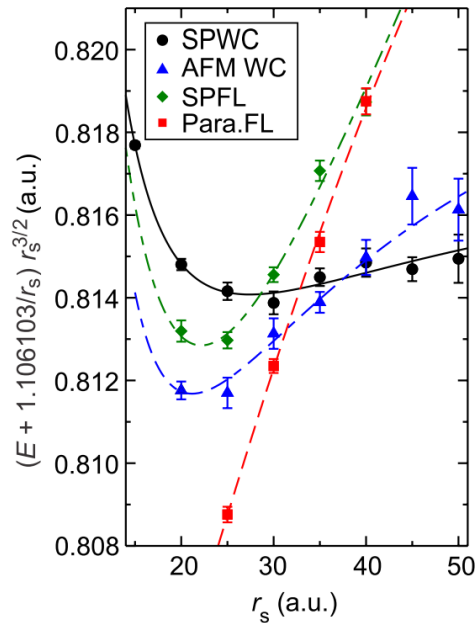


Figure 3.25: Energy per electron against r_s for four different states: spin polarized Wigner crystal (SPWC, circles), antiferromagnetic Wigner crystal (AFM WC, triangles), spin polarized Fermi liquid (SPFL, diamonds) and paramagnetic Fermi liquid (Para. FL, squares). Adapted from Ref. [25].

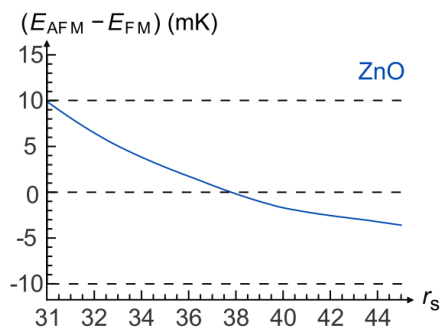


Figure 3.26: Energy difference between the spin polarized Wigner crystal and the antiferromagnetic Wigner crystal as a function of r_s in ZnO using the Quantum Monte Carlo results in Ref. [25].

is plotted against the interaction parameter. Included in the calculations are the unpolarized paramagnetic Fermi liquid (Para. FL), the spin polarized Fermi liquid (SPFL), the unpolarized antiferromagnetic (AFM) Wigner crystal (AFM WC) and the spin polarized Wigner crystal (SPWC). At low r_s the paramagnetic FL state is preferred. As the interactions become stronger ($r_s > 30$), the lowest energy state is replaced by the antiferromagnetically aligned WC and then by the spin polarized WC. For all values of the interaction parameter the spin polarized Fermi liquid is excluded as the ground state.

Although a spin polarized WC is expected at large r_s , its energy is close to the one of antiferromagnetically aligned WC. Therefore a finite experimental temperature may blur a transition between the two states. To verify this, we compute the difference $E_{\text{AFM}} - E_{\text{FM}}$ between the ground state energies of the two WC spin-ordered states using the appropriate parameters for ZnO ($m = 0.3 m_e$ and $\epsilon = 8.5 \epsilon_0$). In Fig. 3.26 we plot the result in units of temperature against r_s . The maximum energy difference occurs at $r_s = 31$ where it is equal to 10 mK. Compared to our experimental base temperature (≈ 15 mK), it is likely that spin order (either AFM or FM) is destroyed by thermal fluctuations.

In Ref. [83] we have attempted to complete the QMC energy diagram in Ref. [25] by including the effect of a parallel magnetic field. Using parameters relevant to our ZnO 2DES, the resulting diagram was then compared to magnetotransport measurements taken on sample S6482. The outcome is shown in Fig. 3.27. Panel (a) displays a colour map of the resistivity at zero bias normalized by the resistivity at $I = 2.5$ nA in the (B_{\parallel}, r_s) plane. This type of representations emphasises the degree of non-linearity of $I - V$ characteristics across this parameter space: green, yellow and red regions correspond to linear, rounded and strongly non-linear $I - V$ s, respectively. Panel (b) illustrates the extended QMC diagram, where no free parameters were used.⁷ The diagram reinforces the assumption that above n_c the system can be described as a paramagnetic Fermi liquid which, in the presence of a sufficiently strong parallel magnetic field becomes a spin polarized Fermi liquid. Based on the diagram, the field required to polarize the 2DES can either be the critical field B_c (dashed line) or the field B^* associated with the suppression of the conductive phase (dotted line). Below n_c , the QMC diagram predicts that the 2DES crystallizes into a Wigner solid. The strong non-linearity of the $I - V$ curves characterized by a large pinning potential supports this view. The nature of the spin texture in the WC state is more challenging to assess. According to the diagram, at zero field the spins are aligned with respect to each other antiparallel for $30 < r_s < 35$ and parallel for $r_s > 35$. However, as argued above, the smallness of the energy difference $E_{\text{AFM}} - E_{\text{FM}}$ with respect to the experimental temperature makes it improbable that a spin ordered state sets in. The existence of a finite magnetoresistance for all values of n supports this view.

⁷For more details on how the energy diagram was obtained and a comparison between different scenarios, see the Supplementary information of Ref. [83].

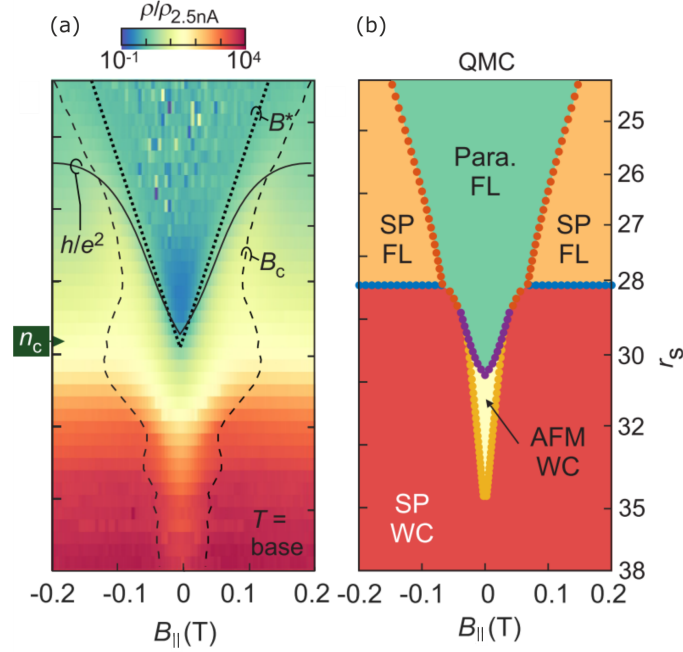


Figure 3.27: Comparison between (a) magnetoresistance data in the $(B_{\parallel} - n)$ plane and (b) an extended QMC energy diagram. From Ref. [83]

3.3 ESR in the dilute regime

The transport measurements presented in the previous sections are supplemented by electron spin resonance (ESR) experiments for further characterization of the ultra-dilute 2DES. Due to the high sensitivity of the resistance to minute changes in temperature, the electrical detection of ESR (EDESr) is extremely facile despite the low number of spins in the system. Here we employ this method by applying continuous radiation of fixed frequency while the DC magnetic field is swept slowly (typical sweeping rates are in the range 0.5–5 mT/min); the resonance signal is then detected as a change in the DC voltage and the DC current. To avoid overheating the sample, low radiation power was used. The output power was adjusted for each value of the frequency individually and varied between 1 μ W and 10 mW.

Figure 3.28 shows an EDESr trace for $n = 1.49 \times 10^{10} \text{ cm}^{-2}$. The magnetic field pointed in the plane of the 2DES and the frequency was $f_{\text{MW}} = 12.2 \text{ GHz}$. Two resonances could be resolved: a sharp peak at $B_{\parallel} \approx 0.445 \text{ mT}$ with a full width at half maximum (FWHM) of 0.2 mT and a weaker, broader one at $B_{\parallel} \approx 0.435$, with FWHM = 2 mT. The line shape of the sharp peak is best described by a Lorentzian, while the broad peak can be fitted well with a Gaussian.

In the inset of Fig. 3.28 we plot the resonance field of the two peaks at a set of frequencies. Triangles and circles correspond to the sharp and the broad peak, respectively. To eliminate the error stemming from a zero-field offset due to remnant flux in the superconducting coil we measured the resonance field both in negative and positive field. Unfortunately, this method does not remove errors due to anomalous hysteretic behaviour, the size of which varies with magnetic field. From the hysteresis observed in SdHO in the same measurement conditions we estimate that this error does not exceed 18 mT for magnetic fields larger than 0.14 T. Fitting

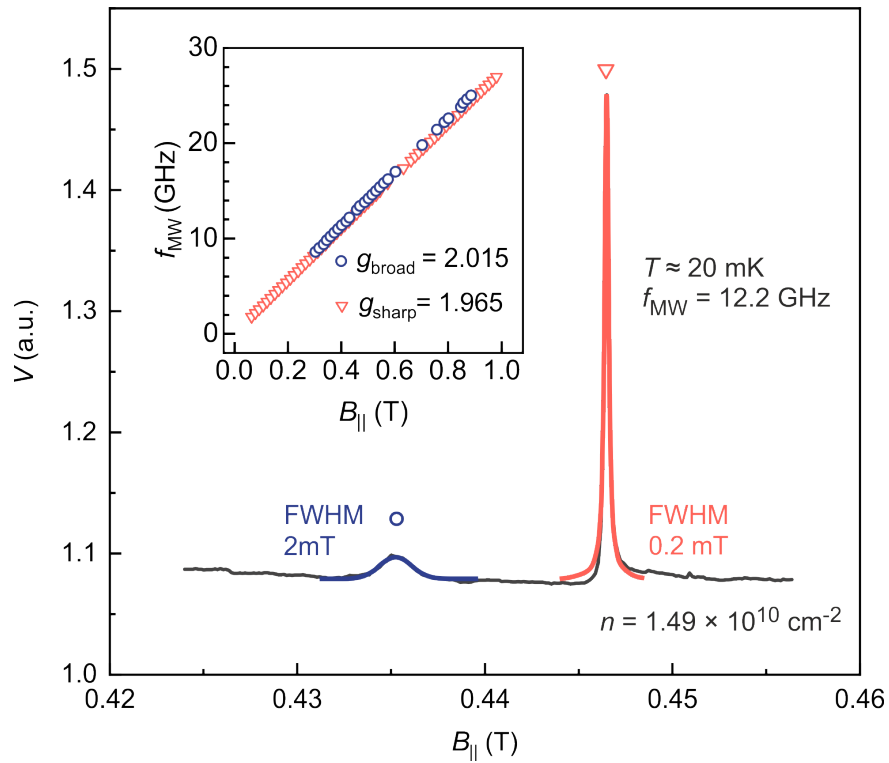


Figure 3.28: EDSR trace for $f_{MW} = 12.2$ GHz. the charge density was $n = 1.49 \times 10^{10}$ cm $^{-2}$ and $T \approx 20$ mK. The green and the red lines represent Gaussian and Lorentzian fits, respectively. Inset: resonance field against microwave frequency for the two resonance peaks. Using a linear regression with zero intercept for each data set, we obtain $g_{broad} = 2.015$ and $g_{sharp} = 1.965$.

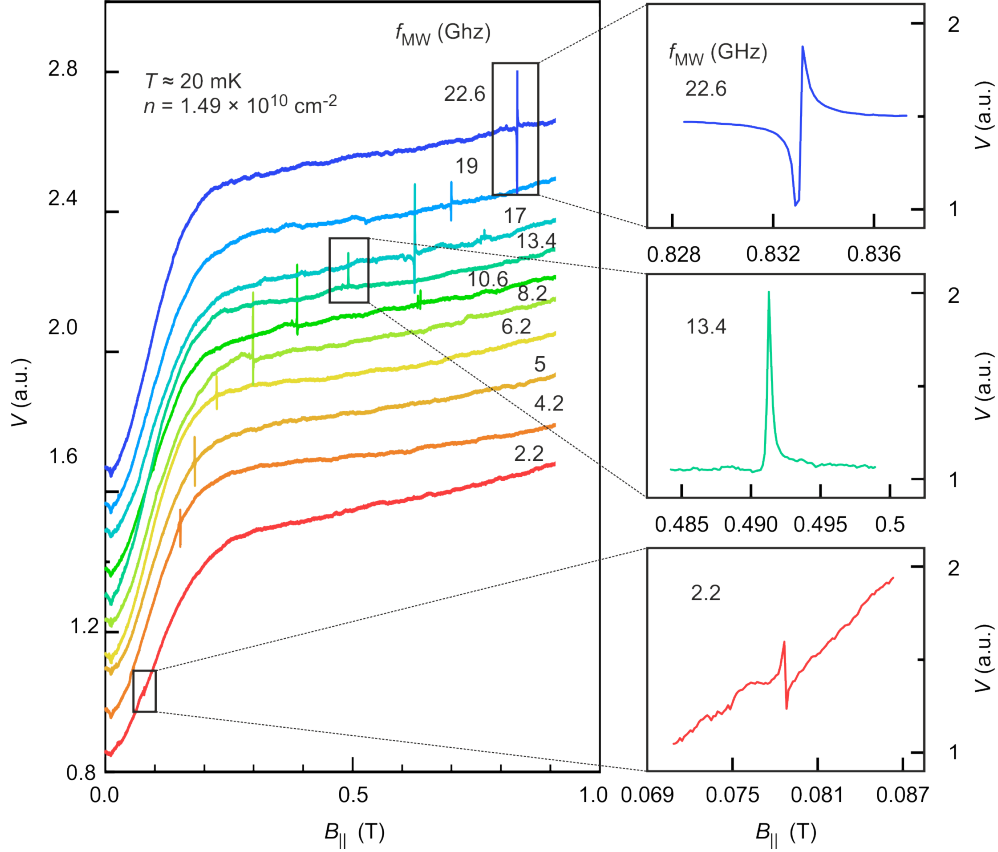


Figure 3.29: EDESr traces for a set of different frequencies, as marked. The electron density was $n = 1.49 \times 10^{10} \text{ cm}^{-2}$ and $T \approx 20 \text{ mK}$. The line shape of the sharp peak evolves gradually with in-plane field.

the two data sets in the inset of Fig. 3.28 using the equation $g\mu_B B = hf_{\text{MW}}$ we obtain $g_{\text{broad}} = 2.015 \pm 0.001$ and $g_{\text{sharp}} = 1.965 \pm 0.0004$.

Judging by its g -value and intensity we can confidently associate the sharp ESR signal to conduction band electrons in pristine ZnO. Since the 2DES resides at the interface between ZnO and $\text{Mg}_x\text{Zn}_{1-x}\text{O}$, it is important to consider the effect of Mg in the cap layer. According to Ref. [173], increasing the alloy content from $x = 0$ to $x = 0.05$ corresponds to an increase in the g -factor from 1.9556 to 1.9593. In our dilute samples the alloy content is less than 1% and therefore we expect a negligible effect on the measured g -factor. Upon rotating the sample from parallel-to perpendicular-field configuration, the position of the sharp resonance changes less than its line width, suggesting very small anisotropy of the g -factor. The origin of the second broader peak is more enigmatic. To our knowledge, this is the first report of a double peak ESR signal in ZnO-based 2DES. Although we have not come to a conclusion on its origin, we explore a few possible explanations.

- Let us assume that this second peak is characteristic only to the ultra-low density 2DES. Two main features stand out in this system: strong inter-electron correlations and the reduced Mg content in the cap layer, which leads to an increased width of the 2DES wavelength. We know that the g -factor extracted from ESR is not sensitive to interactions [169], therefore we do not expect a

renormalized value of g from these measurements. As we have already argued above, the small content of Mg in the cap layer may have only a negligible effect on the g -factor value. Thus even if the system were pressed into the cap layer, the change in the g -factor would be much smaller than the observed change of 2.5%. The assumption that the second peak is present only in low density samples should therefore be reassessed.

- A finite number of nuclear spins are present due to a 4% natural abundance of ^{67}Zn isotopes with spin 5/2. If nuclear spins are polarized (through dynamic nuclear spin polarization), the local effective field experienced by electrons would be larger. This would lead to a shift of the resonance line to lower field, an effect known as the Overhauser shift. The absence of a noticeable hysteresis upon changing sweep direction as well as the insensitivity of the resonance field with temperature makes it unlikely that the broad peak is an effect of dynamic nuclear polarization.
- ESR measurements are highly sensitive to the crystal environment of the paramagnetic spins, thus allowing different types of defects and impurities to be identified in a material. The two most frequent defects in ZnO are the Zn interstitials corresponding to $g_{\text{Zni}} \approx 1.96$ and oxygen vacancies with $g_{\text{Ov}} \approx 1.996$ [224]. The latter is close to the measured g_{broad} . The g -factor of the broad resonance signal may therefore correspond to electrons in the 2D layer which are in the vicinity of oxygen vacancies. Due to the small difference between the zinc interstitials g -factor and the conduction electrons g -factor, it is possible that the two ESR signals cannot be resolved.

The sharp ESR signal displays a systematic line shape change in a parallel magnetic field. Figure 3.29 displays representative traces for different frequencies in the range $f_{\text{MW}} = 2.2 - 22.6$ GHz. The charge carrier density was set to $n = 1.49 \times 10^{10} \text{ cm}^{-2}$ and the temperature was approximately 20 mK. At low frequencies ($f_{\text{MW}} < 11.8$ GHz) the ESR signal displays a derivative-like line shape, with a peak followed by a dip. As the frequency is increased, the amplitude of the dip diminishes until, for $f_{\text{MW}} = 12.2 - 13.4$ GHz the ESR line can be approximated with a Lorentzian function. At even higher frequencies, the signal evolves again into a derivative-like shape, however now the dip precedes the peak. The Lorentzian line shape occurs only in a narrow magnetic field range ($B_{\parallel} = 0.41 - 0.48$ T). The transition in the ESR line cannot be attributed to full spin polarization since the critical field is much lower (for $n = 1.49 \times 10^{10} \text{ cm}^{-2}$, $B_c = 0.12$ T). Moreover the charge carrier density is below $n_c = 1.7 \times 10^{10} \text{ cm}^{-2}$, which excludes effects due to magnetic-field induced MIT. Overall the line shape cannot be explained by heating of the 2DES upon resonant absorption, which would have implied a single dip in the measured DC voltage due to the insulating character at this electron concentration.

The change in line shape from Fig. 3.29 is not present in perpendicular field, where the resonance is characterized by a peak followed by a dip for all frequencies (see Fig. 3.30). This result is surprising as, so far, a strong dependence of the ESR amplitude and line shape on the filling factor has been observed [166, 225]. An essential difference here is that the 2DES becomes fully spin polarized above a relatively small B -field, such that all the spin-down Landau levels are completely

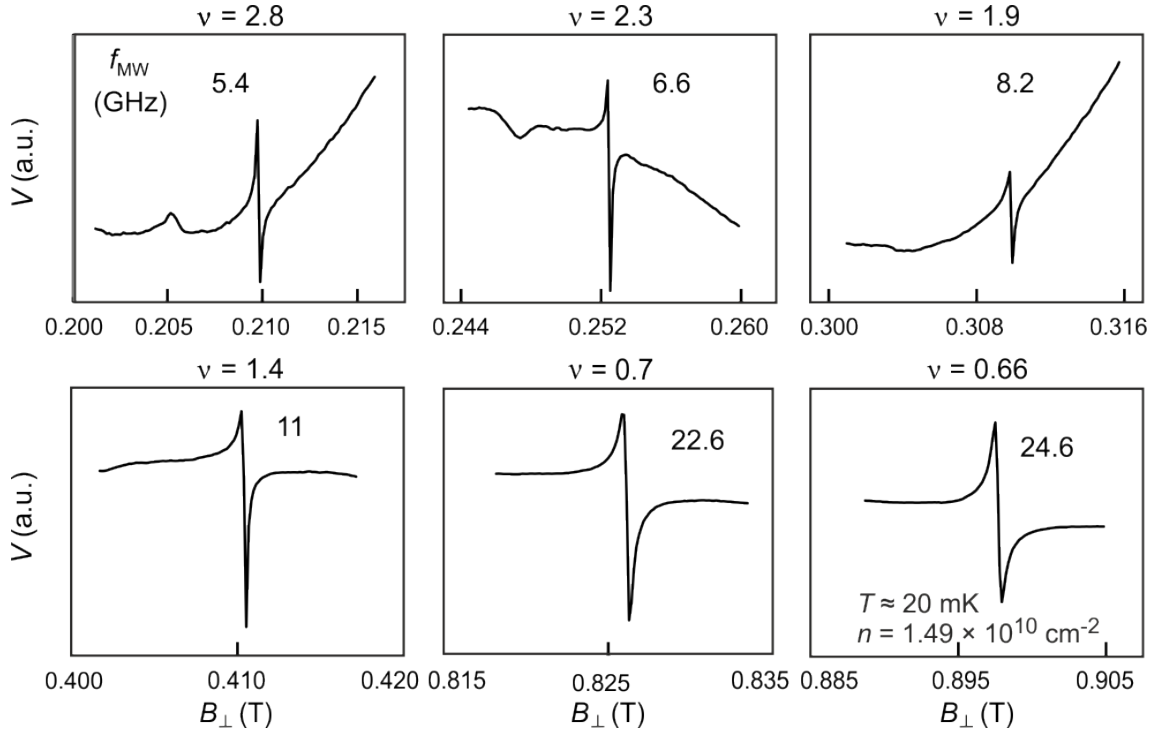


Figure 3.30: EDESr traces measured in a perpendicular field. Each panel corresponds to a different frequency, as marked.

depopulated above B_c . In this regime all the electrons below the Fermi level can contribute to the ESR signal. We were able to detect the sharp ESR peak down to $B_\perp \approx 65$ mT, well below B_c . Here the line shape is similar to the ones presented in Fig. 3.30, thus providing no further insight. With the present measurements it difficult to pinpoint the mechanism which leads to the observed behaviour in the ESR line shape.

Chapter 4

Summary and outlook

The 2DES hosted in high-quality MgZnO/ZnO heterostructures has proven to be a convenient platform for the study of inter-particle correlations. The strength of electron-electron interactions, gauged by the Wigner-Seitz parameter, r_s , is in excess of 3 at all carrier densities n under study. In other words, the Coulomb energy dominates over the kinetic energy of the system, leading to an array of phenomena, the exploration of which presents the scope of this thesis. The experimental results are divided into two parts, constituting the contents of chapters 2 and 3. Here we summarise the main findings and offer a few comments on future directions.

The first part of the thesis concerns 2DESs with a broad electron density range, $2 \times 10^{11} \text{ cm}^{-2} \leq n \leq 20 \times 10^{11} \text{ cm}^{-2}$, which span an interaction parameter interval of $2.6 \leq r_s \leq 8$. The variation of the carrier density was achieved in the growth process by tuning the Mg content in the cap layer. The excellent quality of the structures ensured electron mobilities as high as $\mu = 7 \times 10^5 \text{ cm}^2 \text{ V}^{-1} \text{ s}^{-1}$ and quantum scattering times peaking at $\tau_q \sim 20 \text{ ps}$.

The behaviour of the 2DESs studied in this chapter can be understood within the Fermi-liquid framework. Developed by Landau in 1954, the formalism is based on the premise that the low-lying excited states of an interacting system can be constructed from the excited states close to the Fermi surface of the free system. This approach explains why, on one hand, some of the properties of the non-interacting system, such as a well-defined Fermi surface, stay the same when correlations are switched on. On the other hand, the theory correctly predicts that so-called quasi-particles of the interacting system display a series of modified properties. Two such examples are the quasi-electron effective mass and g -factor, whose values can vary greatly from those of the bare electron.

In the first part of chapter 2 we aimed to explore the many-body effects on the electron effective mass by studying the 2DES response to microwaves with frequencies $f_{\text{MW}} \leq 170 \text{ GHz}$ in the presence of a perpendicular static magnetic field [226]. Transmission measurements were carried out using home-made bolometers for four heterostructures of different n , covering the entire range of electron densities under study. The transmission signal presented a single spectral line which we identified as the cyclotron resonance. From the resonant B -field at high microwave frequencies we extracted the effective mass, whose value was close to the band mass in bulk ZnO [62], $m \approx 0.3m_0$, and varied little with charge carrier density. This result showed that Kohn's theorem [89], which predicts the insensitivity of the CR energy to inter-

actions, applies to the 2DESs in our heterostructures. At low microwave frequencies where the half-wavelength becomes comparable to the size of the sample, $f_{\text{MW}}(B_{\text{res}})$ presented deviations from the linear resonance law. Using a simple model based on the hybridization of the CR with plasma oscillations, we were able to describe the deviation with precision.

The CR mass obtained from transmission was used as reference for the interaction-renormalized mass. We aimed to obtain the latter by analysing the period of microwave-induced resistance oscillations (MIRO). This method was inspired by recent evidence that MIRO probes the many-body mass in GaAs-based 2DESs [100, 101, 142]. Preliminary results in ZnO heterostructures supported this premise [144]. MIRO was successfully detected in 10 samples with electron densities $n \geq 3.5 \times 10^{11} \text{ cm}^{-2}$. At $n > 14 \times 10^{11} \text{ cm}^{-2}$ a reduction in the MIRO mass with respect to the bare mass was found. A systematic increase in m_{MIRO}^* followed at lower n . Both the reduction and the increase qualitatively mirror the renormalized mass obtained from temperature dependent measurements of SdHO, reported elsewhere [121]. Estimating the many-body mass from MIRO poses some advantages over temperature dependent transport measurements: if sufficient oscillations are visible, m_{MIRO}^* can be obtained from a single photoresistance trace with excellent accuracy.

Current theories of MIRO do not accommodate the role on correlations explicitly. Nonetheless, the renormalized mass obtained from MIRO can be intuitively understood as follows: unlike the CR which concerns electron-hole pairs with wave numbers $k \rightarrow 0$, MIRO involves the scattering of quasi-particles at the Fermi surface. This allows a large separation between the electron and the hole, which corresponds to the opposite limit of $k \rightarrow \infty$. Therefore the excitations involved are similar in nature with those contributing to transport. It would indeed be interesting to formulate a theory of MIRO which gauges the effect of interactions on its period.

MIRO was not observed in all samples under study. At low electron densities, $n < 3.5 \times 10^{11} \text{ cm}^{-2}$, the photoresistance was dominated by a different response, namely the bolometric effect of the 2DES at the CR. Concomitant transmission measurements support this interpretation. We attempted to explain the radically different response in low and high density samples by considering the sensitivity of R to a change in temperature in each regime. While this may account for the absence of the bolometric effect at high n , it does not clarify why no MIRO features could be seen at low n . We speculate that it is due to a reduced contribution from the displacement mechanism of MIRO. To determine whether that is indeed the case require further temperature dependent measurements of the amplitude of MIRO.

In view of the results obtained in Ref. [227] for a strongly interacting AlAs-based 2DES, we propose similar experiments in ZnO. The authors report polarization-dependent measurements of the effective mass. By controlling the angle between B and the plane defined by the 2DES, the authors selectively increase the ratio between the Zeeman and the cyclotron energy. At sufficiently large angles, the system is driven into a ferromagnetic state, where only spin-up states are occupied. The effective mass is obtained from the temperature-dependent analysis of SdHO and compared to the value extracted in the paramagnetic state. This provided an interesting result: the effective mass in the fully spin polarized state was close to the bare mass of the system; in the paramagnetic state the mass was greatly enhanced. Such polarization dependent measurements employed in ZnO may shed light on the

absence of a fully spin polarized state at ultra-low densities [83].

The second part of chapter 2 concerns electron spin resonance (ESR) measurements in a sample with $n = 5.3 \times 10^{11} \text{ cm}^{-2}$. Similar to the results in ZnO and AlAs from Ref. [166] we report an interesting alternation between peaks and dips around odd and even filling factors, respectively. Conventionally, electrically detected ESR is associated with an increase in the electron temperature, which would result in a positive contribution to R_{xx} in a quantum Hall minimum. Therefore a reduction in R_{xx} at the paramagnetic resonance in the vicinity of even filling challenges that assumption. The mere existence of an ESR signal at even ν is intriguing: no spin-flip excitations are possible in a fully occupied LL. Previously, the finite polarization at even filling was described as an interaction-induced effect [178]. Although correlations have no impact on the energy probed by ESR, they can modify the Zeeman and cyclotron gap through the renormalized parameters g^* and m^* , as observed in numerous transport experiments [228]. This can have an effect on the amplitude of ESR, as demonstrated in [176]. Similarly, interactions may also modify the energy of the cyclotron spin-flip excitations required to polarize the 2DES at even filling, as indicated in Ref. [179]. While we cannot exclude the effect of level mixing, we argue that it is more likely originating from thermally activated carriers. We attempt to address the ESR amplitude sign by considering a non-equilibrium shift of the spin-up and spin-down chemical potential. The contribution to longitudinal resistance due to such a shift agrees well with the experimental observations. However the model does not account for the heating of the 2DES, which always has a positive contribution to R_{xx} at integer filling. Rotation-dependent measurements as the ones described above may hold the key to a deeper understanding of the ESR amplitude.

The third chapter of this thesis presents the results of a collaborative project on a ZnO heterostructure with ultra-low electron density. The device had a back gate, which allowed the in-situ variation of the charge carrier density in the range $1 \leq n \leq 2.2 (\times 10^{10} \text{ cm}^{-2})$. Thus we were able to access interaction parameter values as high as $r_s \approx 40$.

Temperature and charge carrier density dependent measurements revealed a breakdown of the metallic regime: below a critical density of $n \approx 1.7 \times 10^{10} \text{ cm}^{-2}$ (corresponding to $r_s \approx 30$), the resistance increased with decreasing temperature. This apparent metal-to-insulator transition has been a topic of intense debate, as its exact origin is unclear. While in low-quality samples it is most likely a result of charge carrier localization due to disorder, in clean and strongly-interacting systems it may be a signature of pinning of a Wigner crystal at impurity sites. To determine the localization mechanism, we have analysed the T dependence of the resistance at several electron densities in the insulating regime. At high temperatures, $T \gtrsim 100 \text{ mK}$, a $\ln(R) \propto T^{-\beta}$ law is found, where β varied between 0.53 and 0.86. A dependency of the type $\propto \exp\{T^{-1}\}$ is typically seen in systems where the metal-to-insulator transition is disorder-induced. A cross-over to a different regime is visible at lower T . Both Mott-like and Efros-Shklovskii (ES) exponential laws fit this regime with comparable accuracy.

Another distinct feature at low electron densities is the strong non-linearity of $I - V$ characteristics. Deep in the insulating regime, threshold electric fields as large as $\approx 3 \text{ V/m}$ were required to switch on the current. A model based on single particle localization required much lower values of the electric field to depin the electrons.

An attempt to address the non-linearity in terms of ES variable range hopping also presented inconsistencies. Finally we turn to the assumption that the finite voltage threshold arises from the pinning of a Wigner crystal. Using the model for weak pinning in charge density waves, a correlation length of the order of $3 \mu\text{m}$ was found.

In a parallel magnetic field the resistance increased sharply and then stayed approximately constant above a certain critical value B_c . This behaviour is due to the less efficient screening of disorder as the density of states is reduced when the system becomes fully spin polarized [125]. Identifying the critical field enabled us to estimate the spin susceptibility $\chi^* = g^*m^*/m_0$, which was overall greatly enhanced with respect to the bare value gm/m_0 . We observed a non-monotonic dependence of χ^* on electron density, unlike the expected divergent behaviour associated with a Stoner instability. Moreover, the critical field remains finite down to the lowest accessible n , thus excluding a spontaneous transition to a fully spin polarized state.

The initial roadmap was to supplement the transport measurements published in Ref. [83] with a microwave response study. The conventional bolometric effect due to enhanced absorption at the cyclotron resonance was absent from the photoresponse and so was MIRO. However, we were able to detect strong ESR signals, which consisted of two spectral lines of remarkably different amplitudes. We speculate that the weaker peak is due to electrons in the 2DES in the vicinity of oxygen vacancies. Rotation-dependent measurements in which the direction of the B -field is varied from perpendicular to parallel orientation with respect to the 2DES plane reveal no significant anisotropy of the g -factor.

Zusammenfassung und Ausblick

Das zweidimensionale Elektronensystem (2DES) in hoch-qualitativen MgZnO/ZnO Heterostrukturen hat sich als gut geeignete Plattform für die Untersuchung von Korrelationen zwischen mehreren Teilchen erwiesen. Die Stärke der Elektron-Elektron-Wechselwirkung wird durch den Wigner-Seitz Parameter, r_s , bestimmt. Dessen Wert beträgt über 3 für alle Ladungsträgerdichten, die in dieser Arbeit untersucht werden. Mit anderen Worten, die Coulomb Energie ist stets deutlich größer als die kinetische Energie des Systems, was zu einer Reihe von Phänomenen führt, deren Erforschung den Rahmen dieser Arbeit bildet. Die experimentellen Ergebnisse sind in zwei Teile gegliedert, welche in Kapitel 2 und 3 behandelt werden. Im Folgenden fassen wir die wichtigsten Ergebnisse zusammen und diskutieren mögliche zukünftige Entwicklungen.

Der erste Teil der Arbeit befasst sich mit 2DES mit einem breiten Elektronendichtebereich von $2 \times 10^{11} \text{ cm}^{-2} \leq n \leq 20 \times 10^{11} \text{ cm}^{-2}$, was einem Wigner-Seitz Parameterbereich von $2,6 \leq r_s \leq 8$ entspricht. Die Variation der Ladungsträgerdichte wurde dabei durch Veränderung des Mg-Gehalts in der oberen Deckschicht während des Wachstumsprozesses erzielt. Durch die hervorragende Qualität der Strukturen konnten Elektronenmobilitäten von bis zu $\mu = 7 \times 10^5 \text{ cm}^2 \text{ V}^{-1} \text{ s}^{-1}$ und Quantenstreuungszeiten mit Spitzenwerten von bis zu $\tau_q \sim 20 \text{ ps}$ erreicht werden.

Das Verhalten des in diesem ersten Kapitel untersuchten 2DES kann im theoretischen Rahmenmodell der Fermi-Flüssigkeit verstanden werden. Das im Jahr 1954 von Landau entwickelte Modell basiert auf der Annahme, dass die unteren angeregten Zustände eines wechselwirkenden Systems aus den angeregten Zuständen nahe der Fermi-Fläche des freien Systems konstruiert werden können. Dieser Ansatz erklärt einerseits, warum einige der Eigenschaften des nicht wechselwirkenden Systems, wie z.B. eine wohldefinierte Fermi-Fläche, gleich bleiben, wenn Korrelationen berücksichtigt werden. Andererseits sagt das Modell korrekt voraus, dass die so genannten Quasiteilchen des wechselwirkenden Systems eine Reihe von veränderten Eigenschaften aufweisen. Zwei solcher Beispiele sind die effektive Masse des Quasi-Elektrons und der g -Faktor, deren Werte stark von denen des einzelnen Elektrons ohne Korrelationen abweichen können.

Im ersten Teil von Kapitel 2 untersuchten wir die Vielteilcheneffekte auf die effektive Elektronenmasse, indem wir die Reaktion des 2DES auf Mikrowellen mit Frequenzen $f_{\text{MW}} \leq 170 \text{ GHz}$ in Gegenwart eines senkrechten statischen Magnetfeldes untersuchten [226]. Diese Transmissionsmessungen wurden mit selbstgebauten Bolometern für vier Heterostrukturen mit unterschiedlichen Ladungsträgerdichten, n , durchgeführt, welche den gesamten, weiter oben beschriebenen Elektronendichtebereich abdecken. Das Transmissionssignal zeigte eine einzige Spektrallinie, die wir

als Zyklotronresonanz identifizierten. Aus dem resonanten Magnetfeld, B , bei hohen Mikrowellenfrequenzen extrahierten wir die effektive Masse, deren Wert nahezu der effektiven Masse von ZnO, $m \approx 0,3m_0$ [62], entsprach und nur in geringem Umfang mit der Ladungsträgerdichte variierte. Dieses Ergebnis zeigt, dass das Kohnsche Theorem [89], welches die Unempfindlichkeit der Zyklotronresonanz-Energie gegenüber Wechselwirkungen vorhersagt, auch für das 2DES in unseren Heterostrukturen gilt. Bei niedrigen Mikrowellenfrequenzen, bei denen die Halbwellenlänge mit der Größe der Probe vergleichbar ist, zeigt $f_{\text{MW}}(B_{\text{res}})$ Abweichungen vom linearen Resonanzgesetz. Mithilfe eines einfachen Modells, das auf der Hybridisierung der Zyklotronresonanz (CR) mit Plasmaschwingungen beruht, konnten wir diese Abweichung mit hoher Genauigkeit beschreiben.

Die mittels der Transmissionsmessung bestimmte CR Masse wurde als Referenzwert für die durch Wechselwirkung renormierte Masse genutzt. Unser Ziel war, diese renormierte Masse durch Analyse der Periode der von Mikrowellen induzierten Widerstandsoszillationen (MIRO) zu bestimmen. Diese Methode wurde durch jüngste Erkenntnisse inspiriert, dass sich durch MIRO die Vielteilchenmasse von 2DES in GaAs bestimmen lässt [100, 101, 142]. Erste Ergebnisse in ZnO-Heterostrukturen unterstützen diese Annahme [144]. Von Mikrowellen induzierte Widerstandsoszillationen (MIRO) wurden erfolgreich in 10 Proben mit Elektronendichten von $n \geq 3,5 \times 10^{11} \text{ cm}^{-2}$ nachgewiesen. Bei Elektronendichten von $n > 14 \times 10^{11} \text{ cm}^{-2}$ wurde eine Abnahme der MIRO-Masse im Vergleich zur ursprünglichen Referenz-Masse festgestellt. Eine systematische Zunahme der MIRO-Masse, m_{MIRO}^* , ergab sich dann bei niedrigeren Dichten n . Sowohl die Abnahme als auch die Zunahme spiegeln qualitativ die renormierte Masse wider, welche durch temperaturabhängige Messungen von SdHO bestimmt wurde, über die an anderer Stelle berichtet wurde [121]. Die Abschätzung der Vielteilchenmasse aus MIRO bietet allerdings einige Vorteile gegenüber derartigen temperaturabhängigen Transportmessungen: Wenn genügend Oszillationen sichtbar sind, kann m_{MIRO}^* aus einer einzigen Fotowiderstandsmessung mit sehr hoher Genauigkeit ermittelt werden.

Die derzeitigen Theorien über MIRO berücksichtigen die Rolle der Korrelationen nicht explizit. Nichtsdestotrotz kann die aus MIRO Messungen erhaltene renormierte Masse intuitiv wie folgt verstanden werden: Im Gegensatz zur CR, die Elektron-Loch-Paare mit Wellenzahlen $k \rightarrow 0$ betrifft, geht es bei MIRO um die Streuung von Quasiteilchen an der Fermi-Fläche. Dies ermöglicht einen großen Abstand zwischen dem Elektron und dem Loch, was dem entgegengesetzten Fall von $k \rightarrow \infty$ entspricht. Daher sind die beteiligten Anregungen von ähnlicher Natur wie diejenigen, die zum elektronischen Transport beitragen. Es wäre in der Tat interessant, eine Theorie über MIRO zu formulieren, die die Auswirkungen der Wechselwirkungen auf die MIRO Periode quantitativ genau erfasst.

MIRO wurden nicht in allen untersuchten Proben beobachtet. Bei geringen Elektronendichten, $n < 3,5 \times 10^{11} \text{ cm}^{-2}$, wurde der Fotowiderstand von einem anderen Effekt dominiert, nämlich dem bolometrischen Effekt des 2DES bei der Zyklotronresonanz. Die gleichzeitig durchgeführten Transmissionsmessungen unterstützen diese Interpretation. Wir haben versucht, die fundamental unterschiedliche Reaktion in Proben mit geringer und hoher Dichte zu erklären, indem wir die Empfindlichkeit des Widerstands, R , gegenüber einer Temperaturänderung in jedem Grenzfall betrachteten. Dies kann zwar das Fehlen des bolometrischen Effekts

bei hohen Dichten n erklären, aber es erklärt nicht, warum bei geringen Dichten n keine MIRO-Merkmale zu sehen sind. Wir vermuten, dass dies auf einen geringeren Beitrag des Verschiebungsmechanismus von MIRO zurückzuführen ist. Zur Bestätigung dieser Vermutung sind weitere temperaturabhängige Messungen der MIRO Amplitude erforderlich.

In Anbetracht der Ergebnisse für stark wechselwirkende AlAs-basierte 2DES [227] erwarten wir ähnliche Experimente in ZnO. Die Autoren berichten von spinpolarisations-abhängigen Messungen der effektiven Masse. Durch die Kontrolle des Winkels zwischen B und der Ebene, welche durch das 2DES definiert wird, erhöhen die Autoren gezielt das Verhältnis zwischen der Zeeman- und der Zyklotron-Energie. Bei ausreichend großen Winkeln wird das System in einen ferromagnetischen Zustand überführt, wodurch nur Zustände mit Spin nach oben besetzt sind. Die effektive Masse wird durch die temperatur-abhängige Analyse der SdHO ermittelt und mit dem Wert verglichen, welcher im paramagnetischen Zustand extrahiert wurde. Dies führt zu einem interessanten Ergebnis: Die effektive Masse im vollständig Spin-polarisierten Zustand war nahe an der gewöhnlichen Masse des Systems; im paramagnetischen Zustand war die Masse deutlich größer. Solche polarisations-abhängigen Messungen in ZnO kann Licht auf die Abwesenheit eines vollständig spin-polarisierten Zustands bei einer sehr geringen Dichte werfen [83].

Der zweite Teil von Kapitel 2 befasst sich mit Elektronen-Spin-Resonanz (ESR) Messungen in einer Probe mit $n = 5,3 \times 10^{11} \text{ cm}^{-2}$. Ähnlich zu den Ergebnisse in ZnO und AlAs aus Ref. [166] berichten wir von einer interessanten Abfolge von Hochpunkten und Tiefpunkten in der Nähe von ungeraden und geraden Füllfaktoren. Normalerweise wird elektrisch detektierte ESR mit einer Erwärmung der Elektronen-Temperatur assoziiert, was zu einem positiven Beitrag zu R_{xx} am Quanten-Hall Minimum führen würde. Deshalb stellt eine Reduzierung von R_{xx} bei der paramagnetischen Resonanz in der Umgebung der geraden Füllung diese Annahme in Frage. Die bloße Existenz eines ESR Signals bei geraden ν ist verblüffend: Keine Spin-Wechsel Anregungen sind in einem vollständig gefüllten LL möglich. In der Vergangenheit wurde die endliche Polarisierung bei gerader Füllung als Wechselwirkungs-induzierter Effekt beschrieben [178]. Auch wenn Korrelationen keinen Einfluss auf die Energie haben, welche durch ESR ermittelt wird, können diese die Zeeman und Zyklotron Lücke durch die renormalisierten Parameter g^* und m^* modifizieren bei $q \neq 0$, was in mehreren Transport Experimenten gezeigt wurde [228]. Dies kann wiederum, wie in [176] gezeigt, einen Effekt auf die Amplitude der ESR haben. Ähnlich dazu können Wechselwirkungen, wie gezeigt in Ref. [179], auch die Energie der Zyklotron Spin-Wechsel Anregungen beeinflussen, welche zur Polarisierung des 2DES bei gerader Füllung benötigt wird. Auch wenn wir den Effekt des Niveau-Mischens nicht ausschließen können, gehen wir davon aus, dass es von thermisch aktivierten Ladungsträgern kommt. Wir haben versucht, das Vorzeichen der ESR Amplitude zu untersuchen, indem wir einen Ungleichgewichts-Wechsel der chemischen Potentiale für die beide entgegengesetzt Spinrichtungen betrachten haben. Der Beitrag zu dem longitudinalen Widerstand aufgrund solch eines Wechsels stimmt gut mit experimentellen Beobachtungen überein. Auf der anderen Seite berücksichtigt das Modell das Aufheizen des 2DES nicht, welches immer einen positiven Einfluss auf R_{xx} bei ganzzahligen Füllfaktoren hat. Rotations-abhängige Messungen wie die oben beschriebenen können eine Schlüsselrolle einnehmen für ein tieferes

Verständnis der ESR Amplitude.

Das dritte Kapitel dieser Dissertation beschäftigt sich mit den Ergebnissen eines gemeinsamen Projekts an einer ZnO Heterostruktur mit ultra-niedriger Ladungsträgerdichte. Die Probe besaß ein Rückseitengatter, durch welches die Ladungsträgerdichte in-situ im Bereich $1 \leq n \leq 2,2 (\times 10^{10} \text{ cm}^{-2})$ verändert werden konnte. Somit war es uns möglich, Interaktions-Parameter bis zu einem Wert von $r_s \approx 40$ zu erreichen. Von der Temperatur und Ladungsträgerdichte abhängige Messungen zeigten einen Zusammenbruch des metallischen Regimes: Unterhalb der kritischen Dichte $n \approx 1,7 \times 10^{10} \text{ cm}^{-2}$ (entspricht $r_s \approx 30$) erhöht sich der Widerstand mit abnehmender Temperatur. Dieser scheinbare Metall-Isolator-Übergang ist ein stark diskutiertes Thema, da sein Ursprung unklar ist. Während es in Proben mit niedriger Qualität höchstwahrscheinlich ein Ergebnis der Ladungsträger-Lokalisierung aufgrund von Unordnung ist, kann es in sauberen und stark wechselwirkenden Systemen auf ein Pinning eines Wigner Kristalls an Verunreinigungsstellen hindeuten. Um den Lokalisierungsmechanismus bestimmen zu können, haben wir die Temperaturabhängigkeit des Widerstands bei verschiedenen Ladungsträgerdichten im Isolator-Regime analysiert. Bei hohen Temperaturen, $T \gtrsim 100 \text{ mK}$, wurde ein $\ln(R) \propto T^{-\beta}$ Gesetz gefunden, bei welchem β zwischen 0,53 und 0,86 variierte. Eine Abhängigkeit vom Typ $\propto \exp\{T^{-1}\}$ kann typischerweise in Systemen beobachtet werden, bei welchen der Metall-Isolator-Übergang unordnungs-induziert ist. Ein Übergang zu einem anderen Regime kann bei niedrigeren Temperaturen gesehen werden. Sowohl Mott-ähnliche wie auch Efros-Shklovskii exponentielle Gesetze können dieses Regime mit vergleichbarer Genauigkeit abbilden.

Ein weiteres deutliches Merkmal bei niedrigen Elektronendichten ist die starke Nicht-Linearität der $I - V$ Charakteristik. Tief im Isolator-Regime wurden dreimal stärkere elektrische Felder bis zu einer Stärke von $\approx 3 \text{ V/m}$ benötigt, um die Stromleitung zu ermöglichen. Ein Modell basierend auf Einzel-Partikel-Lokalisierung würde deutlich niedrigere Werte der elektrischen Feldstärke benötigen, um die Elektronen zu lösen. Der Versuch, die Nichtlinearität auch in Bezug auf das Efros-Shklovskii Variablen Range-Hopping zu untersuchen, präsentierte Ungereimtheiten. Schlussendlich kommen wir zu der Annahme, dass der endliche Spannungs-Schwellwert durch das Pinning eines Wigner Kristalls kommt. Mithilfe des Modells für schwaches Pinning in Ladungsdichte-Wellen wurde eine Korrelationslänge von $3 \mu\text{m}$ gefunden.

In Anwesenheit eines parallelen magnetischen Felds steigt der Widerstand scharf an und bleibt dann ungefähr konstant oberhalb eines bestimmten kritischen Wertes B_c . Dieses Verhalten stammt von dem weniger effizienten Abschirmen von Unordnungseffekten während der Reduzierung der Zustandsdichte, wenn das System vollständig Spin-polarisiert wird [125]. Die Identifizierung der kritischen Feldstärke eröffnet uns die Möglichkeit, die Spin-Suszeptibilität $\chi^* = g^*m^*/m_0$ zu bestimmen, welche generell deutlich verstärkt war im Vergleich zu dem regulären Wert gm/m_0 . Wir haben eine nicht-monotone Abhängigkeit zwischen χ und der Elektronendichte festgestellt, welche im Gegensatz zu dem erwarteten divergenten Verhalten steht, welches mit einer Stoner Instabilität einhergeht. Darüber hinaus bleibt die kritische Feldstärke endlich bis hinab zu der niedrigsten möglichen Dichte n , wodurch ein spontaner Übergang zu einem vollständig spin-polarisierten Zustand ausgeschlossen werden kann.

Ursprünglich haben wir geplant, die Transportmessungen, welche in Ref. [83]

publiziert wurden, mit einer Mikrowellenreaktionsstudie zu ergänzen. Der herkömmliche bolometrische Effekt aufgrund verstärkter Absorption bei der Zyklotronresonanz sowie MIRO fehlten in der Fotoantwort. Wir konnten jedoch starke ESR Signale nachweisen, welche aus zwei Spektrallinien mit bemerkenswert unterschiedlichen Amplituden bestanden. Wir nehmen an, dass der schwächere Hochpunkt auf Elektronen im 2DES in der Nähe von Sauerstoffleerstellen zurückzuführen ist. Rotationsabhängige Messungen, bei denen die Richtung des B -Feldes von senkrecht bis parallel zur 2DES-Ebene variiert wird, zeigen keine signifikante Anisotropie des g -Faktors.

Acknowledgements

This work was made possible with great support from the people around me. In particular, I am grateful to...

- Jurgen Smet, who has given me the freedom and support to pursue the projects that I found interesting, and has inspired me to have a well-rounded view of things.
- Joseph Falson, who has spent countless hours teaching me the art of transport and cryogenics, and has always been so supportive. I look up to you, Joe.
- Prof. Klaus von Klitzing, whose enthusiasm for science brought me back on track when things got tough.
- all the Smet group members with whom I had the pleasure to interact. In particular, I am grateful to Dong Zhao, Mingdi Luo and Nils Gross for the long academic and not-so-academic discussions. Big thanks to Steffen Wahl, Gunther Euchner, Sheng Yang, Matthias Kühne, Youngwook Kim, Sanela Göres, Qixing Wang and Fangdong Tang for advice and aid in the lab. I am grateful to Patrick Herlinger, Benedikt Friess, Sven Fecher and Ruth Jenz for helping me navigate through the German labyrinth. My deepest appreciation to Johannes Geurs, who proofread this thesis and has always managed to cheer me up.
- Ivan Dmitriev, Michael Zudov and Sergey Dorozhkin for their input on the MIRO manuscript. Special thanks to Ivan who has offered theoretical support.
- Ksenia Rabinovich and Alexander Boris for the exciting collaboration on CaRuO_3 .
- Thomas Reindl, Marion Hagel, Achim Güth and Yvonne Stuhlhofer for technical support.
- all the wonderful people whom I have met in the Shuttle Smashers badminton group, the Gloss book club and PhD forum. Thank you for filling up my days with joy.
- my friends at home and around the world who have remained just as loyal despite the long distance. In particular, my appreciation to Mădălina Ostafe, Raluca Cohal, Elisabeta Răuță, Irina Ionițe, Diana Gălbinașu and Yuan Miao. You rock!
- my dear family who have offered their unconditional support and have put up with my constant moving around. Thank you for your love.

Bibliography

- [1] D. Pines and P. Nozières, *The Theory of Quantum Liquids: Normal Fermi Liquids*. Cambridge, Massachusetts: Perseus Books Publishing, 1999 ed., 1966.
- [2] E. Dagotto, “Complexity in Strongly Correlated Electronic Systems,” *Science*, vol. 309, pp. 257–262, 2005.
- [3] E. Wigner, “On the interaction of electrons in metals,” *Physical Review*, vol. 46, no. 11, pp. 1002–1011, 1934.
- [4] Z. F. Ezawa, *Quantum Hall effects: Recent theoretical and experimental developments*. Singapore: World Scientific Publishing Co., 2013.
- [5] U. Bockelmann, G. Abstreiter, G. Weimann, and W. Schlapp, “Single-particle and transport scattering times in narrow GaAs/Al_xGa_{1-x}As quantum wells,” *Physical Review B*, vol. 41, no. 11, pp. 7864–7867, 1990.
- [6] L. J. V. D. Pauw, “A method of measuring the resistivity and Hall coefficient on lamellae of arbitrary shape,” *Philips Technical Review*, vol. 20, no. 8, pp. 220–224, 1958.
- [7] J. Weis and K. V. Klitzing, “Metrology and microscopic picture of the integer quantum Hall effect,” *Phil. Trans. R. Soc. A*, vol. 369, pp. 3954–3974, 2011.
- [8] D. B. Chklovskii, B. I. Shklovskii, and L. I. Glazman, “Electrostatics of edge channels,” *Physical Review B*, vol. 46, no. 7, pp. 4026–4034, 1992.
- [9] K. V. Klitzing, G. Dorda, and M. Pepper, “New method for high-accuracy determination of the fine-structure constant based on quantized Hall resistance,” *Physical Review Letters*, vol. 45, no. 6, pp. 494–497, 1980.
- [10] Y. Y. Wei, J. Weis, K. V. Klitzing, and K. Eberl, “Edge strips in the quantum hall regime imaged by a single-electron transistor,” *Physical Review Letters*, vol. 81, no. 8, pp. 1674–1677, 1998.
- [11] E. Ahlswede, P. Weitz, J. Weis, K. Von Klitzing, and K. Eberl, “Hall potential profiles in the quantum Hall regime measured by a scanning force microscope,” *Physica B: Condensed Matter*, vol. 298, pp. 562–566, 2001.
- [12] A. Siddiki and R. R. Gerhardts, “Incompressible strips in dissipative Hall bars as origin of quantized Hall plateaus,” *Physical Review B*, vol. 70, p. 195335, 2004.

- [13] B. Tanatar and D. M. Ceperley, “Ground state of the two-dimensional electron gas,” *Physical Review B*, vol. 39, no. 8, pp. 5005–5016, 1989.
- [14] Y. Kwon, D. M. Ceperley, and R. M. Martin, “Quantum Monte Carlo calculation of the Fermi-liquid parameters in the two-dimensional electron gas,” *Physical Review B*, vol. 50, no. 3, pp. 1684–1694, 1994.
- [15] Y. W. Tan, J. Zhu, H. L. Stormer, L. N. Pfeiffer, K. W. Baldwin, and K. W. West, “Measurements of the density-dependent many-body electron mass in two dimensional GaAs/AlGaAs heterostructures,” *Physical Review Letters*, vol. 94, p. 016405, 2005.
- [16] Y. Zhang and S. Das Sarma, “Density-dependent spin susceptibility and effective mass in interacting quasi-two-dimensional electron systems,” *Physical Review B*, vol. 72, p. 075308, 2005.
- [17] R. Asgari, B. Davoudi, M. Polini, G. F. Giuliani, M. P. Tosi, and G. Vignale, “Quasiparticle self-energy and many-body effective mass enhancement in a two-dimensional electron liquid,” *Physical Review B*, vol. 71, p. 045323, 2005.
- [18] R. Asgari and B. Tanatar, “Many-body effective mass and spin susceptibility in a quasi-two-dimensional electron liquid,” *Physical Review B*, vol. 74, p. 075301, 2006.
- [19] J. Yoon, C. C. Li, D. Shahar, D. C. Tsui, and M. Shayegan, “Wigner crystallization and metal-insulator transition of two-dimensional holes in GaAs at $B = 0$,” *Physical Review Letters*, vol. 82, no. 8, pp. 1744–1747, 1999.
- [20] T. Knighton, Z. Wu, J. Huang, A. Serafin, J. S. Xia, L. N. Pfeiffer, and K. W. West, “Evidence of two-stage melting of Wigner solids,” *Physical Review B*, vol. 97, p. 085135, 2018.
- [21] T. Smoleński, P. E. Dolgirev, C. Kuhlenkamp, A. Popert, Y. Shimazaki, P. Back, X. Lu, M. Kroner, and K. Watanabe, “Signatures of Wigner crystal of electrons in a monolayer semiconductor,” *Nature*, vol. 595, pp. 53–57, 2021.
- [22] S. V. Kravchenko and M. P. Sarachik, “Metal-insulator transition in two-dimensional electron systems,” *Reports on Progress in Physics*, vol. 67, pp. 1–44, 2004.
- [23] B. Spivak and S. A. Kivelson, “Phases intermediate between a two-dimensional electron liquid and Wigner crystal,” *Physical Review B*, vol. 70, p. 155114, 2004.
- [24] C. Attacalite, S. Moroni, P. Gori-Giorgi, and G. B. Bachelet, “Correlation energy and spin polarization in the 2D electron gas,” *Physical Review Letters*, vol. 88, no. 25, p. 2566011, 2002.
- [25] N. D. Drummond and R. J. Needs, “Phase diagram of the low-density two-dimensional homogeneous electron gas,” *Physical Review Letters*, vol. 102, p. 126402, 2009.

- [26] M. S. Hossain, M. K. Ma, K. A. Villegas Rosales, Y. J. Chung, L. N. Pfeiffer, K. W. West, K. W. Baldwin, and M. Shayegan, “Observation of spontaneous ferromagnetism in a two-dimensional electron system,” *Proceedings of the National Academy of Sciences of the United States of America*, vol. 117, no. 51, pp. 32244–32250, 2020.
- [27] G. Giuliani and G. Vignale, *Quantum theory of the electron liquid*. New York: Cambridge University Press, 2005.
- [28] L. Bonsall and A. A. Maradudin, “Some dynamical properties of a two-dimensional Wigner crystal,” *Physical Review B*, vol. 15, no. 4, pp. 1959–1973, 1977.
- [29] R. D. Misra, “On the stability of crystal lattices,” *Mathematical Proceedings of the Cambridge Philosophical Society*, vol. 36, pp. 173–182, 1939.
- [30] A. K. Rajagopal and J. C. Kimball, “Correlations in a two-dimensional electron system,” *Physical Review B*, vol. 15, no. 5, pp. 2819–2825, 1977.
- [31] V. J. Goldman, M. Santos, M. Shayegan, and J. E. Cunningham, “Evidence for two-dimensional quantum Wigner crystal,” *Physical Review Letters*, vol. 65, no. 17, pp. 2189–2192, 1990.
- [32] F. I. Williams, P. A. Wright, R. G. Clark, E. Y. Andrei, G. Deville, D. C. Glatli, O. Probst, B. Etienne, C. Dorin, C. T. Foxon, and J. J. Harris, “Conduction threshold and pinning frequency of magnetically induced Wigner solid,” *Physical Review Letters*, vol. 66, no. 25, pp. 3285–3288, 1991.
- [33] M. A. Paalanen, R. L. Willett, R. R. Ruel, P. B. Littlewood, K. W. West, and L. N. Pfeiffer, “Electrical conductivity and Wigner crystallization,” *Physical Review B*, vol. 45, no. 23, pp. 13784–13787, 1992.
- [34] E. Y. Andrei, G. Deville, D. C. Glatli, F. I. Williams, E. Paris, and B. Etienne, “Observation of a magnetically induced wigner solid,” *Physical Review Letters*, vol. 60, no. 26, pp. 2765–2768, 1988.
- [35] Y. P. Chen, G. Sambandamurthy, Z. H. Wang, R. M. Lewis, L. W. Engel, D. C. Tsui, P. D. Ye, L. N. Pfeiffer, and K. W. West, “Melting of a 2D quantum electron solid in high magnetic field,” *Nature Physics*, vol. 2, pp. 452–455, 2006.
- [36] E. C. Regan, D. Wang, C. Jin, M. I. Bakti Utama, B. Gao, X. Wei, S. Zhao, W. Zhao, Z. Zhang, K. Yumigeta, M. Blei, J. D. Carlström, K. Watanabe, T. Taniguchi, S. Tongay, M. Crommie, A. Zettl, and F. Wang, “Mott and generalized Wigner crystal states in WSe₂/WS₂ moiré superlattices,” *Nature*, vol. 579, no. 7799, pp. 359–363, 2020.
- [37] Y. Zhou, J. Sung, E. Brutschea, I. Esterlis, Y. Wang, G. Scuri, R. J. Gelly, H. Heo, T. Taniguchi, K. Watanabe, G. Zaránd, M. D. Lukin, P. Kim, E. Demler, and H. Park, “Signatures of bilayer Wigner crystals in a transition metal dichalcogenide heterostructure,” *Nature*, vol. 595, pp. 48–52, 2021.

- [38] H. Li, S. Li, E. C. Regan, D. Wang, W. Zhao, S. Kahn, K. Yumigeta, M. Blei, T. Taniguchi, K. Watanabe, S. Tongay, A. Zettl, M. F. Crommie, and F. Wang, “Imaging two-dimensional generalized Wigner crystals,” *Nature*, vol. 597, pp. 650–654, 2021.
- [39] S. R. Hofstein and F. P. Heiman, “The silicon insulated-gate field-effect transistor,” *Proceedings of the IEEE*, vol. 51, pp. 1190–1202, 1963.
- [40] S. V. Kravchenko, G. V. Kravchenko, J. E. Furneaux, M. V. Pudalov, and M. D’Iorio, “Possible metal-insulator transition at $B=0$ in two dimensions,” *Physical Review B*, vol. 50, no. 11, pp. 8038 – 8042, 1994.
- [41] V. M. Pudalov, M. D’Iorio, S. V. Kravchenko, and J. W. Campbell, “Zero-magnetic-field collective insulator phase in a dilute 2D electron system,” *Physical Review Letters*, vol. 70, no. 12, pp. 1866–1869, 1993.
- [42] J. C. Hensel, H. Hasegawa, and M. Nakayama, “Cyclotron resonance in uniaxially stressed silicon. II. Nature of the covalent bond,” *Physical Review*, vol. 138, no. 1 A, p. A225, 1965.
- [43] D. C. Tsui, H. L. Stormer, and A. C. Gossard, “Two-dimensional magneto-transport in the extreme quantum limit,” *Physical Review Letters*, vol. 48, no. 22, pp. 1559–1562, 1982.
- [44] R. Willett, J. P. Eisenstein, H. L. Störmer, D. C. Tsui, A. C. Gossard, and J. H. English, “Observation of an even-denominator quantum number in the fractional quantum Hall effect,” *Physical Review Letters*, vol. 59, no. 15, pp. 1776–1779, 1987.
- [45] W. Pan, J.-S. Xia, V. Shvarts, D. E. Adams, H. L. Stormer, D. C. Tsui, L. N. Pfeiffer, K. W. Baldwin, and K. W. West, “Exact Quantization of the Even-Denominator Fractional Quantum Hall State at $\nu = 5 / 2$ Landau Level Filling Factor,” *Physical Review Letters*, vol. 83, no. 17, pp. 3530–3533, 1999.
- [46] M. Y. Melnikov, A. A. Shashkin, V. T. Dolgoplov, S. H. Huang, C. W. Liu, and S. V. Kravchenko, “Indication of band flattening at the Fermi level in a strongly correlated electron system,” *Scientific Reports*, vol. 7, p. 14539, 2017.
- [47] M. Y. Melnikov, A. A. Shashkin, V. T. Dolgoplov, A. Y. Zhu, S. V. Kravchenko, S. H. Huang, and C. W. Liu, “Quantum phase transition in ultrahigh mobility SiGe/Si/SiGe two-dimensional electron system,” *Physical Review B*, vol. 99, p. 081106(R), 2019.
- [48] A. V. Shchepetilnikov, A. R. Khisameeva, Y. A. Nefyodov, I. V. Kukushkin, L. Tiemann, C. Reichl, W. Dietsche, and W. Wegscheider, “Spin-orbit interaction in AlAs quantum wells,” *Physica E: Low-Dimensional Systems and Nanostructures*, vol. 124, p. 114278, 2020.
- [49] S. Shankar, A. M. Tyryshkin, S. Avasthi, and S. A. Lyon, “Spin resonance of 2D electrons in a large-area silicon MOSFET,” *Physica E: Low-Dimensional Systems and Nanostructures*, vol. 40, pp. 1659–1661, 2008.

- [50] M. Y. Melnikov, A. A. Shashkin, V. T. Dolgoplov, S. H. Huang, C. W. Liu, and S. V. Kravchenko, “Ultra-high mobility two-dimensional electron gas in a SiGe/Si/SiGe quantum well,” *Applied Physics Letters*, vol. 106, p. 092102, 2015.
- [51] Y. J. Chung, K. A. Villegas Rosales, K. W. Baldwin, P. T. Madathil, K. W. West, M. Shayegan, and L. N. Pfeiffer, “Ultra-high-quality two-dimensional electron systems,” *Nature Materials*, vol. 20, no. 5, pp. 632–637, 2021.
- [52] M. Cardona, “Electron effective masses of InAs and GaAs as a function of temperature and doping,” *Physical Review*, vol. 121, no. 3, pp. 752–758, 1961.
- [53] M. J. Snelling, G. P. Flinn, A. S. Plaut, R. T. Harley, A. C. Tropper, R. Eccleston, and C. C. Phillips, “Magnetic g-factor of electrons in GaAs/Al_xGa_{1-x}As quantum wells,” *Physical Review B*, vol. 44, no. 20, pp. 11345–11352, 1991.
- [54] M. J. Manfra, E. H. Hwang, S. Das Sarma, L. N. Pfeiffer, K. W. West, and A. M. Sergent, “Transport and percolation in a low-density high-mobility two-dimensional hole system,” *Physical Review Letters*, vol. 99, no. 23, p. 236402, 2007.
- [55] H. L. Stormer, Z. Schlesinger, A. Chang, D. C. Tsui, A. C. Gossard, and W. Wiegmann, “Energy structure and quantized hall effect of two-dimensional holes,” *Physical Review Letters*, vol. 51, no. 2, pp. 126–129, 1983.
- [56] Y. J. Chung, K. A. Villegas Rosales, H. Deng, K. W. Baldwin, K. W. West, M. Shayegan, and L. N. Pfeiffer, “Multivalley two-dimensional electron system in an AlAs quantum well with mobility exceeding $2 \times 10^6 \text{ cm}^2 \text{ V}^{-1} \text{ s}^{-1}$,” *Physical Review Materials*, vol. 2, no. 7, pp. 1–6, 2018.
- [57] M. Shayegan, E. P. De Poortere, O. Gunawan, Y. P. Shkolnikov, E. Tutuc, and K. Vakili, “Two-dimensional electrons occupying multiple valleys in AlAs,” *Physica Status Solidi (B) Basic Research*, vol. 243, pp. 3629–3642, nov 2006.
- [58] S. Syed, M. J. Manfra, Y. J. Wang, R. J. Molnar, and H. L. Stormer, “Electron scattering in AlGa_N/Ga_N structures,” *Applied Physics Letters*, vol. 84, pp. 1507–1509, 2004.
- [59] W. Knap, H. Alause, J. M. Bluet, J. Camassel, J. Young, M. Asif Khan, Q. Chen, S. Huant, and M. Shur, “The cyclotron resonance effective mass of two-dimensional electrons confined at the Ga_N/AlGa_N interface,” *Solid State Communications*, vol. 99, no. 3, pp. 195–199, 1996.
- [60] A. Wolos, Z. Wilamowski, C. Skierbiszewski, A. Drabinska, B. Lucznik, I. Grzegory, and S. Porowski, “Electron spin resonance and Rashba field in Ga_N-based materials,” *Physica B: Condensed Matter*, vol. 406, pp. 2548–2554, jul 2011.
- [61] J. Falson, Y. Kozuka, M. Uchida, J. H. Smet, T.-h. Arima, A. Tsukazaki, and M. Kawasaki, “MgZnO/ZnO heterostructures with electron mobility exceeding $1 \times 10^6 \text{ cm}^2/\text{Vs}$,” *Scientific Reports*, vol. 6, p. 26598, 2016.

- [62] K. J. Button, D. R. Cohn, M. von Ortenbert, B. Lax, E. Mollwo, and R. Helbig, “Zeeman Splitting of Anomalous Shallow Bound States in ZnO,” *Physical Review Letters*, vol. 28, no. 25, pp. 1637–1639, 1972.
- [63] D. Reiser, J. Bloemker, G. Denninger, and J. Schneider, “A magnetic double-resonance investigation of the quadrupole interaction in ZnO single crystals,” *Solid State Communications*, vol. 102, no. 5, pp. 359–363, 1997.
- [64] H. W. Van Kesteren, E. C. Cosman, W. A. Van Der Poel, and C. T. Foxon, “Fine structure of excitons in type-II GaAs/AlAs quantum wells,” *Physical Review B*, vol. 41, no. 8, pp. 5283–5292, 1990.
- [65] X. Marie, T. Amand, P. L. Jeune, M. Paillard, P. Renucci, L. E. Golub, V. D. Dymnikov, and E. L. Ivchenko, “Hole spin quantum beats in quantum-well structures,” *Physical Review B*, vol. 60, no. 8, pp. 5811–5817, 1999.
- [66] M. Syperek, D. R. Yakovlev, A. Grelich, J. Misiewicz, M. Bayer, D. Reuter, and A. D. Wieck, “Spin coherence of holes in GaAs/(Al,Ga)As quantum wells,” *Physical Review Letters*, vol. 99, no. 18, pp. 5–8, 2007.
- [67] V. F. Sapega, M. Cardona, K. Ploog, E. L. Ivchenko, and D. N. Mirlin, “Spin-flip Raman scattering in GaAs/Al_xGa_{1-x}As multiple quantum wells,” *Physical Review B*, vol. 45, no. 8, pp. 4320–4326, 1992.
- [68] M. A. Khan, J. N. Kuznia, J. M. Van Hove, N. Pan, and J. Carter, “Observation of a two-dimensional electron gas in low pressure metalorganic chemical vapor deposited GaN/Al_xGa_{1-x}N heterojunctions,” *Applied Physics Letters*, vol. 60, pp. 3027–3029, 1992.
- [69] A. H. Castro Neto, F. Guinea, N. M. Peres, K. S. Novoselov, and A. K. Geim, “The electronic properties of graphene,” *Reviews of Modern Physics*, vol. 81, pp. 109–162, 2009.
- [70] K. S. Novoselov, V. I. Fal’ko, L. Colombo, P. R. Gellert, M. G. Schwab, and K. Kim, “A roadmap for graphene,” *Nature*, vol. 490, no. 7419, pp. 192–200, 2012.
- [71] K. S. Novoselov, A. K. Geim, S. V. Morozov, D. Jiang, Y. Zhang, S. V. Dubonos, I. Grigorieva, and A. A. Firsov, “Electric Field Effect in Atomically Thin Carbon Films,” *Science*, vol. 306, pp. 666–669, 2004.
- [72] N. Mounet, M. Gibertini, P. Schwaller, D. Campi, A. Merkys, A. Marrazzo, T. Sohier, I. E. Castelli, A. Cepellotti, G. Pizzi, and N. Marzari, “Two-dimensional materials from high-throughput computational exfoliation of experimentally known compounds,” *Nature Nanotechnology*, vol. 13, no. 3, pp. 246–252, 2018.
- [73] https://commons.wikimedia.org/wiki/File:Wurtzite_polyhedra.png, “Wurtzite polyhedra.”

- [74] A. Ohtomo, M. Kawasaki, T. Koida, K. Masubuchi, H. Koinuma, Y. Sakurai, Y. Yoshida, T. Yasuda, and Y. Segawa, “MgZnO as a II – VI widegap semiconductor alloy,” *Appl. Phys. Lett.*, vol. 72, p. 2466, 1998.
- [75] Y. Kozuka, A. Tsukazaki, and M. Kawasaki, “Challenges and opportunities of ZnO-related single crystalline heterostructures,” *Applied Physics Reviews*, vol. 1, p. 011303, 2014.
- [76] Ü. Özgür, Y. I. Alivov, C. Liu, A. Teke, M. A. Reshchikov, S. Doğan, V. Avrutin, S. J. Cho, and H. Morkoç, “A comprehensive review of ZnO materials and devices,” *Journal of Applied Physics*, vol. 98, p. 041301, 2005.
- [77] J. Falson, *Transport phenomena and correlation effects in MgZnO/ZnO interface confined high mobility two-dimensional electron systems*. PhD thesis, University of Tokyo, 2015.
- [78] H. Tampo, H. Shibata, K. Maejima, A. Yamada, K. Matsubara, P. Fons, S. Kashiwaya, S. Niki, Y. Chiba, T. Wakamatsu, and H. Kanie, “Polarization-induced two-dimensional electron gases in ZnMgO/ZnO heterostructures,” *Applied Physics Letters*, vol. 93, no. 20, 2008.
- [79] J. Falson, D. Maryenko, Y. Kozuka, A. Tsukazaki, and M. Kawasaki, “Magnesium doping controlled density and mobility of two-dimensional electron gas in MgZnO/ZnO heterostructures,” *Applied Physics Express*, vol. 4, p. 91101, 2011.
- [80] V. V. Solovyev, A. B. Van’kov, I. V. Kukushkin, J. Falson, D. Zhang, D. Maryenko, Y. Kozuka, A. Tsukazaki, J. H. Smet, and M. Kawasaki, “Optical probing of MgZnO/ZnO heterointerface confinement potential energy levels,” *Applied Physics Letters*, vol. 106, p. 082102, 2015.
- [81] J. Falson, D. Maryenko, B. Friess, D. Zhang, Y. Kozuka, A. Tsukazaki, and J. H. Smet, “Even-denominator fractional quantum Hall physics in ZnO,” *Nat. Phys.*, vol. 6, p. 347, 2015.
- [82] J. Falson, D. Tabrea, D. Zhang, I. Sodemann, Y. Kozuka, A. Tsukazaki, M. Kawasaki, K. Von Klitzing, and J. Smet, “A cascade of phase transitions in an orbitally mixed half-filled Landau level,” *Science Advances*, vol. 4, no. 9, 2018.
- [83] J. Falson, I. Sodemann, B. Skinner, D. Tabrea, Y. Kozuka, A. Tsukazaki, M. Kawasaki, K. von Klitzing, and J. H. Smet, “Competing correlated states around the zero field Wigner crystallization transition of electrons in two-dimensions,” *Nature Materials*, vol. 21, pp. 311–316, 2021.
- [84] W. Knap, H. Alause, J. M. Bluett, J. Camassel, J. Young, M. Asif Khan, Q. Chen, S. Huan, and M. Shur, “The cyclotron resonance effective mass of two-dimensional electrons confined at the GaN/AlGaN interface,” *Solid State Communications*, vol. 99, no. 3, pp. 195–199, 1996.

- [85] T. Ando, "Theory of Cyclotron Resonance Lineshape in a Two-Dimensional Electron System," *Journal of the Physical Society of Japan*, vol. 38, no. 4, pp. 989–997, 1975.
- [86] G. Abstreiter, J. P. Kotthaus, J. F. Koch, and G. Dorda, "Cyclotron resonance of electrons in surface space-charge layers on silicon," *Physical Review B*, vol. 14, no. 6, p. 2480, 1976.
- [87] T. Ando, "Theory of magnetoplasmon resonance lineshape in the silicon inversion layer," *Solid State Communications*, vol. 27, no. 9, pp. 895–899, 1978.
- [88] E. Vasiliadou, G. Muller, D. Heitmann, D. Weiss, and K. Klitzing, "Collective response in the microwave photoconductivity of Hall bar structures," *Phys. Rev. B*, vol. 48, no. 23, p. 17145, 1993.
- [89] W. Kohn, "Cyclotron resonance and de Haas-van Alphen oscillations of an interacting electron gas," *Physical Review*, vol. 123, no. 4, pp. 1242–1244, 1961.
- [90] I. A. Dmitriev, A. D. Mirlin, D. G. Polyakov, and M. A. Zudov, "Nonequilibrium phenomena in high Landau levels," *Reviews of Modern Physics*, vol. 84, no. 4, p. 1709, 2012.
- [91] R. G. Mani, J. H. Smet, K. Von Klitzing, V. Narayanamurti, W. B. Johnson, and V. Umansky, "Demonstration of a $1/4$ -cycle phase shift in the radiation-induced oscillatory magnetoresistance in GaAs/AlGaAs devices," *Physical Review Letters*, vol. 92, p. 146801, 2004.
- [92] A. C. Durst, S. Sachdev, N. Read, and S. M. Girvin, "Radiation-Induced Magnetoresistance Oscillations in a 2D Electron Gas," *Physical Review Letters*, vol. 91, p. 086803, jan 2003.
- [93] M. G. Vavilov and T. L. Aleiner, "Magnetotransport in a two-dimensional electron gas at large filling factors," *Physical Review B*, vol. 69, p. 035303, 2004.
- [94] I. A. Dmitriev, A. D. Mirlin, and D. G. Polyakov, "Microwave photoconductivity of a two-dimensional electron gas: Mechanisms and their interplay at high radiation power," *Physical Review B*, vol. 75, p. 245320, 2007.
- [95] M. Khodas and M. G. Vavilov, "Effect of microwave radiation on the nonlinear resistivity of a two-dimensional electron gas at large filling factors," *Physical Review B*, vol. 78, p. 245319, 2008.
- [96] I. A. Dmitriev, M. Khodas, A. D. Mirlin, D. G. Polyakov, and M. G. Vavilov, "Mechanisms of the microwave photoconductivity in two-dimensional electron systems with mixed disorder," *Physical Review B*, vol. 80, p. 165327, 2009.
- [97] I. A. Dmitriev, A. D. Mirlin, and D. G. Polyakov, "Cyclotron-resonance harmonics in the ac response of a 2d electron gas with smooth disorder," *Physical Review Letters*, vol. 91, no. 22, p. 226802, 2003.

- [98] I. A. Dmitriev, M. G. Vavilov, I. L. Aleiner, A. D. Mirlin, and D. G. Polyakov, “Theory of microwave-induced oscillations in the magnetoconductivity of a two-dimensional electron gas,” *Physical Review B*, vol. 71, p. 115316, 2005.
- [99] J. H. Smet, B. Gorshunov, C. Jiang, L. Pfeiffer, K. West, V. Umankysy, M. Dressel, R. Meisels, F. Kuchar, and K. Von Klitzing, “Circular-polarization-dependent study of the microwave photoconductivity in a two-dimensional electron system,” *Physical Review Letters*, vol. 95, p. 116804, 2005.
- [100] A. T. Hatke, M. A. Zudov, J. D. Watson, M. J. Manfra, L. N. Pfeiffer, and K. W. West, “Evidence for effective mass reduction in GaAs/AlGaAs quantum wells,” *Physical Review B*, vol. 87, p. 161307(R), 2013.
- [101] A. V. Shchepetilnikov, D. D. Frolov, Y. A. Nefyodov, I. V. Kukushkin, and S. Schmult, “Renormalization of the effective mass deduced from the period of microwave-induced resistance oscillations in GaAs/AlGaAs heterostructures,” *Physical Review B*, vol. 95, p. 161305(R), 2017.
- [102] X. L. Lei and S. Y. Liu, “Radiation-induced magnetoresistance oscillation in a two-dimensional electron gas in Faraday geometry,” *Physical Review Letters*, vol. 91, p. 226805, 2003.
- [103] J. Shi and X. C. Xie, “Radiation-Induced “Zero-Resistance State” and the Photon-Assisted Transport,” *Physical Review Letters*, vol. 91, no. 8, p. 086801, 2003.
- [104] Y. M. Beltukov and M. I. Dyakonov, “Microwave-Induced Resistance Oscillations as a Classical Memory Effect,” *Physical Review Letters*, vol. 116, p. 176801, 2016.
- [105] A. D. Chepelianskii and D. L. Shepelyansky, “Microwave stabilization of edge transport and zero-resistance states,” *Physical Review B*, vol. 80, no. 24, p. 241308(R), 2009.
- [106] S. A. Mikhailov and N. A. Savostianova, “Influence of contacts on the microwave response of a two-dimensional electron stripe,” *Physical Review B*, vol. 74, p. 045325, 2006.
- [107] S. A. Mikhailov, “Theory of microwave-induced zero-resistance states in two-dimensional electron systems,” *Physical Review B*, vol. 83, p. 155303, 2011.
- [108] C. L. Yang, M. A. Zudov, T. A. Knuuttila, R. R. Du, L. N. Pfeiffer, and K. W. West, “Observation of Microwave-Induced Zero-Conductance State in Corbino Rings of a Two-Dimensional Electron System,” *Physical Review Letters*, vol. 91, p. 096803, 2003.
- [109] A. V. Shchepetilnikov, A. R. Khisameeva, Y. A. Nefyodov, S. Schmult, and I. V. Kukushkin, “Observation of microwave-induced resistance oscillations in a contactless geometry,” *Physical Review B*, vol. 102, p. 075445, 2020.

- [110] B. Friess, I. A. Dmitriev, V. Umansky, L. Pfeiffer, K. West, K. Von Klitzing, and J. H. Smet, “Acoustoelectric Study of Microwave-Induced Current Domains,” *Physical Review Letters*, vol. 124, p. 117601, 2020.
- [111] C. P. Poole, *Electron spin resonance - A comprehensive treatise on experimental techniques*. New York City: John Wiley & Sons, Inc., second ed., 1983.
- [112] R. J. Elliott, “Theory of the effect of spin-Orbit coupling on magnetic resonance in some semiconductors,” *Physical Review*, vol. 96, no. 2, pp. 266–279, 1954.
- [113] M. I. Dyakonov and V. I. Perel, “Current-induced spin orientation of electrons in semiconductors,” *Physics Letters*, vol. 35A, no. 6, pp. 459–460, 1971.
- [114] Y. Yafet, “g Factors and Spin-Lattice Relaxation of Conduction Electrons,” in *Solid State Physics*, vol. 14, pp. 1–98, Academic Press, 1963.
- [115] M. Califano, T. Chakraborty, P. Pietiläinen, and C. M. Hu, “Breaking of Larmor’s theorem in quantum Hall states with spin-orbit coupling,” *Physical Review B*, vol. 73, p. 113315, 2006.
- [116] M. J. Manfra, K. W. Baldwin, A. M. Sergent, R. J. Molnar, and J. Caissie, “Electron mobility in very low density GaN/AlGaN/GaN heterostructures,” *Applied Physics Letters*, vol. 85, no. 10, pp. 1722–1724, 2004.
- [117] A. Gold, “Transport properties of the electron gas in ZnO/MgZnO heterostructures,” *Applied Physics Letters*, vol. 96, p. 242111, 2010.
- [118] J. L. Smith and P. J. Stiles, “Electron-Electron Interactions Continuously Variable in the Range $2.1 > r_s > 0.9^*$,” *Physical Review Letters*, vol. 29, no. 2, pp. 102–104, 1972.
- [119] Y. Kozuka, A. Tsukazaki, D. Maryenko, J. Falson, C. Bell, M. Kim, Y. Hikita, H. Y. Hwang, and M. Kawasaki, “Single-valley quantum Hall ferromagnet in a dilute $\text{Mg}_x\text{Zn}_{1-x}\text{O}/\text{ZnO}$ strongly correlated two-dimensional electron system,” *Physical Review B*, vol. 85, p. 075302, 2012.
- [120] A. Tsukazaki, H. Yuji, S. Akasaka, K. Tamura, K. Nakahara, T. Tanabe, H. Takasu, A. Ohtomo, and M. Kawasaki, “High Electron Mobility Exceeding $10^4 \text{ cm}^2 \text{ V}^{-1} \text{ s}^{-1}$ in $\text{Mg}_x\text{Zn}_{1-x}\text{O}/\text{ZnO}$ Single Heterostructures Grown by Molecular Beam Epitaxy,” *Applied Physics Express*, vol. 1, p. 055004, 2008.
- [121] J. Falson and M. Kawasaki, “A review of the quantum Hall effects in MgZnO/ZnO heterostructures,” *Reports on Progress in Physics*, vol. 81, p. 056501, 2018.
- [122] V. M. Pudalov, M. E. Gershenson, H. Kojima, N. Butch, E. M. Dizhur, G. Brunthaler, A. Prinz, and G. Bauer, “Low-density spin susceptibility and effective mass of mobile electrons in Si inversion layers,” *Physical Review Letters*, vol. 88, no. 19, p. 196404, 2002.

- [123] F. F. Fang and P. J. Stiles, “Effects of a tilted magnetic field on a two-dimensional electron gas,” *Physical Review*, vol. 174, no. 3, pp. 823–828, 1968.
- [124] T. Okamoto, K. Hosoya, S. Kawaji, and A. Yagi, “Spin degree of freedom in a two-dimensional electron liquid,” *Physical Review Letters*, vol. 82, no. 19, pp. 3875–3878, 1999.
- [125] V. T. Dolgoplov and A. Gold, “Magnetoresistance of a two-dimensional electron gas in a parallel magnetic field,” *Journal of Experimental and Theoretical Physics Letters*, vol. 71, no. 1, pp. 27–30, 2000.
- [126] G. Dresselhaus, A. F. Kip, and C. Kittel, “Plasma resonance in crystals: Observations and theory,” *Physical Review*, vol. 100, no. 2, pp. 618–625, 1955.
- [127] M. A. Hopkins, R. J. Nicholas, M. A. Brummell, J. J. Harris, and C. T. Foxon, “Cyclotron-resonance study of nonparabolicity and screening in GaAs-GaAlAs heterojunctions,” *Physical Review B*, vol. 36, no. 9, pp. 4789–4795, 1987.
- [128] A. H. MacDonald and C. Kallin, “Cyclotron resonance in two dimensions: Electron-electron interactions and band nonparabolicity,” *Physical Review B*, vol. 40, no. 8, pp. 5795–5798, 1989.
- [129] Z. Schlesinger, S. J. Allen, J. C. M. Hwang, and P. M. Platzman, “Cyclotron resonance in two dimensions,” *Physical Review B*, vol. 30, no. 1, pp. 435–437, 1984.
- [130] C. Kallin and B. I. Halperin, “Many-body effects on the cyclotron resonance in a two-dimensional electron gas,” *Physical Review B*, vol. 31, no. 6, pp. 3635–3647, 1985.
- [131] E. A. Henriksen, S. Syed, Y. J. Wang, H. L. Stormer, L. N. Pfeiffer, and K. W. West, “Disorder-mediated splitting of the cyclotron resonance in two-dimensional electron systems,” *Physical Review B*, vol. 73, p. 241309(R), 2006.
- [132] I. V. Kukushkin, J. H. Smet, K. Von Klitzing, and W. Wegscheider, “Cyclotron resonance of composite fermions,” *Nature*, vol. 415, pp. 409–412, 2002.
- [133] E. Batke, D. Heitmann, J. P. Kotthaus, and K. Ploog, “Nonlocality in the two-dimensional plasmon dispersion,” *Physical Review Letters*, vol. 54, no. 21, pp. 2367–2370, 1985.
- [134] V. E. Kozlov, a. B. Van’kov, S. I. Gubarev, I. V. Kukushkin, J. Falson, D. Maryenko, Y. Kozuka, A. Tsukazaki, M. Kawasaki, and J. H. Smet, “Observation of plasma and magnetoplasma resonances of two-dimensional electrons in a single MgZnO/ZnO heterojunction,” *JETP Letters*, vol. 98, no. 4, pp. 223–226, 2013.
- [135] V. E. Kozlov, A. B. Van’Kov, S. I. Gubarev, I. V. Kukushkin, V. V. Solovyev, J. Falson, D. Maryenko, Y. Kozuka, A. Tsukazaki, M. Kawasaki, and J. H. Smet, “Microwave magnetoplasma resonances of two-dimensional electrons in MgZnO/ZnO heterojunctions,” *Physical Review B*, vol. 91, no. 8, p. 085304, 2015.

- [136] F. Neppl, J. P. Kotthaus, and J. F. Koch, “Mechanism of intersubband resonant photoresponse,” *Physical Review B*, vol. 19, no. 10, pp. 5240–5250, 1979.
- [137] W. Knap, S. Contreras, H. Alause, C. Skierbiszewski, J. Camassel, M. Dyakonov, J. L. Robert, J. Yang, Q. Chen, M. Asif Khan, M. L. Sadowski, S. Huant, F. H. Yang, M. Goiran, J. Leotin, and M. S. Shur, “Cyclotron resonance and quantum Hall effect studies of the two-dimensional electron gas confined at the GaN/AlGaN interface,” *Applied Physics Letters*, vol. 70, no. 16, pp. 2123–2125, 1997.
- [138] S. A. Mikhailov, “Microwave-induced magnetotransport phenomena in two-dimensional electron systems: Importance of electrodynamic effects,” *Physical Review B*, vol. 70, p. 165311, 2004.
- [139] T. Ando, A. B. Fowler, and F. Stern, “Electronic properties of two-dimensional systems,” *Reviews of Modern Physics*, vol. 54, no. 2, pp. 437–672, 1982.
- [140] A. A. Zabolotnykh, *PhD thesis*. PhD thesis, Kotelnikov Institute of Radio Engineering and Electronics of the RAS, 2018.
- [141] T. N. Theis, J. P. Kotthaus, and P. J. Stiles, “Two-dimensional magnetoplasmon in the silicon inversion layer,” *Solid State Communications*, vol. 24, pp. 273–277, 1977.
- [142] X. Fu, Q. A. Ebner, Q. Shi, M. A. Zudov, Q. Qian, J. D. Watson, and M. J. Manfra, “Microwave-induced resistance oscillations in a back-gated GaAs quantum well,” *Physical Review B*, vol. 95, p. 235415, 2017.
- [143] A. V. Shchepetilnikov, Y. A. Nefyodov, and I. V. Kukushkin, “Observation of Microwave-Induced Magnetoresistance Oscillations in a ZnO/Mg_xZn_{1-x}O Heterojunction,” *JETP Letters*, vol. 102, no. 12, pp. 811–814, 2015.
- [144] D. F. Kärcher, A. V. Shchepetilnikov, Y. A. Nefyodov, J. Falson, I. A. Dmitriev, Y. Kozuka, D. Maryenko, A. Tsukazaki, S. I. Dorozhkin, I. V. Kukushkin, M. Kawasaki, and J. H. Smet, “Observation of microwave induced resistance and photovoltage oscillations in MgZnO/ZnO heterostructures,” *Physical Review B*, vol. 93, p. 041410(R), 2016.
- [145] A. V. Shchepetilnikov, Y. A. Nefyodov, A. A. Dremin, and I. V. Kukushkin, “Renormalization of the effective electron mass governing the period of microwave-induced resistance oscillations in ZnO/MgZnO heterojunctions,” *JETP Letters*, vol. 107, no. 12, pp. 770–773, 2018.
- [146] S. A. Studenikin, M. Potemski, P. T. Coleridge, A. S. Sachrajda, and Z. R. Wasilewski, “Microwave radiation induced magneto-oscillations in the longitudinal and transverse resistance of a two-dimensional electron gas,” *Solid State Communications*, vol. 129, no. 5, pp. 341–345, 2004.
- [147] O. M. Fedorych, M. Potemski, S. A. Studenikin, J. A. Gupta, Z. R. Wasilewski, and I. A. Dmitriev, “Quantum oscillations in the microwave magnetoabsorption of a two-dimensional electron gas,” *Physical Review B*, vol. 81, p. 201302(R), 2010.

- [148] M. L. Savchenko, A. Shuvaev, I. A. Dmitriev, A. A. Bykov, A. K. Bakarov, Z. D. Kvon, and A. Pimenov, “High harmonics of the cyclotron resonance in microwave transmission of a high-mobility two-dimensional electron system,” *Physical Review Research*, vol. 3, p. L012013, 2021.
- [149] Q. Li, J. Zhang, J. Chong, and X. Hou, “Electron mobility in ZnMgO/ZnO heterostructures in the Bloch-Grüneisen regime,” *Applied Physics Express*, vol. 6, p. 121102, 2013.
- [150] J. Falson, Y. Kozuka, J. H. Smet, T. Arima, A. Tsukazaki, and M. Kawasaki, “Electron scattering times in ZnO based polar heterostructures,” *Applied Physics Letters*, vol. 107, p. 082102, 2015.
- [151] Q. Shi, M. A. Zudov, J. Falson, Y. Kozuka, A. Tsukazaki, M. Kawasaki, K. Von Klitzing, and J. Smet, “Hall field-induced resistance oscillations in MgZnO/ZnO heterostructures,” *Physical Review B*, vol. 95, p. 041411(R), 2017.
- [152] A. T. Hatke, M. Khodas, M. A. Zudov, L. N. Pfeiffer, and K. W. West, “Multiphoton microwave photoresistance in a high-mobility two-dimensional electron gas,” *Physical Review B*, vol. 84, p. 241302(R), 2011.
- [153] Q. Shi, M. A. Zudov, I. A. Dmitriev, K. W. Baldwin, L. N. Pfeiffer, and K. W. West, “Fine structure of high-power microwave-induced resistance oscillations,” *Physical Review B*, vol. 95, p. 041403(R), 2017.
- [154] P. Coleridge, M. Hayne, P. Zawadzki, and A. Sachrajda, “Effective masses in high-mobility 2D electron gas structures,” *Surface Science*, vol. 361-362, pp. 560–563, 1996.
- [155] N. D. Drummond and R. J. Needs, “Quantum Monte Carlo calculation of the energy band and quasiparticle effective mass of the two-dimensional Fermi fluid,” *Physical Review B*, vol. 80, p. 245104, 2009.
- [156] D. Stein, K. v. Klitzing, and G. Weimann, “Electron Spin Resonance on As GaAs/AlGaAs Heterostructures,” *Physical Review Letters*, vol. 51, no. 2, pp. 130–133, 1983.
- [157] N. Nestle, G. Denninger, M. Vidal, C. Weinzierl, K. Brunner, K. Eberl, and K. von Klitzing, “Electron spin resonance on a two-dimensional electron gas,” *Physical Review B*, vol. 56, no. 8, p. R4359, 1997.
- [158] W. Jantsch, Z. Wilamowski, N. Sandersfeld, and F. Schäffler, “ESR investigations of modulation-doped Si/SiGe quantum wells,” *Physica Status Solidi (B)*, vol. 210, pp. 643–648, 1998.
- [159] C. F. O. Graeff, M. S. Brandt, M. Stutzmann, M. Holzmann, G. Abstreiter, and F. Schä, “Electrically detected magnetic resonance of two-dimensional electron gases in Si/SiGe heterostructures,” *Physical Review B*, vol. 59, no. 20, p. 13242, 1999.

- [160] M. Schulte, J. G. Lok, G. Denninger, and W. Dietsche, “Electron spin resonance on a two-dimensional electron gas in a single AlAs quantum well,” *Physical Review Letters*, vol. 94, p. 137601, 2005.
- [161] A. V. Shchepetilnikov, Y. A. Nefyodov, I. V. Kukushkin, L. Tiemann, C. Reichl, W. Dietsche, and W. Wegscheider, “Electron g-factor anisotropy in an AlAs quantum well probed by ESR,” *Physical Review B*, vol. 92, p. 161301(R), 2015.
- [162] T. J. Lyon, J. Sichau, A. Dorn, A. Centeno, A. Pesquera, A. Zurutuza, and R. H. Blick, “Probing Electron Spin Resonance in Monolayer Graphene,” *Physical Review Letters*, vol. 119, p. 066802, 2017.
- [163] A. V. Shchepetilnikov, D. D. Frolov, V. V. Solovyev, Y. A. Nefyodov, A. Großer, T. Mikolajick, S. Schmult, and I. V. Kukushkin, “Electron spin resonance in a 2D system at a GaN/AlGaN heterojunction,” *Applied Physics Letters*, vol. 113, p. 052102, 2018.
- [164] M. Dobers, K. v. Klitzing, J. Schneider, G. Weimann, and K. Ploog, “Electrical Detection of Nuclear Magnetic Resonance in GaAs/Al_xGa_{1-x}As Heterostructures,” *Physical Review Letters*, vol. 61, no. 14, pp. 1650–1653, 1988.
- [165] I. T. Vink, K. C. Nowack, F. H. L. Koppens, J. Danon, Y. V. Nazarov, and L. M. K. Vandersypen, “Locking electron spins into magnetic resonance by electron–nuclear feedback,” *Nature Physics*, vol. 5, pp. 764–768, 2009.
- [166] A. V. Shchepetilnikov, A. R. Khisameeva, Y. A. Nefyodov, and I. V. Kukushkin, “Anomalous spin resonance around even fillings in the quantum Hall regime,” *Physical Review B*, vol. 104, p. 075437, 2021.
- [167] C. Kallin and B. I. Halperin, “Excitations from a filled Landau level in the two-dimensional electron gas,” *Physical Review B*, vol. 30, no. 10, pp. 5655–5668, 1984.
- [168] I. V. Kukushkin, J. H. Smet, D. S. Lyne Aabergel, V. I. Fal’ko, W. Wegscheider, and K. Von Klitzing, “Detection of the electron spin resonance of two-dimensional electrons at large wave vectors,” *Physical Review Letters*, vol. 96, p. 126807, 2006.
- [169] J. F. Janak, “g-factor of the two-dimensional interacting electron gas,” *Physical Review*, vol. 178, no. 3, pp. 1416–1418, 1969.
- [170] J. Matsunami, M. Ooya, and T. Okamoto, “Electrically detected electron spin resonance in a high-mobility silicon quantum well,” *Physical Review Letters*, vol. 97, p. 066602, 2006.
- [171] Z. Wilamowski, W. Jantsch, H. Malissa, and U. Rössler, “Evidence and evaluation of the Bychkov-Rashba effect in SiGe/Si/SiGe quantum wells,” *Physical Review B*, vol. 66, p. 195315, 2002.

- [172] W. J. Wallace and R. H. Silsbee, “Microstrip resonators for electron-spin resonance,” *Review of Scientific Instruments*, vol. 62, pp. 1754–1766, 1991.
- [173] T. A. Wassner, B. Laumer, M. Althammer, S. T. B. Goennenwein, M. Stutzmann, M. Eickhoff, and M. S. Brandt, “Electron spin resonance of $\text{Zn}_{1-x}\text{Mg}_x\text{O}$ thin films grown by plasma-assisted molecular beam epitaxy,” *Applied Physics Letters*, vol. 97, p. 92102, 2010.
- [174] J. Matsunami and T. Okamoto, *Electron Spin Resonance and Related Phenomena in Low-Dimensional Structures*. Berlin: Springer, 1st ed., 2009.
- [175] X. Linpeng, M. L. Viitaniemi, A. Vishnuradhan, Y. Kozuka, C. Johnson, M. Kawasaki, and K. M. C. Fu, “Coherence Properties of Shallow Donor Qubits in ZnO,” *Physical Review Applied*, vol. 10, p. 064061, 2018.
- [176] D. Tabrea, *Transport Phenomena in Gated MgZnO/ZnO Heterostructures*. Msc thesis, Max Planck Institute for Solid State Research, 2017.
- [177] J. Falson and J. H. Smet, “Correlated phases in ZnO-based heterostructures,” in *Fractional Quantum Hall Effects* (B. Halperin and J. K. Jain, eds.), ch. 6, pp. 273–316, World Scientific, 2020.
- [178] A. V. Shchepetilnikov, Y. A. Nefyodov, I. V. Kukushkin, J. Falson, Y. Kozuka, D. Maryenko, A. Tsukazaki, M. Kawasaki, and J. H. Smet, “Interaction mediated electron spin resonance near even filling factors in a $\text{Mg}_x\text{Zn}_{1-x}\text{O}/\text{ZnO}$ heterostructure,” *Unpublished*.
- [179] S. Dickmann and I. V. Kukushkin, “Zero-momentum cyclotron spin-flip mode in a spin-unpolarized quantum Hall system,” *Physical Review B*, vol. 71, p. 241310(R), 2005.
- [180] J. P. Joshi and S. V. Bhat, “On the analysis of broad dysonian electron paramagnetic resonance spectra,” *Journal of Magnetic Resonance*, vol. 168, no. 2, pp. 284–287, 2004.
- [181] E. Abrahams, P. W. Anderson, D. C. Licciardello, and T. V. Ramakrishnan, “Scaling theory of localization: Absence of quantum diffusion in two dimensions,” *Physical Review Letters*, vol. 42, no. 10, pp. 673–676, 1979.
- [182] B. L. Altshuler, A. G. Aronov, and P. A. Lee, “Interaction effects in disordered fermi systems in two dimensions,” *Physical Review Letters*, vol. 44, no. 19, pp. 1288–1291, 1980.
- [183] M. Y. Simmons, A. R. Hamilton, M. Pepper, E. H. Linfield, P. D. Rose, D. A. Ritchie, A. K. Savchenko, and T. G. Griffiths, “Metal-insulator transition at $B = 0$ in a dilute two dimensional GaAs-AlGaAs hole gas,” *Physical Review Letters*, vol. 80, no. 6, pp. 1292–1295, 1998.
- [184] T. N. Zavaritskaya and E. I. Zavaritskaya, “Metal-insulator transition in inversion channels of silicon MOS structures,” 1987.

- [185] V. Dobrosavljevic, E. Abrahams, E. Miranda, and S. Chakravarty, “Scaling theory of two-dimensional metal-insulator transitions,” *Physical Review Letters*, vol. 79, no. 3, pp. 455–458, 1997.
- [186] Y. Hanein, U. Meirav, D. Shahar, C. C. Li, D. C. Tsui, and H. Shtrikman, “The metalliclike conductivity of a two-dimensional hole system,” *Physical Review Letters*, vol. 80, no. 6, pp. 1288–1291, 1998.
- [187] S. Papadakis and M. Shayegan, “Apparent metallic behavior at of a two-dimensional electron system in AlAs,” *Physical Review B*, vol. 57, no. 24, p. R15068, 1998.
- [188] P. T. Coleridge, R. L. Williams, Y. Feng, and P. Zawadzki, “Metal-insulator transition at $B = 0$ in p-type SiGe,” *Phys. Rev. B*, vol. 56, no. 20, p. R12 764, 1997.
- [189] T. Okamoto, M. Ooya, K. Hosoya, and S. Kawaji, “Spin polarization and metallic behavior in a silicon two-dimensional electron system,” *Physical Review B*, vol. 69, no. 4, p. 041202, 2004.
- [190] A. M. Finkel’stein, “Influence of Coulomb interaction on the properties of disordered metals,” *Zh. Eksp. Teor. Fiz.*, vol. 84, pp. 168–189, 1983.
- [191] B. I. Shklovskii and A. I. Efros, *Electronic Properties of Semiconductors*. New York: Springer-Verlag, 1986.
- [192] S. Dlimi, L. Limouny, J. Hemine, A. Echhelh, and A. El Kaaouachi, “Efros–Shklovskii hopping in the electronic transport in 2D p-GaAs,” *Lithuanian Journal of Physics*, vol. 60, no. 3, pp. 167–171, 2020.
- [193] T. B. Bateman, “Elastic moduli of single-crystal zinc oxide,” *Journal of Applied Physics*, vol. 33, pp. 3309–3312, 1962.
- [194] S. D. Sarma and E. H. Hwang, “Charged impurity-scattering-limited low-temperature resistivity of low-density silicon inversion layers,” *Physical Review Letters*, vol. 83, no. 1, pp. 164–167, 1999.
- [195] A. G. Zabrodskii and K. N. Zinov’eva, “Low-temperature conductivity and metal-insulator transition in compensate n-Ge,” *Zh. Eksp. Teor. Fiz.*, vol. 86, pp. 727–742, 1984.
- [196] N. F. Mott, “Conduction in glasses containing transition metal ions,” *Journal of Non-Crystalline Solids*, vol. 1, no. 1, pp. 1–17, 1968.
- [197] A. L. Efros and B. I. Shklovskii, “Coulomb gap and low temperature conductivity of disordered systems,” *Journal of Physics C: Solid State Physics*, vol. 8, p. L49, 1975.
- [198] J. J. Kim and H. J. Lee, “Observation of a nonmagnetic hard gap in amorphous In/InO_x films in the hopping regime,” *Physical Review Letters*, vol. 70, no. 18, pp. 2798–2801, 1993.

- [199] W. Mason, S. V. Kravchenko, and J. E. Furneaux, “Experimental evidence of the Coulomb gap in a high-mobility 2D electron system in silicon,” *Surface Science*, vol. 361-362, pp. 953–956, 1996.
- [200] J. Huang, L. N. Pfeiffer, and K. W. West, “Nonactivated transport of ultradilute two-dimensional hole systems in GaAs field-effect transistors: Interaction versus disorder,” *Physical Review B*, vol. 85, p. 041304(R), 2012.
- [201] S. Das Sarma, M. P. Lilly, E. H. Hwang, L. N. Pfeiffer, K. W. West, and J. L. Reno, “Two-dimensional metal-insulator transition as a percolation transition in a high-mobility electron system,” *Physical Review Letters*, vol. 94, p. 136401, 2005.
- [202] A. A. Shashkin, V. T. Dolgoplov, and G. V. Kravchenko, “Insulating phases in a two-dimensional electron system of high-mobility Si MOSFET’s,” *Phys. Rev. B*, vol. 49, no. 20, p. 14486, 1994.
- [203] M. Caravaca, A. M. Somoza, and M. Ortuno, “Nonlinear conductivity of two-dimensional Coulomb glasses,” *Physical Review B*, vol. 82, p. 134204, 2010.
- [204] S. V. Kravchenko, D. Simonian, and M. P. Sarachik, “Electric field scaling at a $B = 0$ metal-insulator transition in two dimensions,” *Physical Review Letters*, vol. 77, no. 24, pp. 4938–4941, 1996.
- [205] Y. C. Lee, C. S. Chu, and E. Castaño, “Effects of finite electric field and inelastic scattering on Anderson localization in two dimensions,” *Physical Review B*, vol. 27, no. 10, pp. 6136–6142, 1983.
- [206] M. E. Gershenson, Y. B. Khavin, D. Reuter, P. Schafmeister, and A. D. Wieck, “Hot-electron effects in two-dimensional hopping with a large localization length,” *Physical Review Letters*, vol. 85, no. 8, pp. 1718–1721, 2000.
- [207] J. Zhang, W. Cui, M. Juda, D. McCammon, R. Kelley, S. Moseley, C. Stahle, and A. Szymkowiak, “Non-Ohmic effects in hopping conduction in doped silicon and germanium between 0.05 and 1 K,” *Physical Review B*, vol. 57, no. 8, pp. 4472–4481, 1998.
- [208] R. Leturcq, D. L’Hôte, R. Tourbot, V. Senz, U. Gennser, T. Ihn, K. Ensslin, G. Dehlinger, and D. Grützmacher, “Hot-hole effects in a dilute two-dimensional gas in SiGe,” *Europhysics Letters*, vol. 61, no. 4, pp. 499–505, 2003.
- [209] P. D. Ye, L. W. Engel, D. C. Tsui, R. M. Lewis, L. N. Pfeiffer, and K. West, “Correlation lengths of the wigner-crystal order in a two-dimensional electron system at high magnetic fields,” *Physical Review Letters*, vol. 89, no. 17, p. 176802, 2002.
- [210] H. Fukuyama and P. A. Lee, “Dynamics of the charge-density wave. I. Impurity pinning in a single chain,” *Physical Review B*, vol. 17, no. 2, pp. 535–541, 1978.

- [211] I. Meinel, D. Grundler, S. Bargstädt-Franke, C. Heyn, D. Heitmann, and B. David, “High-sensitive superconducting magnetometry on a two-dimensional electron gas up to 10 Tesla,” *Applied Physics Letters*, vol. 70, pp. 3305–3307, 1997.
- [212] J. P. Eisenstein, H. L. Stormer, V. Narayanamurti, A. Y. Cho, A. C. Gosard, and C. W. Tu, “Density of States and de Haasvan Alphen Effect in Two-Dimensional Electron Systems,” *Physical Review Letters*, vol. 55, no. 8, pp. 875–878, 1985.
- [213] M. Brasse, S. M. Sauther, J. Falson, Y. Kozuka, A. Tsukazaki, C. Heyn, M. A. Wilde, M. Kawasaki, and D. Grundler, “Enhanced quantum oscillatory magnetization and nonequilibrium currents in an interacting two-dimensional electron system in MgZnO/ZnO with repulsive scatterers,” *Physical Review B*, vol. 89, p. 075307, 2014.
- [214] A. A. Shashkin, S. Anissimova, M. R. Sakr, S. V. Kravchenko, V. T. Dolgoplov, and T. M. Klapwijk, “Pauli Spin Susceptibility of a Strongly Correlated Two-Dimensional Electron Liquid,” *Physical Review Letters*, vol. 96, p. 0364031, jan 2006.
- [215] S. A. Vitkalov, M. P. Sarachik, and T. M. Klapwijk, “Spin polarization of two-dimensional electrons determined from Shubnikov–de Haas oscillations as a function of angle,” *Physical Review B*, vol. 64, p. 073101, 2001.
- [216] I. F. Herbut, “The effect of parallel magnetic field on the Boltzmann conductivity and the Hall coefficient of a disordered two-dimensional Fermi liquid,” *Physical Review B*, vol. 63, p. 113102, 2001.
- [217] A. A. Shashkin, S. V. Kravchenko, V. T. Dolgoplov, and T. M. Klapwijk, “Indication of the Ferromagnetic Instability in a Dilute Two-Dimensional Electron System,” *Physical Review Letters*, vol. 87, no. 8, p. 86801, 2001.
- [218] H. Noh, P. Lilly, C. Tsui, A. Simmons, H. Hwang, S. Das Sarma, N. Pfeiffer, and W. West, “Interaction corrections to two-dimensional hole transport in the large- r_s limit,” *Physical Review B*, vol. 68, p. 165308, 2003.
- [219] G. Zala, B. N. Narozhny, and I. L. Aleiner, “Interaction corrections at intermediate temperatures: Longitudinal conductivity and kinetic equation,” *Physical Review B*, vol. 64, p. 214204, 2001.
- [220] D. Simonian, S. V. Kravchenko, M. P. Sarachik, and V. M. Pudalov, “Magnetic field suppression of the conducting phase in two dimensions,” *Physical Review Letters*, vol. 79, no. 12, pp. 2304–2307, 1997.
- [221] K. Vakili, Y. P. Shkolnikov, E. Tutuc, E. P. De Poortere, and M. Shayegan, “Spin susceptibility of two-dimensional electrons in narrow AlAs quantum wells,” *Physical Review Letters*, vol. 92, no. 22, p. 226401, 2004.

- [222] V. M. Pudalov, A. Y. Kuntsevich, M. E. Gershenson, I. S. Burmistrov, and M. Reznikov, “Probing spin susceptibility of a correlated two-dimensional electron system by transport and magnetization measurements,” *Physical Review B*, vol. 98, p. 155109, 2018.
- [223] S. Li, Q. Zhang, P. Ghaemi, and M. P. Sarachik, “Evidence for mixed phases and percolation at the metal-insulator transition in two dimensions,” *Physical Review B*, vol. 99, p. 155302, 2019.
- [224] A. Bera and D. Basak, “Manifestation of spin-spin interaction ZnMg nanorods by electron paramagnetic resonance studies,” *Applied Physics Letters*, vol. 99, p. 194101, 2011.
- [225] Y. Kozuka, S. Teraoka, J. Falson, A. Oiwa, A. Tsukazaki, S. Tarucha, and M. Kawasaki, “Rashba spin-orbit interaction in a MgZnO/ZnO two-dimensional electron gas studied by electrically detected electron spin resonance,” *Physical Review B*, vol. 87, no. 20, p. 205411, 2013.
- [226] D. Tabrea, I. Dmitriev, S. Dorozhkin, B. Gorshunov, A. Boris, Y. Kozuka, A. Tsukazaki, M. Kawasaki, K. Von Klitzing, and J. Falson, “Microwave response of interacting oxide two-dimensional electron systems,” *Physical Review B*, vol. 102, p. 115432, 2020.
- [227] T. Gokmen, M. Padmanabhan, K. Vakili, E. Tutuc, and M. Shayegan, “Effective mass suppression upon complete spin-polarization in an isotropic two-dimensional electron system,” *Physical Review B*, vol. 79, p. 195311, 2009.
- [228] A. J. Daneshvar, C. J. Ford, M. Y. Simmons, A. V. Khaetskii, A. R. Hamilton, M. Pepper, and D. A. Ritchie, “Magnetization instability in a two-dimensional system,” *Physical Review Letters*, vol. 79, no. 22, pp. 4449–4452, 1997.